Structural, Optical And Photo-Electrochemical Properties Of H:TiO_2 Nanoparticle, TiO_2-MoS_2 Nanocomposite And TiO_2-$BiVO_4$ Core-Shell Nanoparticle Structures

Thesis

Structural, optical and photo-electrochemical properties of H:TiO_2 nanoparticle, TiO_2-MoS_2 nanocomposite and TiO_2-$BiVO_4$ core-shell nanoparticle structures

PhD thesis submitted

By

Manan Mehta

To

The Open University
Milton Keynes, U.K.

Under the supervision of

Prof. Satheesh Krishnamurty, Prof. Tony Nixon,
Prof.Suddhasatwa Basu and Dr. Aadesh Pratap Singh.

ACKNOWLEDGEMENTS

I sincerely thank my supervisors for their advice, support and mentorship during my PhD. I sincerely thank Prof. Satheesh Krishnamurthy to carry out PhD at The Open University, Milton Keynes and giving me chance to work in his reseach group. I really enjoyed the scientific, academic, and friendly environment in his research group. His encouragement and personal care and advice were very important for me. I would also like to thank Prof. Suddhasatwa Basu for his advice and suggestions which helped me to complete the thesis work on time. I thank Prof. *Tony Nixon for his encouragement and valuable advice.* I also thank Dr. Aadesh Pratap Singh for helping me in planning the research plan and experiments and teaching me important experimental skills.

I would also like to thank all the members of the Research Group at The Open University and Fuel Cell group at IIT Delhi for day to day support and their friendly behaviour. I would like to especially mention Dr. Rishabh Sharma, Dr. Sandeep Dhaka, Mr. Mujeeb Ahmed, Mr. Ravi Tejaswi Bajpai and Ms. Nisha for their help and support, both in and outside the laboratory.

I would like to sincerely thank my parents, sister Shivani, wife Diksha and my grandmother for their unconditional love and support throughout this endeavour.

--- Manan Mehta

CONTENTS

List of Figures

List of Tables

Abstract

Photo-electrochemical decomposition of water into oxygen and hydrogen for fuel applications is one of the most important research areas because of the vital need to meet the ever-increasing global energy demands by sustainable and clean methods. For photoelectrochemical water splitting, semiconductor should possess properties of efficient absorption of photons, suitable energy band alignment, stability in the electrolyte and efficient carrier transport. In this work, surface treatment, core-shell nanoparticle synthesis and formation of 1D-2D nanocomposites have been used as the methodologies to achieve the above-mentioned material requirements using low cost methods. The central objective of the present study is to achieve improved visible light absorption and enhanced carrier separation in TiO_2 nanoparticles, which have a major drawback of very poor visible light absorption despite having good stability in the electrolyte and a favorable energy band alignment.

A detailed literature review has been done to have a comprehensive view of the background of the work done by other researchers to achieve similar objectives. Based on the experiments carried out in this thesis, hydrogen treatment of TiO_2 nanoparticle in mild hydrogen conditions have been observed to enhance photo-electrochemical performance which is related to the observed incease in optical absorption in the visible light and improved surface catalytic properties. The role of Ti^{3+} defects for creating the energy states suitable of photon absorption and electronic transport has been established using experimental investigations and DFT based simulations. This is very important, as the nature of defects in terms of its energy position and localized/non-localized energy state is expected to influence the electronic properties of the resulting material. In another study, MoS_2 2D nanoflakes have been used to form 2D nanocomposites with TiO_2 particles. On addition of MoS_2 nanoflakes with lower energy gap to TiO_2

nanoparticles, 1D-2D nanocomposite samples show increased optical absorption in the visible part of the spectrum along with large area interface between the two components. The present study has resulted in understanding the effect of varying MoS_2 concentration and about 7.5 % of MoS_2 has been found to be an optimal concentration for increasing visible light abosorption without screening the surface catalytic properties of TiO_2. This is an important result of the present study. $BiVO_4$-TiO_2 core shell nanoparticles have also been used for studying photo-electrochemical properties and the increased photo-electrochemical performance has been understood by comparing the structural, optical, photocatalytic properties of core-shell nanoparticles with $BiVO_4$ and TiO_2 nanoparticles. Changes in the anodic PEC response of pristine TiO_2 nanoparticle to cathodic response observed in $BiVO_4$-TiO_2 nanoparticles is an interesting result. This has been explained on the basis of possible changes in semiconductor properties due to small thickness of the shell layer or due to its proximity with the electrolyte. Finally, summary of important results of the present thesis and scope for future research work in this area have been presented.

Chapter 1

Introduction

1.1 World Energy Needs

Per capita energy consumption of a country is a measure of not only its economic but also its social development[1]. At present, fossil fuels supply major part of world's total world energy consumption. However, due to rapid rise in energy consumption in last few decades especially of fossil fuels, fossil fuel reserves are facing a rapid depletion[2]. With the current rate of increase in energy consumption, the world energy demand will increase to 70 % higher than its present value in the year 2030 compared to its value in the beginning of year 2000[3]. Large-scale utilization of fossil fuels has resulted in environmental pollution and large concentrations of released harmful wastes due to combustion of fossil fuels which have already reached a serious dimension. The growing demand for energy, combined with the need to preserve and sustain clean environment, has created an urgent need for environment-friendly and sustainable energy technologies. Renewable energy technologies including photovoltaic, solar-thermal, wind energy, biomass-derived liquid fuels and biomass-fired electricity are potential alternatives which comprise about 14 % of the total world energy consumption[2]**.**

Solar energy utilization for terrestrial applications is one of the priority topics of the recent research [4, 5]**.** Solar energy is unique as it is inexhaustible, non-polluting and is probably the most uniformly distributed energy source worldwide. However, for an optimum utilization of non-conventional energy sources, particularly an intermittent source like solar energy, an intermediate energy storage system is also needed, which can link the primary source of energy with the end consumers. Many synthetic fuels, which can be produced with the help of nonconventional energy resources like solar

energy viz., hydrogen, methane, methanol, ethanol and ammonia, meet the criteria of abundance, storability, transportability and environment compatibility. However, hydrogen meets these requirements to the maximum extent. Table 1.1 presents some important characteristics of hydrogen which suggest its suitability as future energy carrier [6].

The search for efficient methods to renewably produce hydrogen has been a long-term research goal of many scientists around the world. Hydrogen is generally produced by steam reforming of non-renewable natural gas. Another common way of its production is via electrolysis of water, which requires high energy demand. To meet tomorrow's demand of cheap, environment friendly and renewable hydrogen, new and efficient ways of its synthesis need focus and are the need of the hour [7]. A process that is very promising, is extracting hydrogen by direct splitting of water using solar energy. A suitable material is required, which can absorb visible and ultraviolet part (i.e. the major part of solar energy) of solar radiant energy and can transfer this energy to water molecules for splitting. Utilizing this concept, various methodologies of photo-biological, photochemical, photovoltaic-electrolysis, photo-electrolysis have been proposed and a wide-ranging research effort is underway to optimize conditions for hydrogen production [8].

Table 1.1: Fuel Quality of Hydrogen

Properties	Parameters for Hydrogen*
1. Environmental damage due to burning of fuel	Combustion generates a harmless compound, H_2O, which is not a pollutant
2. Heat of combustion	34.18 kcal/g
3. Energy storage capacity	119 kJ/g
4.Usability with present time internal combustion engines	Can be used with minor alteration in engine
5. Transportability	Can be easily transported with/without conversion
6. Utility as fuel for aircrafts	Use for aircrafts is possible (AB-57 aircraft of US Air Force was test run on H_2 as early as in 1957).
7. Usability as domestic cooking fuel	Hydrogen can also be used as cooking gas
8. Safety aspects	Hydrogen has explosive limit of 4% in air, which is less than that of butane. Hence, its use as a fuel is also not safe.

*****Data taken from Ref. 6.

1.2 Photo-electrochemical Cell

Photo-electro-chemical (PEC) cells are devices that are used for the absorption of solar energy and its conversion to a usable form of chemical energy.

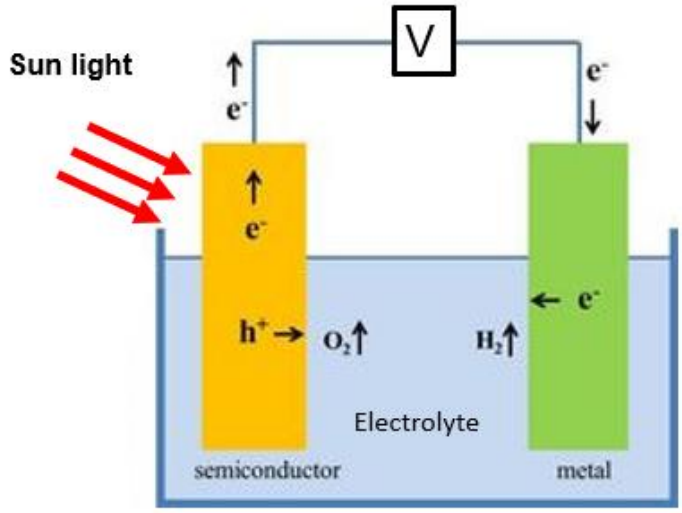

Figure 1.1: Schematic view of a typical photo-electro-chemical cell used for splitting of water to hydrogen and oxygen. (Adapted from Ref 9)

A photo-electro-chemical (PEC) cell consists of a semiconductor or metal electrodes cathode and anode in an electrolyte solution as illustrated in Fig. 1.1. Either of the two electrodes, or both can be photoactive. The electrodes, which is photoactive, are generally made up of some semiconductor, which absorbs radiations with photon energy ($h\upsilon$) greater than their band gap energy (E_g). Thus, the most important portion of a PEC cell is the semiconductor material and its junction between liquid electrolyte.

Fujishima and Honda were the first to use single crystal TiO_2 (as photo-anode) for PEC splitting of water[10]. Since then, there has been considerable progress, in this area. Gerischer[11] presented a thorough overview of this theory, Nozik provided an analytical account of the photo-electro-chemical devices[12], and Hellergave an excellent analysis of efficiencies of various photo-electro-chemical systems[13]. Further, Getoffand Pleskov gave a detailed analysis of PEC processes[14,15]. The most efficient photo-electro-chemical cells (efficiency ~13%) is observed in a p-type indium phosphide photocathode, onto which tiny islands of platinum have been deposited. Cells involving

n-CdS, n- TiO_2 and n-$SrTi_2O_2$ as photoanodes have achieved good efficiencies of ~10 % [16].

Upon irradiation of the photoactive electrodes with photons of energy larger than the band gap energy of semiconductor, electron-hole pairs are formed and the chemical equilibrium in the PEC cell is disturbed. This creates a photo-voltage that gives rise to photocurrent through an open circuit, in the direction of the electrode having lower chemical potential[17].The flow circuit of electrons is completed by electron transfer processes over the electrode-electrolyte interfaces. Depending upon the nature of chemical reactions that occur during irradiation, photocurrent can represent a portion of light energy that has been converted to either electrical or chemical energy. PEC cells have the advantage of combining the photovoltaic cell and electrolyzer into one system. Further, the advantage of PEC cells over photovoltaic cells is that, in PEC cells junction between two semiconductors is not required. The junction is formed spontaneously at the semiconductor-electrolyte interface. However, a potential disadvantage in a photo-electro-chemical cell is the close proximity of the semiconductor used with the liquid electrolyte, which can lead to photo-corrosion and thus, dissolution and degradation of the photoactive electrodes. Hence, its stability and long duration utility are important areas of concern[18].

1.3 Semiconductor Physics: Some Important Concepts for PEC conversion

1.3.1 Band Structure

In solid state materials, because of overlap of wave function of different levels on tight packing of atoms in a solid, overlap of energy levels of isolated atom get converted to energy bands with continuous value of allowed values of energy[19]**.** Valence band (E_V) is the highest occupied band and the immediate next band with higher energy, is called the conduction band (E_C). The difference between the highest energy in the filled

valence band and the lowest energy in the vacant conduction band is called the forbidden gap or band gap (E_g) as shown in Fig. 1.2. It represents a range of energies in which no allowed values of electron energy states exist.

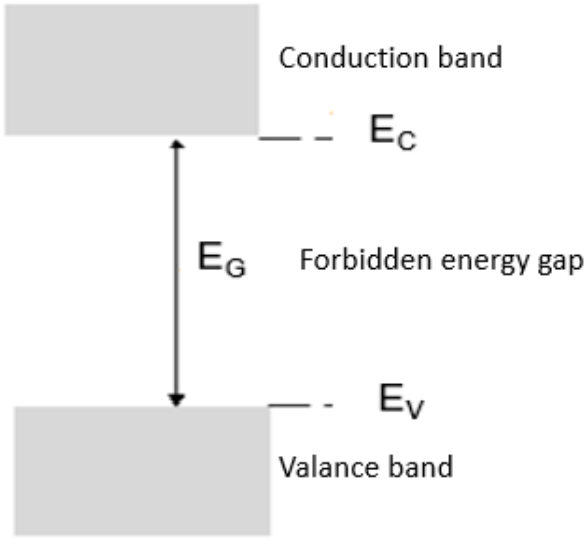

Figure 1.2: Schematic representation of band gap (EG) and band edges (EC and EV) of a semiconductor material (redrwan and adapted from Ref. 19).

In semiconductors and insulators, the highest filled energy level of valence band and the lowest vacant energy level of conduction band are called valence band edges (E_v) and conduction band edges (E_c), respectively (Fig. 1.3). Electrons in valence band cannot carry current. But, at temperatures above zero Kelvin, electrons can be excited by the thermal motion of the atoms, resulting in some electrons filling the orbitals in the conduction band. The electrons in the conduction band are mobile and can carry current. As a result of excitation of electrons, there will be a vacant position in the valence band (named as hole), which also contribute to the flow of current. As shown in Fig 1.3, the difference between an insulator and semiconductor gives the magnitude of the forbidden gap and the value of an energy gap changes the concentration of electrons and holes in the conduction and valence bands, respectively. Hence, the current flow in a semiconductor can be estimated to be the sum of the motion of

electrons in the conduction band and holes in the valence band. Electronic conductivity in the semiconductors requires electrons to be excited to the conduction band. This may be achieved thermally (by increase in temperature), or optically (by application of light)[19].

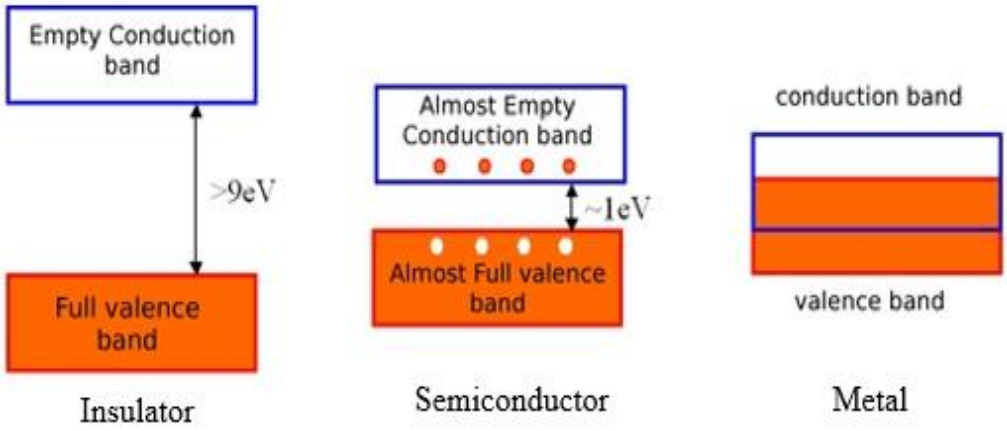

Figure 1.3: A schematic diagram showing the energy band diagram of large forbidden gap in a insulator, a smaller band gap in a semiconductor and overlapped energy bands in case of a metal (redrawn and adapted from Ref. 19).

An important concept to describe the semiconductors is that of the Fermi level, (E_F), which is defined as the energy level where the probability of existence of an electron is 0.5 (i.e., where the probably that the level is either occupied or vacant)**.** In a metal, the conduction band is energetically either adjacent or overlapping to the valence band, as shown in Fig. 1.3 above. Thus, electrons can be easily excited from the valence band into the conduction band by thermal energy and do not have to overcome any forbidden energy gap. Because of this minimal energy difference between the valence and conduction bands, conduction occurs easily in a metal. In case of semiconductor, in the ground state all of the electrons are in the valence band and there are no electrons in the conduction band, so the probability of finding an electron abruptly changes from 100% at the top of the valence band to 0% at the bottom of the conduction band. At higher

temperatures, some electrons gain energy in excess of the Fermi level and reach the conduction band. The probability of occupation of an allowed energy state corresponding to energy E, can be statistically calculated from the Fermi-Dirac distribution function f(E), described as equation (1.1)[20].

$$f(E) = [1 + e^{(E - E_F)/kT}] \quad \ldots\ldots\ldots\

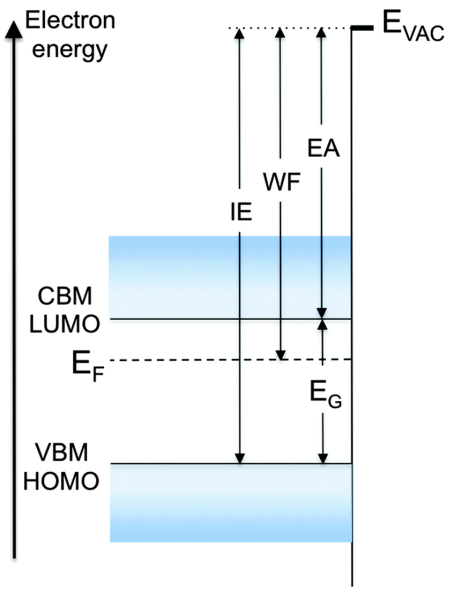

Figure 1.4: Energy diagram of a semiconductor showing CB minima (CBM or LUMO level) and VB maxima (VBM or HOMO level), vacuum level EVAC, work function WF, energy gap EG, ionization energy IE and electron affinity EA (adapted from Ref. 22).

Energy gap (E_G) is the energy difference between conduction band and valence band. In general, electrons are naturally bound to the solid. At the surface of the material, they are prevented to escape (to the vacuum) by an energy barrier that culminates at the vacuum level (E_{VAC}). The energy difference between E_{VAC} and top of the valance band is therefore, the minimum energy necessary to remove an electron from the system, and is known as the ionization energy (IE). Work function W_F is defined as the energy necessary to remove an electron originally at the Fermi level (E_F) deep inside the material and place it at rest at a point in free space just outside the surface, *i.e.* at E_{VAC}.

In a semiconductor, work function is very sensitive to the surface conditions as it is a difference in the position of the vacuum level (E_{vac}) and Fermi energy (E_F). Anything which affects Fermi energy can also affect the work function. It is well known that Fermi energy of a semiconductor depends upon the doping concentration and temperature. In a *n* type semiconductor, Fermi energy is close to the conduction band. In a *p* type semiconductor,

Fermi energy is close to the valence band. For an intrinsic semiconductor, Fermi energy is close to the middle of the forbidden gap. With an increase in the dopant concentration, Fermi energy shifts towards the conduction band (*n* type semiconductor) or towards the valence band (*p* type semiconductor). With increase in temperature, Fermi energy shifts towards the centre of the forbidden gap[19].

1.4 PEC Cell: Important Concepts

The key components of a PEC cell are, undoubtedly, the semiconductor electrode and the electrolyte. The semiconductor-electrolyte junction is the main functional unit. A clarity in the concepts of chemistry and physics of semiconductor in contact with the electrolyte solution is needed to understand the mechanism of the processes occurring in a photo-electro-chemical cell. In this section, an attempt has been made to present some of these aspects of a PEC cell.

1.4.1 Optimum value of band gap for light absorption

One of the most important consideration for choosing a semiconductor material for solar cell and photo-electro-chemical cell is its band gap. It is required to completely absorb the solar spectrum for converting it to electrical energy in a solar cell or chemical energy in case of PEC.

For a fixed value of band gap, the solar photons having energy higher than the band gap are absorbed and the one having energy smaller than the band gap are transmitted as shown in Fig. 1.5. This can be termed as the transmission loss. For the photons having energy higher than the band gap, the excess energy, which is the difference between photon energy and band gap of the semiconductor (photon energy – band gap) is lost as heat energy. As the photon is absorbed, the photoexcited electron is excited to an energy state as per the value of photon energy. The photoexcited electron quickly looses its energy by collision with the

lattice and occupies the conduction band minimum. Therefore, these photons having energy higher than the band gap are not absorbed efficiently[23].

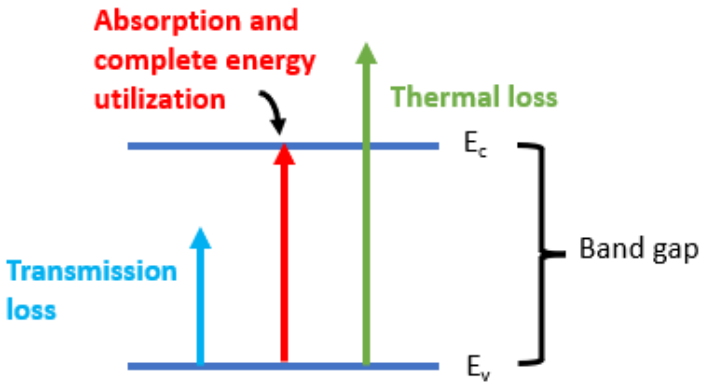

Figure 1.5: A schematic description of transmission and thermal loss during absorption of solar photons having energy lower (blue) and higher (green) than the band gap, respectively. As shown, photon having energy equal to the band gap (red arrow) is effeciently absorbed as its energy is completly converted to the energy of the electron-hole pair (Adapted from Ref. 23).

The maximum energy which can be efficiently absorbed can be described by the product of band gap energy and number of photons absorbed. Maximum photon energy absorbed is equal to $E_g.n_{ph.}$

The optimum value of band gap for one semiconductor to absorb solar light is 1.1 -1.2 eV. As a result, CdTe, Si and $CuIn_2Se_2$ are some of the semiconductors suitable for solar cell applications. For PEC cells, there are additional conditions to be discussed below[24].

1.4.2 Requirement of Eg for PEC

PEC cells can be constructed with p or n type semiconductors. When a PEC cell, with n-type semiconductor, is used for the purpose of direct water splitting, oxygen is formed at anode by hole induced oxidation of water and hydrogen is evolved at cathode by the complimentary reduction process. In a PEC cell, with p-type semiconductor, the flow

of charge carriers will be in a reverse direction and H_2 and O_2 would evolve at semiconductor photocathode and anode (i.e. counter electrode), respectively. The transfer of photoexcited electrons and holes as per equation 1.3 is shown in the Fig 1.6.

$$\text{Semiconductor (n type)} + h\upsilon \longrightarrow e^- + h \qquad \ldots\ldots\ldots\ldots\ldots\ldots\ldots\ldots 1.3$$

The two redox reactions that proceed at the cathode and anode with the participation of these electrons and holes are given below in equation 1.4.

At photoanode $\quad 2H_2O + 4h^+ \longrightarrow O_2 + 4H^+$

At cathode $\quad 4H^+ + 4e^- \longrightarrow 2H_2$

Overall reaction $\quad 2H_2O \longrightarrow 2H_2 + O_2 \qquad \ldots\ldots\ldots\ldots\ldots\ldots\ldots 1.4$

If there is no resistance in the circuit, the Fermi level of the counter electrode will be at the same level as that of the semiconductor. In order to split water with light irradiation, the flatband potential of the semiconductor has to be at a higher energy than the redox potentialfor hydrogen evolution, $U^0(H_2O \longrightarrow H_2)$. For this, the band gap of the semiconductor must be more than 1.23 eV, which is the position of U^0 $(H_2O \longrightarrow O_2)$ with reference to U^0 $(H_2O \longrightarrow H_2)$[25].

1.4.3 Alignment of the energy band diagram with redox potentials

There is a thermodynamic relationship between the band edges of a semiconductor photocatalyst and the redox potentials of species entering into redox reactions. Fig.1.6 shows the alignment between band edges of semiconductor and the electrochemical potentials of the two redox half reactions of water decomposition with respect to the vacuum level[26]. It is clear that for driving the oxygen evolution reaction, the photo-generated-hole energy must be lower than the electrochemical potential of the O_2/H_2O redox couple, and for driving the hydrogen evolution reaction, the photo-generated electron energy must be higher than the potential of the H^+/H_2 redox couple. The

thermodynamic rule states that higher the conduction band minimum energy and lower valence band maximum energy, the stronger tendency for reduction and oxidation reactions, respectively. The ideal energy difference between the valence and conduction band edges for photo electrolysis of water is between 1.6–2.4 eV, while taking the losses at the semiconductor/liquid interface due to the concentration and kinetic overpotential needed to drive reactions. The two band edges must straddle the electrochemical potentials of the O_2/H_2O and H^+/H_2 redox couples[27].

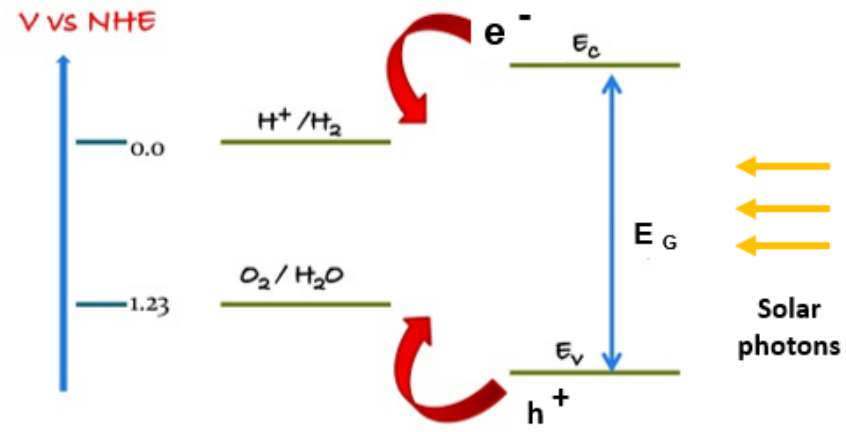

Figure 1.6: A schematic description of the requirement of straddling of water redox potential w.r.t conduction and valence band edges of the semiconductor (Redrawn and adapted from Ref. 28)

Metal oxide semiconductors that are stable and easy to synthesize. Tungsten oxide (WO_3), bismuth vanadium oxide ($BiVO_4$) and tin dioxide (SnO_2), are the potential candidates for visible light driven photocatalysts. The primary reason being the band gaps of WO_3 and $BiVO_4$ are 2.8 eV and 2.4 eV, respectively[29].However, they cannot be used for hydrogen production due to their deep conduction band (CB) levels at potentials more positive than 0 V vs NHE (pH = 0) as shown in the Fig.1.7.

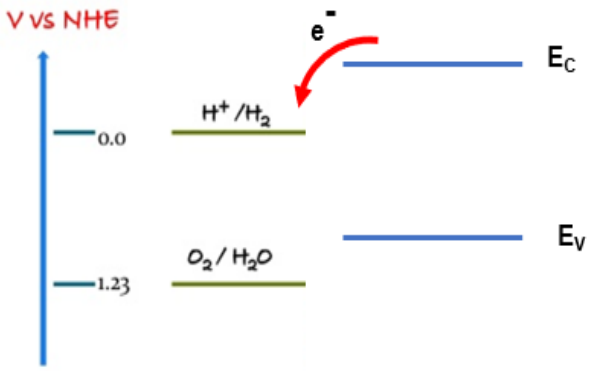

Figure 1.7: Partial straddling of water redox potential resulting in the limitation that only hydrogen formation can take place at the semiconductor surface (Redrawn and adapted from Ref. 28).

The alignment of the energy band w.r.t the water redox potentials is such that the conduction band edge is below the hydrogen redox potential. Such a semiconductor can only be used for oxygen evolution. In Fig 1.8 show a typical band gap alignment of these systems.

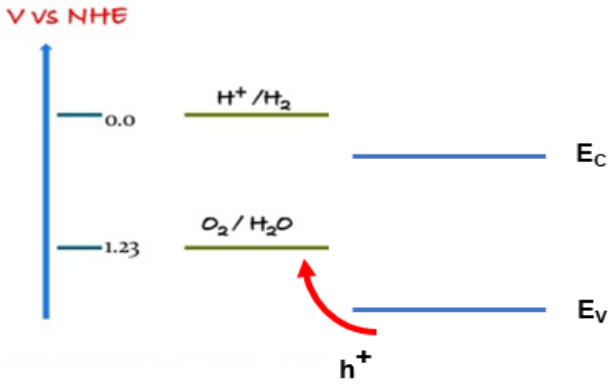

Figure 1.8: Partial straddling of water redox potential resulting in limitation that only oxygen formation can take place at the semiconductor surface (Redrawn and adapted from Ref. 28).

1.4.4 Semiconductor materials for water splitting applications

Fig. 1.9 shows a variety of semiconductor materials that can be used for photo-electro-chemical water splitting. As per the above discussion, band gap and straddling of the water redox potentials by conduction and valence bands are important requirements for

efficient absorption of sun light and separation of electron hole pairs at the semiconductor-electrolyte interface. Materials like WO_3 and Fe_2O_3 have band gap values very close to optimum values but their conduction band is below the hydrogen redox potential. Similarly, materials like Si have the valence band edge above the oxidation redox potential. Materials like TiO_2 are ideal in terms of straddling requirement but have very high band gap.

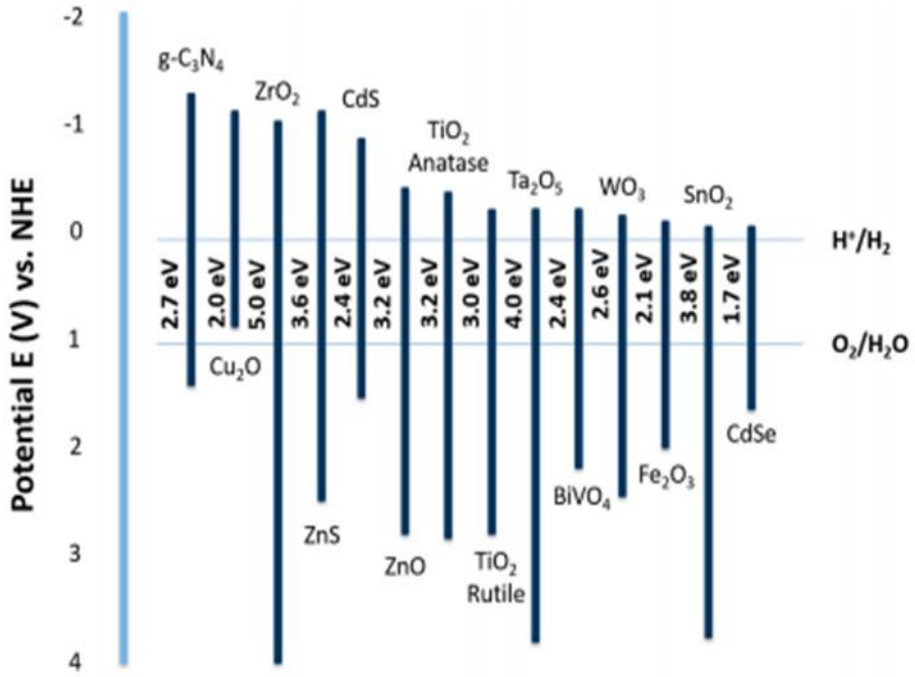

Figure 1.9: Conduction and valence band edge for a variety of semiconductor materials w.r.t water redox levels (Adapted from Ref. 30).

The stability of the electrode is also a deciding factor in addition to the band gap. GaAs and GaP are the semiconductors with low band gaps. However, they are not stable against photo-corrosion or electrochemical corrosion in aqueous medium. In contrast, oxides of transition metals, like TiO_2, ZnO, WO_3, PbO are stable in aqueous solution either as photoanode or as photocathode. But the importance of their stability in aqueous environment is nullified by their poor absorption in solar spectrum on account of their high band gap. Therefore, there is a large research scope for modifying the

optical, energy band diagram and stability properties for efficient photo-electro-chemical water splitting.

1.5 Modification of Material Properties

1.5.1 Surface engineering

Surface engineering involve modifying the properties of materials and nanoparticles by post deposition surface treatments. Surface treatments varies from sintering the nanoparticles in a reducing or oxidizing environment to bombardment by ions. Surface engineering is important for the present study as one can modify the optical properties by introducing defects in the forbidden gap of a material. Vacancies interstitials and dangling bonds at the surface result in the appearance of defect states in the forbidden gap. These defect states result in absorption at energy lower than the band gap, which can be useful in photoelectrical application. Defects can also act as sink or recombination centres for photogenerated carriers, which can deterioate the photocurrent and then harmful for PEC properties. The nature of defects and their position in the energy gap is thus, very important. Introduction of defects will also result in the modification in the surface catalytic properties.

1.5.2 Controlling properties by varying nanoparticle size

Controlling the properties of materials by varying the nanoparticle size is an important methodology of tailoring the material properties for specific application[31]. Decrease in nanoparticle size results in increase in the band gap of semiconductor materials due to quantum confinement effect.

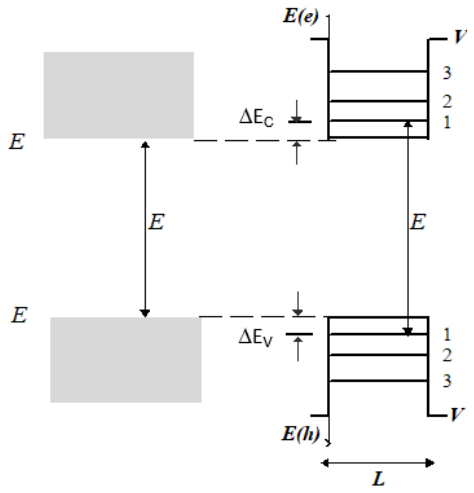

Figure 1.10: Energy band diagram of a bulk semiconductor and modification due to quantum confinement resulting in blue shift in forbidden gap (Redrawn and adapted from Ref. 32).

As shown in Fig 1.10, quantum confinement of an electron in a potential box of dimension L (size of the nanoparticle) results in continuous allowed values of energy in conduction and valence bands which are discrete and a finite value of energy (in comparison to zero value allowed in a case of bulk materials). This results in the shift in the bottom and top of conduction and valence band by values ΔE_C and ΔE_V, respectively. The band gap of the semiconductor nanoparticle thus, becomes a function of nanoparticle size being proportional to $1/L^2$.

The specific surface area of the nanoparticle (surface area per unit volume) is proportional to 1/L. With decrease in size of the nanoparticles, the specific surface area increases as the dimension of the nanoparticle becomes smaller. This results in the enhancement of the surface catalytic properties but also affect the stability of the nanoparticle due to increased surface areas resulting in increase in chemical instability.

1.5.3 Core-shell nanoparticle formation

Core-shell nanoparticle formation is a very useful methodology for controlling the optical and carrier transport properties[32]. By choosing a small band gap material, it is

possible to increase the optical absorption of the incident solar light. This is particularly useful for carrier transport as light absorption in the visible part of the solar spectrum can be increased resulting in enhanced PEC response[33]. Core- s hell material can be chosen so as to increase the stability of semiconductor core in the liquid electrolyte and also to enhance the surface catalytic properties. A correct alignment of the energy bands of core-shell semiconductors can result in the separation of photo-generated electrons and holes at the interface, as shown in Fig 1.11. Lower energy photons can be absorbed in the smaller energy band gap semiconductor. It is clear that an effecient hetero-interface requires a correct selection of the two semiconductor materials for a favourable energy level alignment.

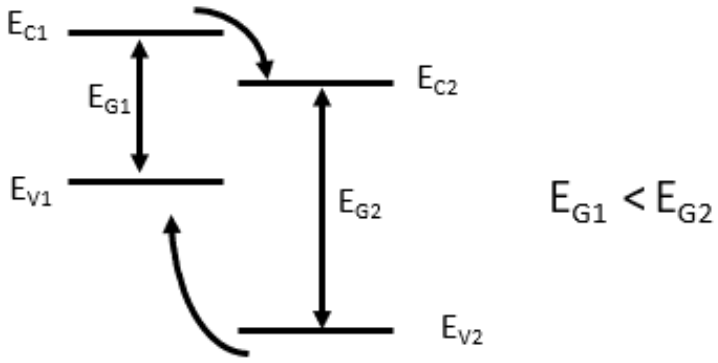

Figure 1.11: Alignment of energy levels of core and shell semiconductors at the nanoparticle heterointerface (Redrawn and adapted from Ref. 34).

1.6 Literature Review

As discussed above, it is very important for a semiconductor material to fulfill all the requirements for the photoelectrical electrode and the main challenge for high efficiency PEC water splitting is to search for appropriate semiconductor materials acting as highly active photo-electrodes or to modify properties of the semiconductor by different material modification methodologies.TiO_2 is one of the most widely used materials. Therefore, In this thesis a discussion with the properties of TiO_2 and how

these properties have been modified by using surface treatments are presented. As these have attracted greater attention since the realization of solar-driven water splitting by using TiO_2[10]. However, due to its wide band gap (≈3 eV), TiO_2 is effective only in the ultraviolet light range and thus, only a small portion (5%) of the solar energy is utilized[35].

1.6.1 Titanium dioxide (TiO_2) as a promising photoelectrode material

Titanium dioxide (TiO_2) possesses many desirable properties which include good chemical stability, non-toxicity, low cost, and most importantly, suitable band gap energy levels for the desired water splitting and CO_2 reduction reactions[36,37]. There are three polymorphs of TiO_2 which are found in nature: tetragonal rutile, tetragonal Anatase, and orthorhombic[38,39]**.** All TiO_2 polymorphs comprise of TiO_6 octahedra but differ in the distortions of the octahedron units and in the manner the edges and corners are shared, as shown in Fig 1.12. Anatase crystalline is a distorted octahedral coordination, in which every Titanium atom is surrounded by six oxygen atoms in an elongated octahedral geometry adopting axial symmetry. In rutile case, additional in-plane and out-of-plane bond length and bond angle distortions exist. In brookite, stronger distortions lead to a loss of local symmetry and formation of symmetric TiO_6 units[40,41]. Deviations in crystal structure lead to diverse electronic structure of these polymorphs thus, affecting their charge transfer ability and band energy levels. The Rutile and Anatase are the most widely studied phases for PEC applications[42]. Anatase to Rutile solid state phase transition is known to depend on nanoparticle size, dopants and structural defects[43,44]. Anatase phase is considered to be kinetically stable phase, whereas Rutile is a more stable phase from thermodynamic consideration[42]. Anatase to Rutile phase transformation usually take place between 600^0C to 700^0 C[45]. The growth temperature for Anatase phase is about 200 C and it transforms to Rutile phase at higher

temperature at about 600C[45,46]. Thus, 350^0C to 400^0 C seems to be the optimum temperature range for Anatase phase growth[42]. In bulk state, rutile is the most thermodynamically stable form while the Anatase is generally more active, due to the higher charge mobility and longer exciton diffusion length in the anatase TiO_2[46]. Both bulk Anatase and Rutile possess band gaps of energy 3.2 eV and 3.0 eV, respectively[47]. Therefore, only ultraviolet irradiation in solar spectrum can be absorbed by TiO_2. However, easily-modified electronic structure with higher charge carrier mobility and excellent surface chemical properties makes it a widely suitable material[48,49].

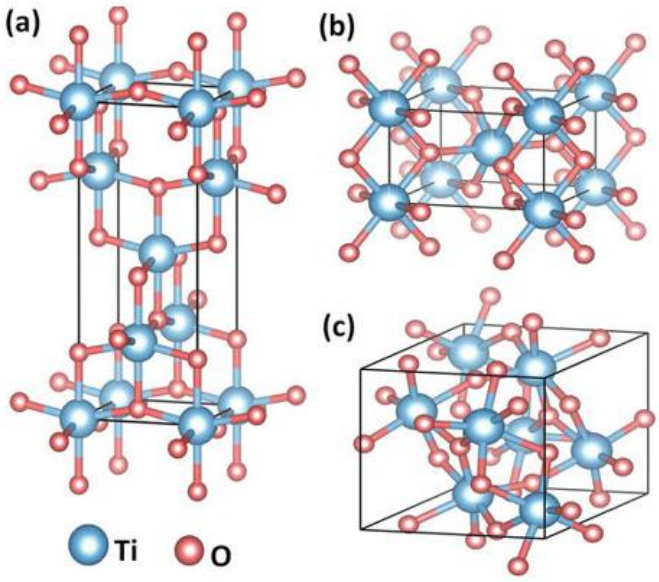

Figure 1.12: Crystal structure of TiO2: a) anatase (tetragonal), b) rutile (tetragonal)and c) brookite (orthorhombic) phases. (adapted from Ref. 50).

1.6.2 Modification of TiO_2 properties

As discussed earlier, nanoparticle methodology is a useful method of modifying the properties of semiconductor materials. At nanoparticle sizes, the surface area of the material is significantly enhanced due to nanoparticle effect. From this point of view,

synthesizing nanoparticle or sub micron sized TiO_2 nanoparticles is one of the most important methodology for improving the photo-electro-chemical properties.

Photo-electrodes which comprises of mixed TiO_2 nanoparticles possesses large specific surface area (hundreds of m^2/g) as well as excellent light scattering effect which lead to fast interfacial charge transfer, low series resistance, superior charge collection efficiency, and hence much higher power conversion efficiency[51-54]. However, the efficiency of the nanoparticulated TiO_2 film is usually low as compared to that of the TiO_2 film with well-designed morphologies, such as nanotubes, nanowires or hierarchical structures. This is mainly due to the large crystal size, grain boundaries between TiO_2 crystallites and less exposed active facets resulting in low effective surface area. TiO_2 nanoparticles films fabricated from thermally sintered nanoparticles can provide desirable high specific surface area useful for PEC applications. However, the electron diffusion coefficient of these nanoparticulate films is several orders of magnitude smaller than that of single-crystal TiO_2 due to large number of interparticle grain boundaries thus, limiting the PEC efficiency. This is due to the increased electron trapping at the grain boundaries of TiO_2 nanoparticles. Compared to sintered nanoparticle films, oriented 1-D TiO_2 nanostructures such as nanowires, nanorods and nonotubes arrays could offer direct electron transport pathway and higher electron mobility, leading to increased charge transport rate[55,56].

Aligned TiO_2 nanowire or nanorod films have been fabricated via several methods including template-directed growth, high temperature vapor phase deposition, and low temperature chemical synthesis (hydrothermal and solvothermal). In early works, template-directed growth was commonly used to synthesize oriented TiO_2 nanowires or nanorods. The most versatile hard template is an iodized alumina oxide. Based on such a template, aligned TiO_2 nanorod arrays on Indium tin oxide (as conductig

substrates) have been prepared using sol-gel and electrochemical deposition methods[56-60] and used them as photo-electrodes for PEC water splitting. The electrons exhibited a high collection rate at the back contact as observed from the IPCE of 79% at 350 nm. This was attributed to the fast vertical charge transport through the long axis of the nanorods, reduced surface defects and the restricted electron-hole recombination. Electrochemical anodization has also been utilized for growing nanostructures for PEC applications[61].

Similar to the properties of 1D TiO_2 nanostructures, 2D nanostructures also have direct electron path ways and favorable electrical and optical properties. There have been enormous efforts made to the synthesize nanobelt or nanoribbon shaped TiO_2 powders for photocatalytic applications, with encouraging results for PEC applications[62-66]. There also have been studies which have been conducted on the surface modification by incorporating Pd on hydrothermally prepared TiO_2 nanobelts for PEC application. Due to the large effective surface areas of TiO_2 nanobelts and Schottky barrier junctions between the noble metal (Ag or Pd) nanoparticles and TiO_2 nanobelts, decorated TiO_2 exhibited excellent PEC sensitivity and selectivity, moderate working temperature, short response/recovery time and good reproducibility. By controlling the treatment given to TiO_2 nanobelt substrate, TiO_2 nanobelt/ZnO nanorod photoelectrodes with flower-like nanostructures were fabricated.

1.6.3 Modification of the TiO2 propertiesby surface treatments

Doping, alloying, composite formation methods have been used to modify the properties of TiO_2 mainly from the point of enhancing the optical properties in the visible spectral range. Doping is used to narrow the band gap of TiO_2 for extended visible light absorption. However, doped TiO_2 nano-particles, showed limited solar water splitting due to dopant induced charge recombination centres. Chen et. al.[67]

proposed a novel concept of "surface disordering" for extended visible light absorption of TiO_2. With the sample color changed from white to black by post hydrogenation, the disorder-engineered nanophase "black TiO_2" consisted of a crystallized core and highly disordered surface layer shell was realised. A laboratory scale experiment carried out in a full-spectrum solar light exposure showed that the H_2 production rate was close to 10 mmol/h/g and it was two orders higher than normally observed response[68]. DFT calculations reveal surface disordering defects on the surface, because of mid-gap electronic states created in hydrogenated anatase TiO_2 nanocrystals. Changes in structural properties due to surface disordering on photocatalytic performance of TiO_2 has been reported in a number of studies[69-78]. It has also been shown that there is an efficient separation of electron–hole pairs which effectively contributes to the improved PEC performance of the surface disordered TiO_2[79]. Kang et al.[80] performed $NaBH_4$ treatment of TiO_2 nanotubes to introduce oxygen vacancies. An electrochemical reductive process was carried out by Xu et al.[81] to hydrogenate TiO_2 nanotube arrays. Similar to the $NaBH_4$ treated TiO_2 nanotube arrays, the electrochemically reduced TiO_2 nanotube arrays showed increased photo-activity. Wang et al.[82] synthesized hydrogenated TiO_2 nanowires by annealing it in hydrogen atmosphere at various temperatures. Higher density of oxygen vacancies and impurity levels were induced within the bandgap of TiO_2, resulting in increased donor density, extended optical absorption and improved photocurrent density. By anodization of titanium substrate and subsequent hydrogenation approach, Li et al.[83] synthesized hydrogenated TiO_2 nanotube photoelectrodes. It was shown that oxygen vacancies introduced into the TiO_2 nanocrystals as shallow donors significantly improve the electronic conductivity and optical absorption ability of the TiO_2 nanotube photoelectrodes. The surface disordering method was also applied to other semiconductor materials such as WO_3[84],

ZnO[85], $SrTiO_3$[86], VO_2[87] and $Li_4Ti_5O_{12}$[88] and the resulting structures been used in wide ranging applications.

In addition to increased absorption, defects states also enhances the carrier recombination process which is not desirable for optoelectronic applications such as PEC energy conversion. To reduce this effect, surface passivation treatments proved to be an effective way to reduce recombination of electron and hole pairs[89,90]. Hoang et al.[91] demonstrated that by coating a cobalt thin film on the surfaces of TiO_2 nanorods effectively improves the PEC performance for water splitting. It is assumed that the cobalt treatment saturates the dangling bonds on the TiO_2 surface. By tuning the ALD deposition time, the thickness of the rutile shell TiO_2 coating can be controlled and passivated TiO_2 nanowires achieved a higher photocurrent density[92].

Doping of impurity atoms has also been used for passivating surface states[93] Gd doping has been observed to enhance light absorption efficiency of TiO_2 and passivation of the surface reactive states resulting in enhanced charge separation efficiency[93]. It has been shown that doping of H and Li can passivate the defect states in TiO_2 nanotube arrays[94]. H and Li doped TiO_2 has been shown to increase the photocurrent as compared to the pristine TiO_2. A summary of different surface treatments used in the literature to modify the properties of TiO_2 for PEC applications has been shown in Table 1.2.

Table 1.2: Effect of surface treatment on the PEC properties of TiO_2 as reported in the literature.

Sample	Synthesis method	Surface treatment	Morphology	PEC properties	Reference
Hydrogen treated Rutile TiO_2 nanorod	Anodization of a titanium foil.	Hydrogen atmosphere treatment	d = 100-200 nm l = 2-3 µm	2 times increase w.r.t pristine TiO_2 nanowires	95
Shell passivated Rutile TiO_2	Hydrothermal method	Atomic layer deposition	l = 0.28 − 1.8 µm	The epitaxial shell formation enhanced photocatalytic activity by 1.5 times.	96

Sample	Synthesis method	Surface treatment	Morphology	PEC properties	Reference
Surface disordered Rutile TiO_2	Hydrothermal method	Hydrogen atmosphere treatment	d = 100 − 200 nm. l = 2-3 µm	The photocurrent of H: TiO_2 is twice w.r.t pristine TiO_2 nanowires	97
Surface disordered anatase TiO_2 nanotube	Anodic oxidation process	$NaBH_4$ treatment	d = 100 nm l = 7µm	4 times increase in photocurrent	98
Surface disordered anatase TiO_2	Anodization	Anodization	d = 300 nm t = 75 nm	−	99
Surface disordered TiO_2 (mixed phase with more rutile)	Anodization process	−	d = 100 nm l = 900 nm	−	100
Surface passivated N doped rutile TiO_2	Hydrothermal method	−	d = − 5nm l = 4.4 µm	2.5 times improvement in the photocurrent	101
Surface passivated Anatase TiO_2	Hydrolysis process	−	d = 75-100 nm l = 1µm	The evolved H_2 from Gd^{3+} : TiO_2 is 180% higher than pristine TiO_2 electrode	93
Trap states passivated Anatase TiO_2	−	Passivation	−	−	94
Surface passivated Anatase TiO_2	Electrochemical	Anodization	d = 80nm l = 4.5 µm	Photocurrent density increase 3.6 times higher	102
Surface disordered anatase TiO_2	Template free chemical route	Hydrogen treatment	Average size is around 15 nm	Photocurrents increase 2-fold	103
Hydrogen treated rutile TiO_2 nanorod	Hydrothermal method	Treatment in H_2/ Ar atmosphere	d = 150 nm l = 1.8 µm	−	104

1.6.4 TiO_2: MoS_2 3D: 2D nanocomposites

MoS_2 is found in earth as a mineral named 'molybdenite'. In its bulk form, it is a dark and shiny solid and has a layered structure as described in Fig. 1.13 with crystal structure in different planes[105]. The weaker interlayer interactions in comparison to

bonding within a layer allows sheets to easily slide over one another and thus, it is often used as a lubricant. It can also be used as an alternative to graphite in high-vacuum applications, but it does have a lower maximum operating temperature than graphite. Similar to graphite, this also results in the possibility of formation of 2D layers by different methods. Bulk MoS_2 is a semiconductor with an indirect bandgap of ~1.2eV and is therefore of limited interest to the optoelectronics industry. Individual layers of MoS_2 have radically different properties compared to the bulk. Absence of interlayer interactions and confinement of electrons into a single plane or few plane results in the formation of a direct bandgap with an increased energy of ~1.89eV in 2D layers. The properties of MoS_2 layers can be modified by controlling the number of layers which makes it a very useful material for application as a 2D semiconductor. A single monolayer of MoS_2 can absorb 10% of incident light with energy above the bandgap[106].

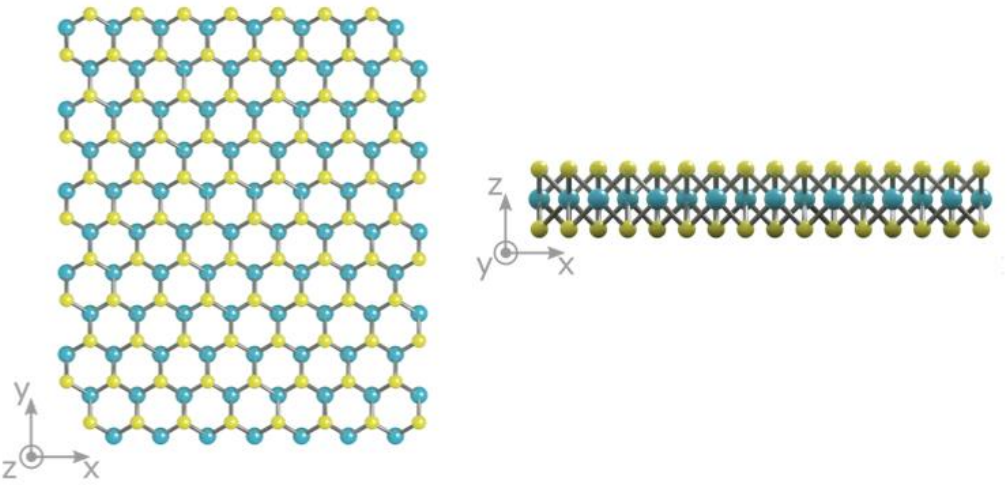

Figure 1.13: The atomic arrangement of monolayer MoS2 showing a 2D layer comprising of molybdenum atoms (blue) sandwiched between two layers of sulfur atoms (yellow) along two different crystallographic directions. (adapted from Ref. 105)

Due to the useful properties of TiO_2 as described earlier in terms of band edge alignment and stability and the attractive semiconductor properties of MoS_2 nanosheets, especially

in terms of 100% surface area and its narrow band gap, TiO_2:MoS_2 nanocomposite seems to have potentially useful properties for photocatalysis. TiO_2:MoS_2 composites have been prepared via a facile hydrothermal process[107]. The improved photocatalytic activities are perhaps derived from the high conductivity and increased active sites for the introduction of co-catalytic MoS_2 nanosheets as well as the positive synergetic effect between the TiO_2 and MoS_2. In another important study, 2D nanojunctions been used to enhance solar hydrogen generation of MoS_2/TiO_2 system[108]. Incorporation of 2D MoS_2 nanosheets on the surface of 2D anatase TiO_2 nanosheets greatly increased the interfacial contact and high H_2 evolution rate were observed. In another study a facile approach for the preparation of MoS_2 nanosheet decorated by porous titanium dioxide for effective photocatalytic activity has been used. Mesoporous titanium dioxide nanostructures is synthesized by a hydrothermal process using titanium (III) chloride and then the MoS_2/TiO_2 were prepared through mixing of MoS_2 nanosheet with mesoporous titanium dioxide under ultrasonic irradiation.

Loading of 2D MoS_2 nanosheets on the surface of 2D anatase TiO_2 nanosheets having (001) facets was observed to increase the interfacial area. In this reported study, it is shown that at an optimal ratio of 0.50 wt % MoS_2, the 2D-2D MoS_2/TiO_2 photocatalyst shows the higher H_2 evolution rate than that of pure TiO_2 nanosheets. The intimate contact and large area interface between the light-harvesting semiconductor and co-catalyst is assumed to be an important factor.

In another important study, 2D TiO_2/MoS_2 hybrid nanosheets have been prepared via a facile hydrothermal process[109]. The improved photocatalytic activities seem to be derived from the high conductivity and the increased active sites for the introduction of co-catalytic MoS_2 nanosheets as well as the positive synergetic effect between the TiO_2

and MoS_2. A summary of the synthesis and properties of TiO_2:MoS_2 nanocomposites is shown in Table 1.3.

Table 1.3: Synthesis and PEC properties of TiO_2:MoS_2 nanocomposites reported in literature

Sample	TiO_2	Method	MoS_2	Method	PEC Properties	Ref.
TiO_2: MoS_2	Porous TiO_2	Hydrothermal	MoS_2 nanosheet	Liquid Exfoliation Method	Photocatalytic performance is 2.2 times higher than mesoporous TiO_2	107
TiO_2:MoS_2 composite	TiO_2 nanoparticles	Solvo thermal	MoS_2	Solvo thermal	Visible light photodegradation TiO_2 = 48% TiO_2 /MoS_2 = 74%	108
TiO_2: MoS_2	TiO_2 nanosheets	MoS_2 2D layer	Hydrothermal reaction	Hydrothermal reaction with TiO_2	HER = 2145 µmol h^{-1} g^{-1}, which is about 36.4 times higher than that of pure TiO_2 nanosheets.	109
TiO_2:MoS_2	TiO_2	MoS_2 2D layer	Hydrothermal process	Mechanical exfoliation	The saturation current density = 33 µA cm^{-2} which is nearly twice that of pure TiO_2	110
MoS_2 @ TiO_2 heterojunction	TiO_2 nanosheet	Proton exchange reaction.	MoS_2 nanoparticles	hydrothermal	Photocurrent density 31.3 mA cm-2 which is about 26 times that of pure MoS_2.	111
TiO_2-MoS_2 nanocomposite	TiO_2 nano broccoli	Commercially obtained	MoS_2 nano sheets	Chemical method	Enhanced photochromic reactions	112
MoS_2/TiO_2 Composite Catalyst	TiO_2 nanoparticles	Hydrothermal method	MoS_2 nanosheets	Hydrothermal method	HPR= 1004 μmol^{-1}. h^{-1}. g^{-1}	113
TiO_2: MoS_2 hybrid pallets	TiO_2 nanoparticles	Wet impregration method	MoS_2 flakes	MoO_2:H_2S reaction at 673 K.	Enhancement w.r.t TiO_2	114
TiO_2/MoS_2 composite photocatalyst one-step hydrothermal process	TiO_2 vitreosol	Ultrasonic processing	Micro-MoS_2 powder	Ultrasonic treatment	Degradation rates of TiO_2, MoS_2-TiO_2 mixture, and TiO_2/MoS_2 composite = 28% , 27 % and 97%	115

TiO_2 – MoS_2 composite	TiO_2 nanoparticles	Solvothermal	MoS_2/Graphene composite	Commerial	High HPR 165.3 µmol h^{-1}	116

1.6.5 Synthesis and properties of TiO_2-$BiVO_4$ composites

Bismuth vanadate ($BiVO_4$) as a ternary oxide semiconductor has a narrow band gap of 2.4-2.5 eV and is a useful and a promising candidate as a photocatalyst owing to its high stability, non-toxicity, good tunability, and visible-light response[117-119]. It has been reported in a number of studies that $BiVO_4$ exhibit high photoelectric conversion efficiency over 40%[120]. Among four crystallographic forms (tetragonal ziroconium silicate, tetragonal scheelite, orthorhombic pucherite and monoclinic β-fergusonite) of $BiVO_4$, Monoclinic $BiVO_4$ is probably the most stable form and has shown high photo-catalytic activity[121]. In spite of its useful and attractive properties of visible light absorption due to its lower band gap, $BiVO_4$ exhibits an inefficient separation of photo-excited electron-hole pairs and thus, low photocatalytic efficiency[122]. As both efficient visible light absorption and efficient carrier separation are essential requirement for PEC applications. Therefore, it is essential to promote the separation of electron-hole pairs to improve the photocatalytic performances by combining it with other materials using different methodologies. It has been demonstrated that Cu doped $BiVO_4$ micro sheets exhibit better photocatalytic activity[123]. In another study, it has been shown that introduction of oxygen vacancy could assist in capturing of photo-generated electrons and thus, inhibit the electron-hole recombination[124]. The important methodology of forming composite structures of $BiVO_4$/TiO_2[125] and $BiVO_4$/graphene have been also been applied[126]. Main results on the synthesis and properties of TiO_2-$BiVO_4$ nanocomposite is given in Table 1.4.

Table 1.4: Synthesis and PEC properties of TiO_2:$BiVO_4$ nanocomposites as reported in the literature

Material	Synthesis TiO_2	$BiVO_4$ Synthesis two step chemical process	PEC	Reference
TiO_2- $BiVO_4$ nanocomposite	-	Hydrothermal process	TiO_2:$BiVO_4$ nanocomposites exhibit much high photocatalytic acitivites for water oxidation and H_2 evolution even by about three times compared to TiO_2-$BiVO_4$ one, along with the greatly-improved visible activity for pollutant degradation.	127
TiO_2- $BiVO_4$ nanoarray	TiO_2 nanorod hydrothermal method	$BiVO_4$ layer electro deposition	The photocurrent of the TiO_2:$BiVO_4$ nanorods reached ˜1.86 mA cm-2 at 1.0 V_{RHE} with an onset potential of 0.3V_{RHE}. Optimum photocurrent of ~1.86 mA cm2 at 1.0 VRHE with an onset potential as small as 0.3 VRHE and IPCE of 26% at 450 nm) was obtained for the TiO2/BiVO4/Co-Pi anodes	128
$BiVO_4$ – TiO_2 heterojunction	TiO_2 layer hydrothermal + chemical	$BiVO_4$ layer Metal organic decomposition	The $BiVO_4$/ TiO_2/FTO are superior to those of the $BiVO_4$/FTO photoanodes at only potentials >1.2 V vs RHE	129
TiO_2 – $BiVO_4$ films	TiO_2 NRs photoanode was hydrothermally synthesized directly onto a FTO substrate.	$BiVO_4$ was prepared by chemical method.	The TiO_2:$BiVO_4$ heterojuction photoanode can reach a high photocurrent density of 1.3mA cm^{-2} at 1.23 V vs. RHE, coupling with a low onset potential (0.18 V vs. RHE) under standard testing conditions.	130
Si/ TiO_2/ $BiVO_4$ Heterojunction	A thin film of TiO_2 by atomic layer deposition	$BiVO_4$ was deposited on various substrates (bare Si, TiO_2 deposited Si, bare FTO, and TiO_2depoisted FTO) following the same	With the assistance of the charge separation in the heterojunction films, Si/TiO_2/ $BiVO_4$ photoanodes showed 3.3 fold enhanced photocurrent density at	131

Material	Synthesis TiO_2	$BiVO_4$ Synthesis two step chemical process	PEC	Reference
		metal- organic decomposition method.	1.23 V versus RHE. In addition , its onset potential for the photocurrent shifted negatively by 300 mV compared to that of the FTO/ $BiVO_4$ photoanode.	
$TiO_2/BiVO_4$ composite	$BiVO_4$ samples were prepared by chemical method.	Different amounts of $(NH_4)_2TiF_6$ were added to the suspension individually and continually stirred for 30 min to get the precursors. The obtained samples were marked with pure $BiVO_4$, 20% $TiO_2/BiVO_4$, 50% $TiO_2/BiVO_4$ and 80% TiO_2/ $BiVO_4$	It is also found that the 20% TiO_2:$BiVO_4$ shows the best photocatalytic activity because of its high crystallinity, narrow band gap, and most importantly, the hierarchical heterostructure.	132
TiO_2- $BiVO_4$ Heterostructure	Monoclinic. $BiVO_4$ was obtained by chemical method	TiO_2 sphere were synthesized by sol-gel method and mixed with $BiVO_4$	High PEC efficiency for sensitive biosensing.	133
TiO_2/ $BiVO_4$ Nanowire	TiO_2 nanowire array.	$BiVO_4$ was deposited on the nanowire array by thermal evaporation of Bi metal, followed by heating in the presence of vanadyl acetylacetonate ($VO(C_5H_7O_2)_2$)	Electrochemical and spectroscopic measurements give evidence for the type 11 and alignment necessary for favourable electron transfer from $BiVO_4$ to TiO_2.	134

1.7 Objectives of the Present Study

The central objective of the present thesis work is to modify the properties of TiO_2 for photo-electrochemical applications by using different methodology of surface treatment, core shell nanoparticles and 2D-nanoparticle composites. Based on the discussion presented in the above section, the potential change in the properties of TiO_2 by using different methodologies is schematically described in the following Table.1.5.

Table 1.5: Different materials configuration used in the present study for modifying the properties and make them more suitable for photo-electrochemical applications.

Material System		Modification in Properties
Nanoparticle		• Blue shift in the band gap • Enhanced surface area • Effecting catalytic properties and stability
Surface modification of nanoparticles		• Modification in catalytic properties • Defect states in the forbidden gap
Core-shell nanoparticle formation		• Use of low band gap semiconductor • Band alignment for carrier separation
2D-nanoparticle composite		• Use of layer dependent properties • Large interface area

The main objective of this study is to understand how one can modify the properties of TiO_2 using different methodologies and to investigate how these modifications result in change in the optical, electrical and thus, the PEC properties. As discussed in the earlier sections, TiO_2 is one of the most well studied material systems for photo-electrochemical applications and thus, is a model material representing other oxide materials. Therefore, the methodologies used in the present study can be applied to other material systems as well. Following materials combination have been used to realize the methodologies given in Table 1.5.

1. TiO_2 nanoparticles and the optical and structural properties have been modified by hydrogen treatment.
2. MoS_2-TiO_2 2D:3D nanocomposite. It is expected that the large interface between 2D materials and nanoparticle will result in large change in the optical absorption and efficient charge separation at the interface.

3. TiO_2-$BiVO_4$ core-shell nanoparticles. PEC properties of the core-shell nanoparticles have been compared w.r.t $BiVO_4$ and TiO_2 nanoparticles.

Chapter 2

Characterization Techniques

In this chapter, details of techniques used to characterize structural, optical and electronic properites of nanoparticle samples are presented. Methods used to investigate the interface and junction properties are summarized. Methods of synthesizing nanoparticles and its composite are also presented.

2.1 Glancing Angle X-ray Diffraction

X-ray diffraction technique is used as crystal structural characterization of nano and bulk materials. Standard values corresponding to the choosen material by matching the experimentally obtained atomic spacing with the material were compared[135]. X-ray diffraction provide valuable information such as, the crystal structure, lattice parameters, preferred orientation of a crystalline sample, phase purity, crystallite size and strain[135]. In the present study, crystal structure and crystatllite size have been determined and are explained below. In a typical X-ray diffractometer, the intensity of the diffracted X-ray is measured as a function of angle 2Θ, according to the Bragg's law (equation 2.1)[136].

$$2d \sin(\Theta) = n\lambda \qquad \ldots\ldots\ldots\

atomic planes with spacing d. As shown in Fig 2.1, 2d Sin Θ is the path difference between the two waves reflected from two consecutive planes.

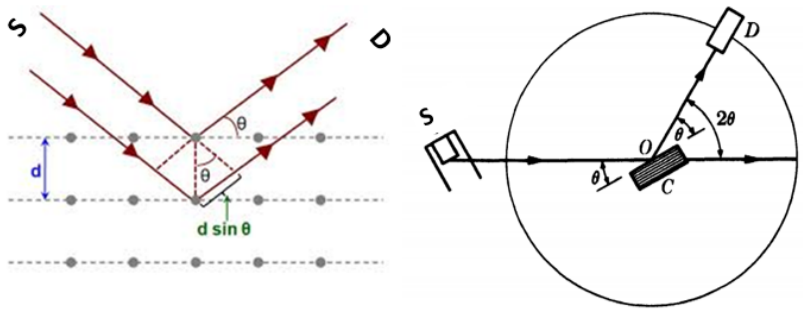

Figure 2.1: A schematic diagram showing the principle of diffraction from a lattice having d as the interplanar spacing. The geometric arrangment used in the experimental set-up for realizing the diffraction condition is also shown. S, D and C are X-ray source, detector and sample, respectivlty. (Adapted from Ref. 136).

Philips X'pert PRO MPD was used in θ–2θ geometry to study the crystal structure of different samples. An operating current of maximum 40 mA at a voltage of about 40 kV is used to produce the X rays. The diffraction pattern was recorded in 2θ range of 20 degree to 80 degree by keeping a step size of 0.04 degree and integration time of 0.01 seconds. A typical set up in the X-ray diffractometer is shown in Fig. 2.2. The soller slits with an angular width of 0.04 radians was used to control the axial divergence of incident X rays and divergence slit of 0.5 degree is used to control the irradiation of the sample surface. The structural properties of TiO_2 nanopraticles, TiO_2-MoS_2 nanocomposites and TiO_2-$BiVO_4$ core-shell nanoparticles were studied by comparing the experimentally observed 2θ values of different diffraction peaks and inter planar spacings with the corresponding JCPDS data. (Joint Committee on Powder Diffraction Standards).

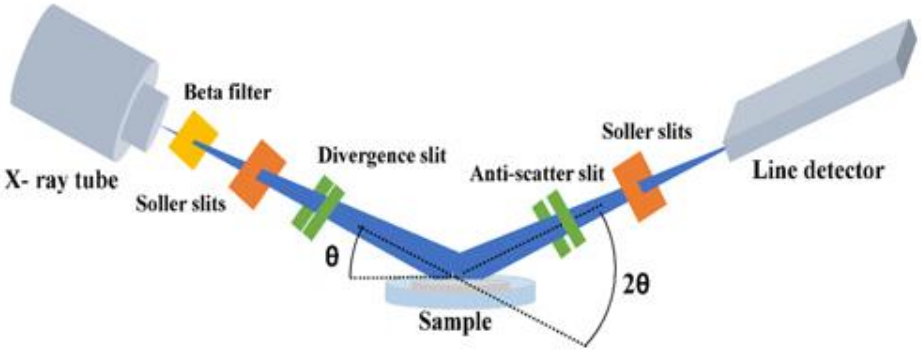

Figure 2.2: A schematic diagram showing important components and their arrangement in X-ray diffraction set up used in the present study. (Adapted from Ref 137 and 138)

In this study, crystal structure is determined using XRD studies by matching the experimentally determined 2 Θ values of the XRD peaks and corrrespoonding d values with the the JCPDS data. For example, in case of TiO_2, the extperimental data (2 Θ and intenstiy) is compared with that from the JCPDS data of probable phases of TiO_2 namely, Anatase, Brookite and Rutile. An amorphous material yields a broad hallow, whereas sharp peaks were observed in case of polycrystalline materials. The crystalline materials were identified by their unique diffraction patterns comprising of peaks for each *hkl* values upon exposure to monochromatic X-ray (Cu Kα = 1.54 A°).

The recorded X-ray diffractograms were used for the estimation of crystallite sizes using Scherrer equation[139,140], which is given as equation 2.2

$$\delta r = \frac{K\lambda}{\beta\cos\theta} \qquad \ldots\ldots\ldots\ldots\ldots\ldots\ldots\ldots\ldots\ldots\ldots\ldots\ldots\ldots\ldots\ldots\ldots\ldots\ldots\ldots\ldots\ldots(2.2)$$

Where δr is the crystallite size (average radius of the crystallite size), K is the dimensionless shape factor, β is the line broadening at FWHM and Θ is the Bragg angle.

2.2 X-Ray Photoelectron Spectroscopy

X-ray photoelectron spectroscopy is the surface analytical technique used to analyse the surface of thin film and nanostructured materials[141]**.** The changes in the stoichiometry of samples as a function of growth techniques have been studied by using X-ray photoelectron spectroscopy (XPS). The XPS technique is based on the principle of photoelectric effect, involving illumination of the sample surface with monochromatic X-rays resulting in photoemission of electrons from the atoms of the host material (Fig 2.3) The photoemitted electrons are characterized in terms of energy and intensity and the resulting data is displayed in terms of intensity as a function of energy. Zero energy refers to the Fermi energy of the sample and each peak corresponds to the binding energy of different electrons.

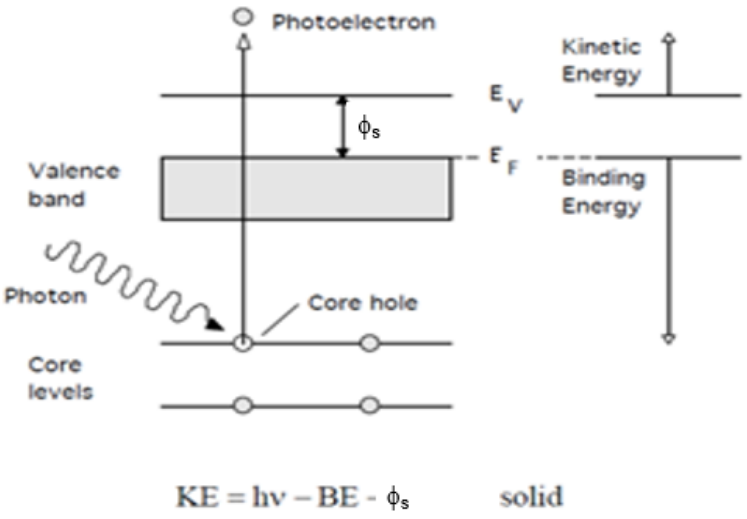

Figure 2.3: XPS schematic diagram showing the emission of photoelectron with kinetic energy as photon incident on the material provides the required energy for electron emission. (Adapted from Ref 142).

XPS is a highly surface sensitive technique as the useful signal comes only from top 10-25 Å and electrons photoemitted in the depth of the sample are not able to reach the detector and are scattered or absorbed in the bulk of the sample under investigation. As

the binding energy of an electron changes due to the change in chemical bond formation, alloying or oxidation. XPS with excellent energy resolution can be used to measure these energy changes and thus, obtain more information about the sample in addition to composition of the material. The changes or shift in binding energy is of the order of 0.1 to 10 eV. The specimen is irradiated with X-rays of known energy, hν and electrons of binding energy E_B are ejected. The kinetic energy (E_k) of the ejected electrons as measured by spectrometer is given by the following equation 2.3, where ϕ_s and ϕ_{sp} are the work functions of the specimen and spectrometer, detector material, respectively[143]. As shown in Fig. 2.3, the measured kinetic energy of electrons can be converted into the corresponding binding energy by the equation:

$$E_k = h\nu - E_B - \phi_s - \phi_{SP} \quad \text{.....(2.3)}$$

Zero of the XPS scale corresponds to the Fermi energy of the samples and each peak corresponds to the binding energy of the electron in different energy levels of the consistent atoms of the sample. As shown in Fig. 2.4, essential components of XPS technique include a X-ray source, a sample under investigation, an electron energy analyser and an electron detector and a signal multiplier, all maintained under ultra-high vacuum, and suitable electronics to convert the detected current into a spectrum. In the present study, X-ray photoelectron spectrometer (Perkin Elmer-1257), which includes a hemispherical section analyser with 25 meV resolution has been used. The set up consist of a dual anode X-ray source, capable of producing Mg K_α or Al K_α X-rays.

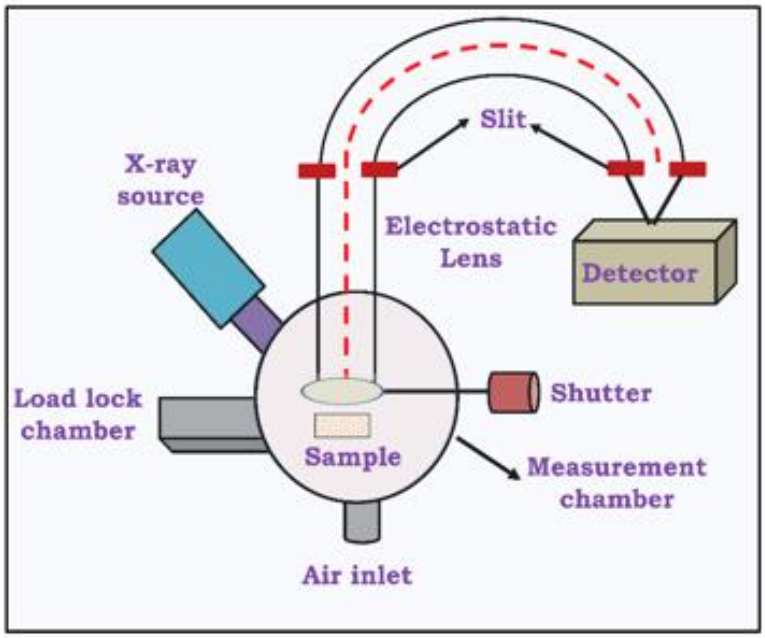

Figure 2.4: A schematic description of XPS set up showing different components (Adapted from Ref. 144)

As already mentioned, XPS is a surface sensitive analytical technique and any surface contamination or surface oxide can interfere with the sample analysis. Therefore, during XPS measurements, sputter ion cleaning of the samples is carried out using 4 KeV Ar^+ ions generated from an ion gun. Ion bombardment during surface cleaning can also damage the sample and alter the chemical composition or chemical state of different elements and therefore, precaution should be taken in terms of the ion energy and irradiation time used during the surface cleaning.

2.3 Raman Spectroscopy Technique

Raman spectroscopy technique is based upon the interaction of light with the materials under investigation[145]. The principle of the technique is based on Raman effect and is used to determine vibrational modes of different atoms. If a radiation of given frequency is incident on a material and gets scattered elastically without undergoing any change in frequency, this is termed as Rayleigh scattering. In case of inelastic scattering, the frequency of radiation gets modified on its interaction with the material.

Scattered radiation has a different frequency and this scattering is classified as Raman scattering. If frequency of scattered photon is lower than the incident photon, it is known as Stokes frequency and if scattered photon possesses frequency higher than the incident photon, it is termed as anti-Stokes scattering (Fig. 2.5). The difference between the output and input light provides the information of vibrational modes, which are signature of materials properties.

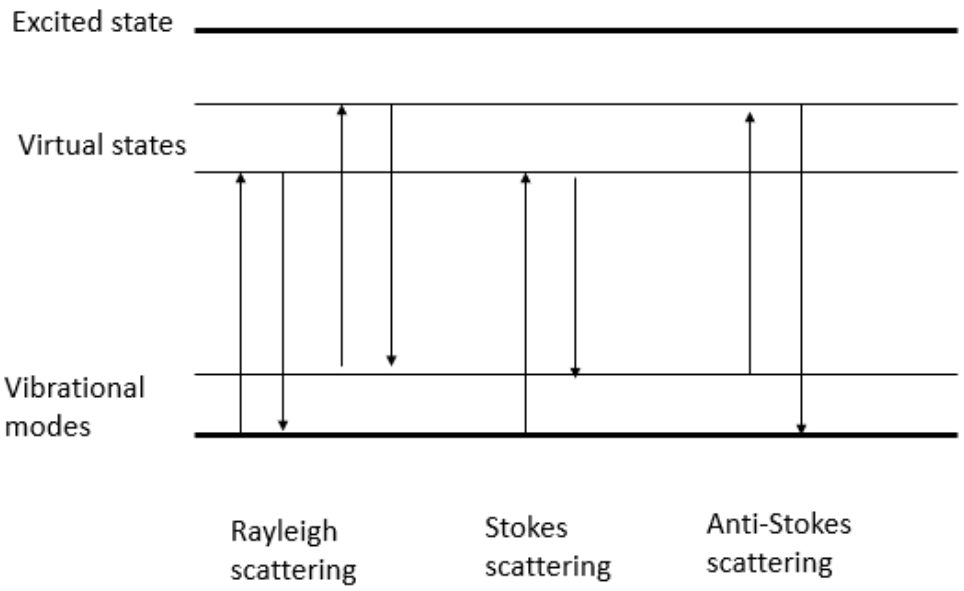

Figure 2.5: A schematic description of Raman effect showing the emission of stokes (lower energy than the incident photons) and anti-stokes line (higher energy w.r.t incident energy). Rayleigh scattering in which no change in wavelength takes place is also shown. (Adapted from Ref. 146)

Horiba Scientific Lab RAM HR Evolution Raman spectrometer is employed for Raman measurements in the present thesis. In the present study, Raman spectra have been recorded with Ar ion laser of wavelength 514 nm. A standard schematic diagram of a Raman spectroscopy setup used in the present investigation is given in the Fig 2.6.

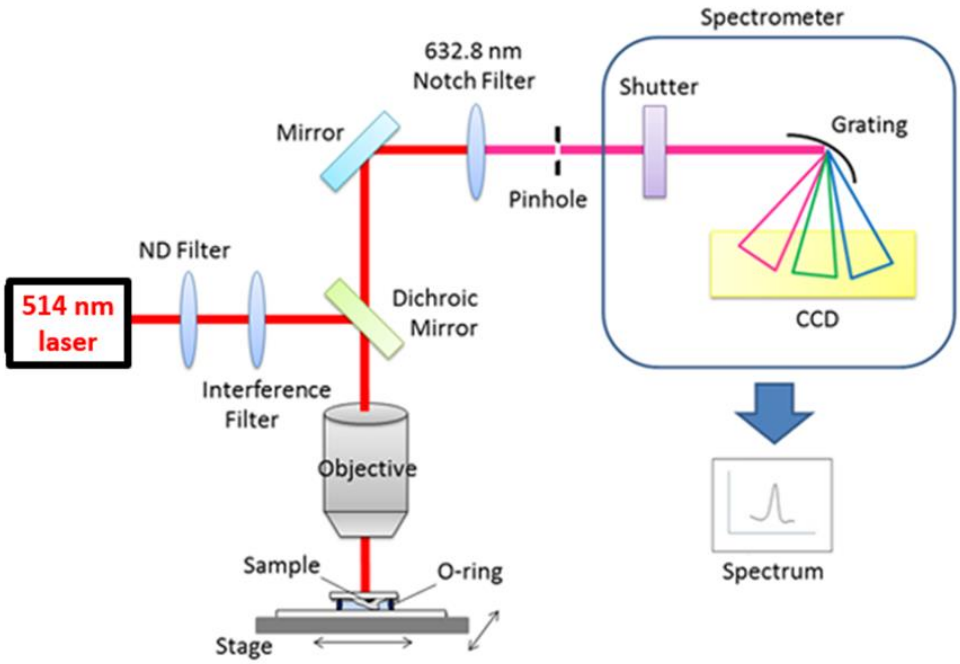

Figure 2.6: A schematic diagram of Raman spectroscopy set up showing the path of laser energy and different components. (Adapted from Ref. 147)

The excitation laser light from the laser source travels within on optical fibre and passes through expanding lens and band pass filter (L3 and F2), respectively as shown in Fig. 2.6. The dichroic mirror (BS) reflects the laser light which is made incident on the sample after passing through lens L2. After the laser light and sample interaction, back scattered light passes through lens L2 for collimation, dichroic mirror BS and holographic rejection filter F1. In the last step, the laser light passes through the spectrograph and charge coupled CCD detector. Finally, the results are shown on the computer monitor.

2.4 Photoluminescence Measurements

In this study, Photoluminescence (PL) measurements have been performed using Horiba Scientific Raman microscope fitted with He-Cd laser of wavelength 325nm. PL spectroscopy is a non-contact, non-destructive method of probing the electronic structure of materials[148]. Similar to Raman spectroscopy, higher energy photons (than

the band gap of the material under investigation) are directed onto a sample. Light is absorbed and photo-excitation occur with the excitation from valence band to conduction band of the material. For electron promotion to occur the laser photon energy must be the same or higher than the material band-gap. The photo-excitation causes the electron transfer to a higher electronic state. As electron relaxes and returns back to a lower energy levels with the emission of light. Photoluminescence technique is used to characterise electronic structure of the materials and states in the forbidden band gap of the semiconductor. It is important to note that due to bulk defects, impurities and surface defects, electrons jump from conduction band to defect states and then from defect states to valence band. Therefore, PL spectra also contain PL peak corresponding to electron emission from conduction band (CB) to valence band (VB) defect states to valence band (VB). As shown in Fig. 2.7. photoluminescence peak due to electron emission from conduction band (CB)-valence band (VB) is called band gap emission and the electron emission from defect state to valence band (VB) is termed as defect emission. In this work, Horiba scientific LabRam HR Evolution photoluminescence setup having He-Cd 325 nm laser has been used to perform photoluminescence measurements in the samples. The schematic diagram of the experimental setup of the photoluminescence spectrophotometer was shown in figure. Laser beam is made incident on the sample under investigation after passing through a filter. As discussed earlier, absorption of incident light and its re-emmission in the form of band to band or defect related light emmission passes through a condenser lens system, monochromator, and a PMT detector. Monochromator and PMT detector assembly results in measurement of photoluminescence intensity as a function of wavelength.

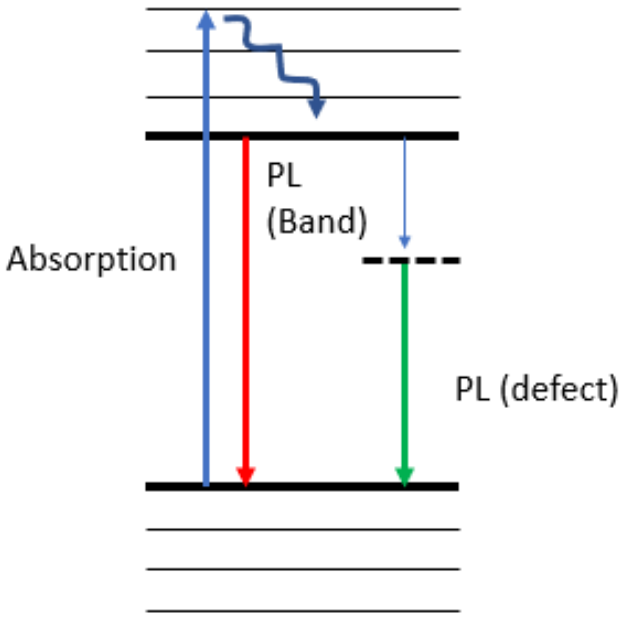

Figure 2.7: A schematic diagram showing the absorption of high energy incident photon taking the electron from valance band to conduction band. The excited electron relaxes to the bottom of conduction band. The photon emission due to de-excitation of electron from conduction band to valence band results in band edge PL emission. In the present of defect states PL emission can take place at lower energy due to de-excitation to the defect state followed by relaxation to valence band. (Adapted from Ref. 149).

2.5 Scanning Electron Microscopy

In the present study, FEI Quanta's 3D scanning electron microscope is used. The basic principle is that a beam of electrons is generated by a field emission gun. The electron beam is accelerated through a high voltage region and pass through a system of electromagnetic lenses to produce a focused beam of electrons. The narrow and focussed beam scans the surface of the specimen by means of scan coils. Electrons emitted from the specimen by the action of the scanning beam and collected by a suitably positioned detector[150]. A schematic diagram showing important parts and operation of scanning electron microscopy is shown in Fig 2.8. The output signal of the electron detector is used to make an image of the surface of the sample under

investigation. The brightness of the spot on the screen corresponds to more electrons being emitted from a particular feature. Similarly, the darker spot represents lower concentration of electrons being received from a particular region of the sample surface. Different types of process takes place during the interaction of incident electrons with target atoms of the surface. Depending upon which electrons are detected and used for constructing the image, there are different modes of operation of scanning electron microscope. The two most common are the secondary electron image (SEI) and the back scattered electron (BSE) image. The SEI is commonly used to study the surface topography features and is a high-resolution mode. The contrast in the BSI is dependent on the atomic number of the atoms constituting the specimen and this mode is useful to have information about the chemical composition of the sample[151]. It needs to be mentioned that the contrast and resolution of different modes are sensitive to operating conditions, which need to be take into account.

In addition to the secondary and back scattered electrons, X-rays are also emitted during the incident electron- solid surface interaction. Measurement of the intensity of X-rays having different energy emitted from different atoms constituting the sample is known as energy dispersive. X-ray microanalysis gives the composition of the micro and nano features in the SEM image. The spatial resolution of the EDX analysis depends upon the area surrounding the spot where incident electron interacts with the sample, from where the X-rays are emitted. The spatial resolution of EDX mode is poorer than that of SEI or BSE image, where the resolution depends upon the spot size of the electron beam. The intensity of a particular X-rays having a characteristic energy represent the relative concentration of that element[152].

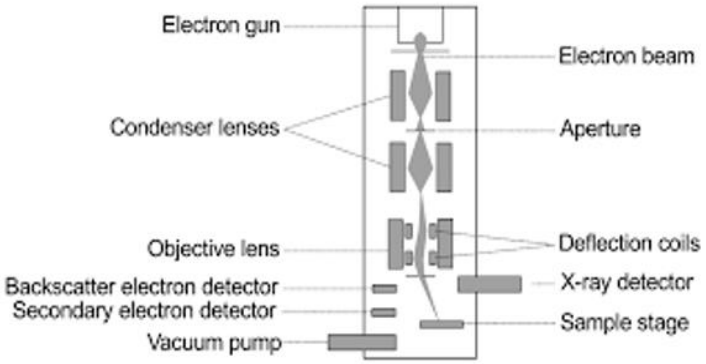

Figure 2.8: A schematic diagram showing the different part of a scanning electron microscope having EDX attachment. (Adapted from Ref. 153).

2.6 Transmission Electron Microscopy

Similar to scanning electron microscope, described above, transmission electron microscopy is also based on utilizing a focussed ion beam[150]**.** In contrast to SEM, focussed ion beam interacts with the sample, and the transmitted beam of electrons is used to construct the image. A modern TEM typically comprises of a vacuum system, and control panels as shown in Fig. 2.9.

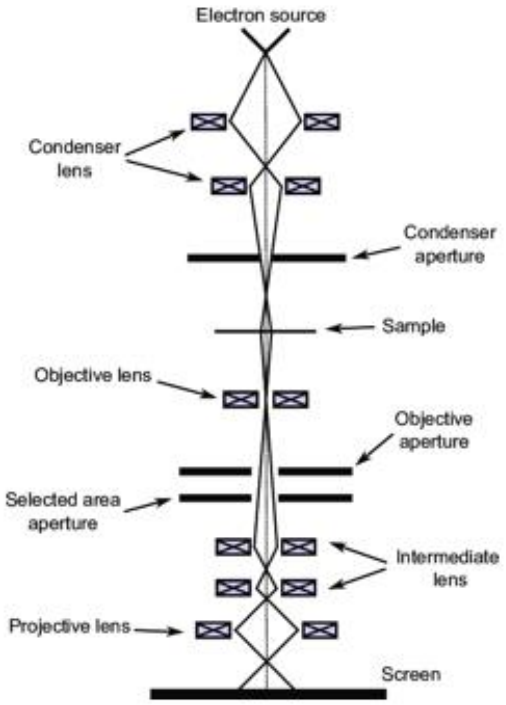

Figure 2.9: A schematic diagram showing the basic part of a transmission electron microscope and the electron path (Adapted from Ref. 154).

The electron column includes elements analogous to those of a light microscope. The light source of the light microscope is replaced by an electron gun, which is built into the column. The glass lenses are replaced by electromagnetic lenses. Unlike glass lenses, the power (focal length) of magnetic lenses can be changed by changing the current through the lens coil. The eyepiece is replaced by a fluorescent screen and/or a digital camera. The electron beam emerges from the electron gun, and passes through a thin specimen. Electrons transmitted from the sample are collected, focused, and projected onto the viewing device at the bottom of the column. The entire electron path from gun to camera must be under vacuum[155].In the present study, FEI Technai G20 having a Lab 6 filament operating at 200 KeV is used in the present study

The advantage of the technique is that it is capable of very high magnification and resolution (about an order of magnitude better than SEM). The key disadvantage is that it can only be used for very thin samples (less than 20 nm thickness). Sample preparation which involves transferring the sample onto a copper grid or transforming a bulk sample to a thin slice and subsequently transferring it to the TEM grid is an important part of the TEM investigation. In the present study, nanoparticle powder was dispersed onto Cu grid by drop casting method.

As shown in the schematic diagram in Fig. 2.10, a small quantity of nanoparticles to be analysed are dispersed into ethanol solution by ultrasonication. With the help of a dropper, ethanol-nanoparticles dispersion is drop-casted onto the Cu grid placed on the parafilm paper. This helps in easy transfer of the TEM grid after sample preparation is completed. The ethanol solution evaporates and the nanoparticle sample onto the Copper grid are dried in the presence of hot air from an electrical drier. TEM grids having nanoparticles is viewed under an optical microscope for general inspection and kept in a high vacuum system for degassing before inserting into HR-TEM for analysis.

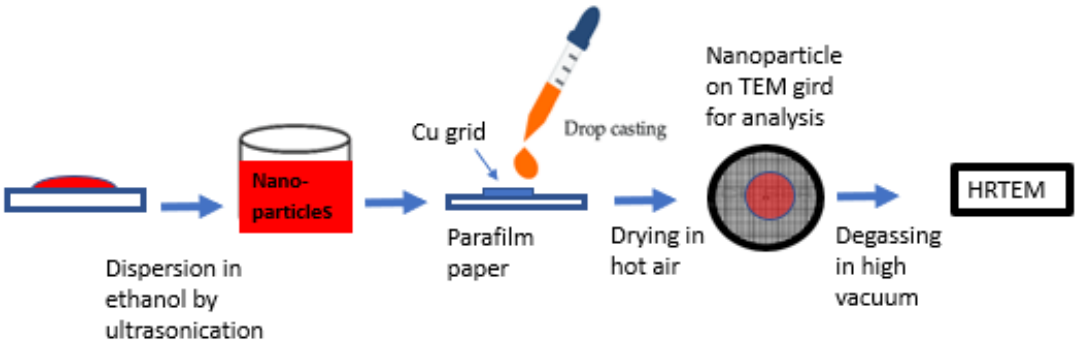

Figure 2.10: Different steps used for dispersing nanoparticles onto TEM grids for TEM sample preparation.

2.7 Photo-electrochemical Measurements

In the present study, photo-electrochemical measurements were performed on different samples to study the improvement in PEC response. For measurements, a photo-electrode is formed using a standard procedure of attaching an electrode and sealing the electrode by epoxy resin. A well-defined area of the sample is left exposed and the remaining part is covered with the epoxy. A small length of copper wire in the form of the loop is attached to the back side of sample pellets which is then covered with silver paste. The sample is left to dry and the formation of Ohmic contacts is checked. The electrode, silver paste and the back side of the sample and its edges are thoroughly sealed using commercially available non-conducting epoxy resin. The exposed area of about 0.5 cm radius forms the photo-electrode which is now ready for photo-electrochemical measurements. Different steps of electrode preparation are schematically described in Fig. 2.11.

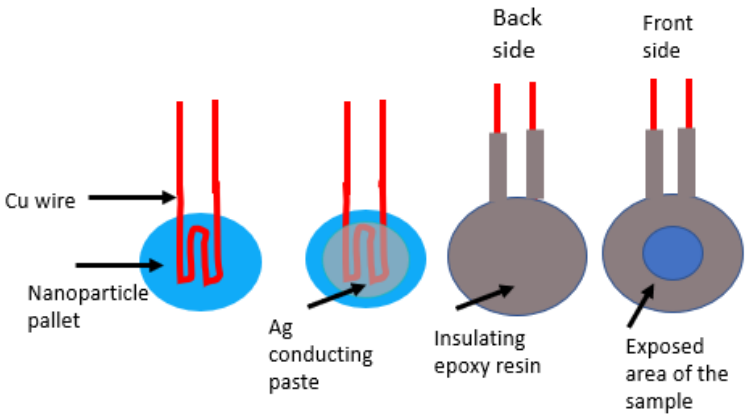

Figure 2.11: Different steps used for the prepration of photoelecrodes using different nanoparticle sample investigated in the pesent study. The steps involve attachment of the copper wire with the sample pallet using conducting paste, insulating the electodes and sample edges and defining the active area of the sample for PEC measurements

Photo-electro-chemical measurements of the electrodes made from different samples were carried out using linear sweep voltammetry and a PEC cell in a three-electrode configuration as shown in Fig. 2.12. Working electrode was prepared from these samples under investigation, a platinum wire as a counter electrode and Ag/AgCl were used as a standard reference electrode. One molar solution of NaOH, 0.5 molar solution of Na_2SO_4 aqueous solutions were used as an electrolyte for photo-electro-chemical measurements. Autolab PEC workstation with Nova software systems (X/POT Potentiostat) was used for photo-electro-chemical measurements. Linear sweep voltammetry measurements were performed in potential range -1.0 volt to + 1.0 volt versus Ag/AgCl with a scan rate of 10 millivolts per second. Measurements under dark conditions were carried out by covering a photo-electro-chemical cell with a black screen and light measurements were carried out by exposing Photo-electro-chemical cell to 280 W Xenon lamp filtered with AM 1.5 optical filter resulting in output light intensity of 100 milliwatt per cm^2. The photocurrent was calculated from the difference between light current and the dark current and the photocurrent density was obtained

by dividing the photocurrent by the exposed active area of the photo-electrode (radius= 0.5 centimetres).

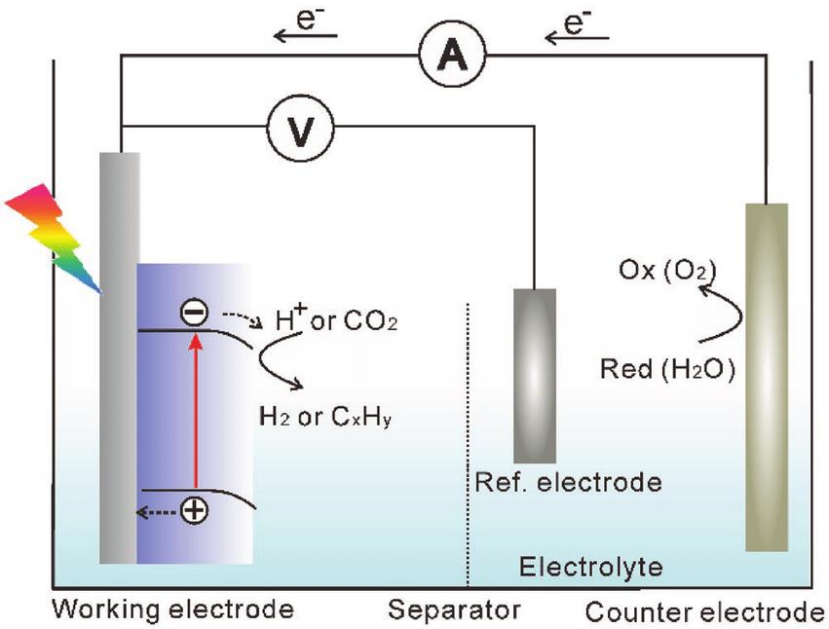

Figure 2.12: A schematic diagram showing the 3-electrodes configuration for PEC measrurements (Adapted from Ref. 155)

2.8 Electrochemical Impedance Spectroscopy

Electrochemical Impedance spectroscopy (EIS) is an important method to study the dielectric and transport properties of the materials and electrochemical reaction mechanism which is directly relevant for this study[156,157]. The electrochemical impedance is a complex resistance which comes into picture when the electric current flows through a material connected to a device with equivalent circuit having resistance and capacitor or inductor. It is complex due to phase difference between applied voltage and the current flowing in the equivalent circuit with real and imaginary parts (-Z" and Z'). Electrochemical impedance spectroscopy is widely used to probe interface charge transfer processes within the photo-anodes. The EIS plot (-Z" vs Z') is known as the Nyquist plot. The EIS Nyquist plots normally consist of a semicircle portion representing the charge transfer limiting process and a linear part observed from the

diffusion limiting step of the electrochemical process. The semicircle diameter gives the value of R_{ct} at the electrode/electrolyte interface. The smaller value of R_{ct} (charge transfer resistance) indicates long lifetime of photogenerated carriers and improved charge transfer ability, indicating an enhanced PEC response. In opposite case of semicircle with larger diameter, indicates poor charge transfer at the interface and material will not be suitable for photo-electro-chemical applications. In the present work, the electrochemical impedance measurements were carried out in a three electrode PEC cell comprising oxide samples as a working electrode, platinum mesh as a counter electrode, and standard Ag/AgCl (3M KCl) as a reference electrode in the potentiostat (AutoLab PEC workstation with nova software). The 0.1 M Na_2SO_4 (Ph-7) was used as an electrolyte. All the impedance measurements are performed in the frequency range of 10 mHz to 100 kHz. These conditions are similar to those prescribed for photo-electro-chemical measurements.

2.9 Mott-Schottky Analysis

To determine the flat band potential (V_{fb}), capacitance (C) is determined in the dark condition from impedance measurements in the three-electrode configuration based on equation 2.4

$$1/C^2 = (2/q\varepsilon_0 \varepsilon s\ N)\ (V_{fb} - kT/q) \qquad \ldots\ldots\ldots\ldots\ldots\ldots\ldots\ldots\ldots\ldots\ldots\ldots (2.4)$$

The above equation represents the bias voltage dependent capacitance of the junction assuming a one sided, abrupt and sharp junction at semiconductor/ electrolyte interface[158]. Any deviation from this will result in changes in the slope or X-axis intercept of the line represented by the above equation. Surface roughness, presence of surface or interfacial layer can thus, influence the results obtained from the above equation[156].

Linear variations of I/C^2 with applied potential (V_{app}) plot is called Mott-Schottky (MS) curves. Here, q is the elementary charge, ε_0 and ε_s are permittivity of the vacuum and dielectric constant of semiconductor electrode, respectively, V_{app} is the applied potential and K is the Boltzmann's constant, T is the absolute temperature and (kT/q) is a temperature dependent term. In the present study, capacitance at junction was measured with varying potential at 1 kHz signal frequency. The intercept of the linear portion of the MS plot on the potential axis yieldes the value of V_{fb}

2.10 Synthesis of Nanoparticles

The growth process used in the present study is the hydroghermal process. Hydrothermal synthesis is a commonly used method for preparation of different types of nanomaterials based on solution reaction-based approach[159]. The hydrothermal method involves crystallizing a substance at a high temperature and high vapor pressure using an aqueous solution. The process is carried out in autoclaves under controlled temperature and pressure. It allows the use of temperatures above the boiling point of water/organic solution. Autoclaves are hermitically sealed steel vessels that can withstand high temperatures and pressure for long durations. The vessel must be chemically inert and must not take part in the hydrothermal process. In the present study a stainless-steel vessel having a Teflon cylinder is used, as shown in Fig. 2.13. There are significant advantages of hydrothermal synthesis method over others such as thhe compositions of nanomaterials to be synthesized can be well controlled in hydrothermal synthesis through liquid or multiphase chemical reactions. The advantages of the hydrothermal method are its simplicity and easy variation of process parameters to obtain desired morphology.

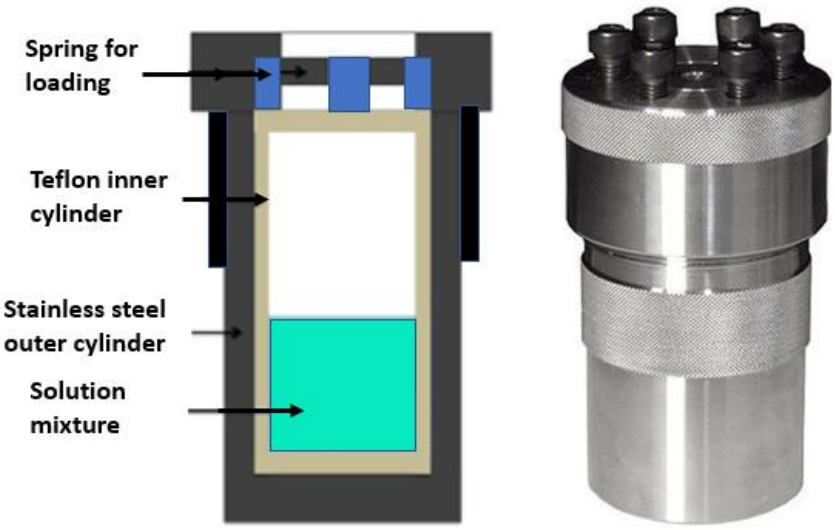

Figure 2.13: A schematic description and a photographic view of the autoclave used in the present study for hydrothermal synthesis of nanomaterials.

2.10.1 Synthesis of TiO_2 nanoparticles

In the present study, pristine TiO_2 nanocrystals were prepared using titanium tetra-isopropoxide solution, ethanol, hydrochloric acid and de-ionized water [160n]. 25 ml of deionized water mixed with 1 ml of hydrochloric acid and added slowly to 10 ml of titanium tetra-isopropoxide with continuous stirring in an ice bath. A white precipitate obtained was filtered and heated in air at 80^0C to evaporate extra water. After water evaporation, the product was sintered at 400^0C for 4 hours. For the hydrogen treatment under partial pressure, the annealing chamber was evacuated to $2.0x10^{-6}$ torr and subsequently at a gas flow rate of 20 sccm 5% H_2 balanced Ar was introduced into the chamber while maintaining the chamber pressure at $2.0x10^{-2}$ torr. The annealing temperature was maintained at 300^0C for 10,20 and 30 hours followed by cooling period of 1 hour. The schematics of growth process is described in Fig. 2.14

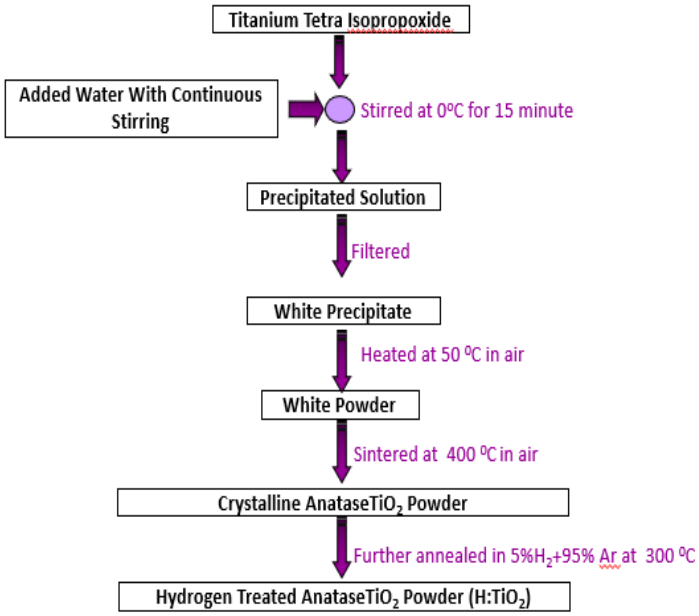

Figure 2.14: Different steps describing the preparation step used in the present study for growth of TiO_2 nanoparticles.

2.10.2 Preparation of MoS_2 nanoflakes

In the present study, MoS_2 nanoflakes were prepared by a wet chemical method. In a typical synthesis process, 2.42 grams of sodium molybdate ($Na_2MoO_4.2H_2O$), 2.12 grams of thiourea (NH_2CSNH_2) were dissolved in 80 ml of deionized water under vigorous stirring for 20 minutes. A small amount of PEG-1000 (polyethylene glycol) 0.28 grams was added to the solution. A clean Teflon container was rinsed with ethanol solution and deionied water. Before putting the above mixture of salts into the Teflon container, it was magnetically stirred in a beaker. Then autoclave instrument was rinsed with ethanol or propanol solution to avoid any contamination. Salt mixtures was kept in a 120 ml Teflon vessel container and was put in an autoclave at 180^0 C for 24 hours. After the cooling down phase, the autoclave containing black precipitates of MoS_2 nanoflakes were obtained. The resulting black precipitate was washed several times with ethanol and deionized water to further remove contaminants and impurities. The sysnthesis process is schematically described in Fig. 2.14.

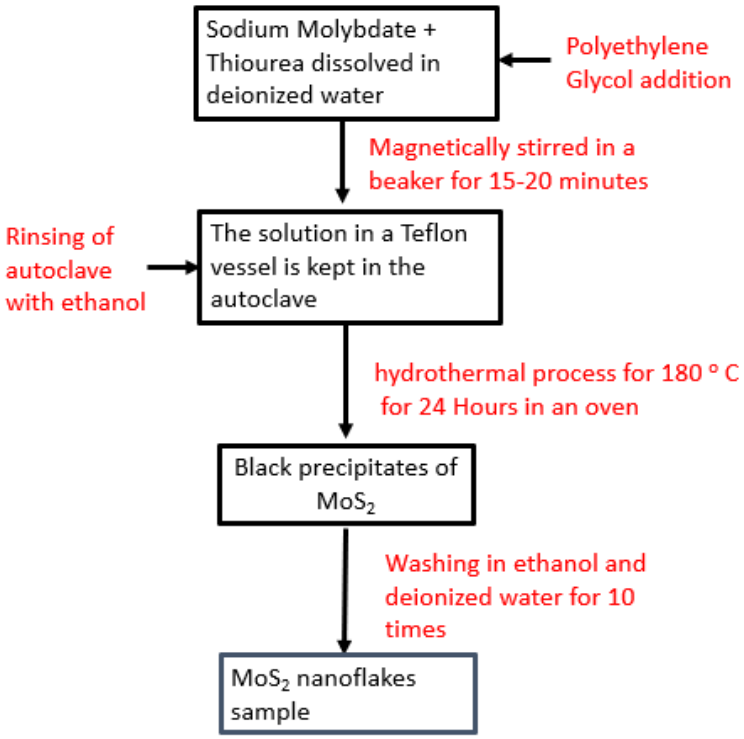

Figure 2.15: Schematic description of different steps used in the growth of MoS_2 nanoflakes in the present study.

2.10.3 Preparation of MoS_2-TiO_2 nanocomposite

For the preparation of MoS_2-TiO_2 nanocomposites, as prepared TiO_2 nanoparticles was loaded with 2.5, 5.0, 7.5 and 10.0 wt% of MoS_2 nanoflakes and sintered at 400^0 C for 4 hours. For example, for preparation of MoS_2-TiO_2 samples containing 7.5 % by weight of MoS_2 and 10 % by weight of MoS_2, 262 milligrams of TiO_2 was mixed with 18.59 milligrams of MoS_2 nanoflakes. For preparation of TiO_2-MoS_2 (10 % by weight) sample, 524 milligrams of TiO_2 nanoparticles was mixed with 53.14 milligrams of MoS_2 nanoflakes. For loading, required quantities of MoS_2 nanoflakes and TiO_2 nanoparticles were mixed in ethanol and ultrasonicated. The obtained nanocomposites were pelletized with dye of one cm diameter. The pellets were then sintered at 400^0 celsius for 4 hours in the furnace.

2.10.4 Preparation of $BiVO_4$ -TiO_2 nanoparticles

The sol-gel process is a method used for preparing solid materials from molecules. This method is used for the fabrication of metal oxides. This process involves conversion of monomers into a colloidal solution (sol) that acts as the precursors for an integrated network of either polymers or discrete particles. Metal alkoxides are the typical precursors used for this process.

$BiVO_4$ nanoparticles were prepared by hydrothermal method at high temperatures in excess of 400^0 C. For the preparation of $BiVO_4$ nanoparticles, the required quantities of bismuth nitrate penta-hydrate were dissolved in required volume of deionized water in acidic medium, whereas required quantities of ammonium meta-vanadate were dissolved in 50 ml of de-ionized water with known quantities of sodium hydroxide flakes in deionized water. After adding some quantities of sodium dodecyl benzene sulphonate to each of the solutions and then magnetically stirred, the two solutions were mixed and stirred again for 30 minutes. The obtained mixed solution was kept in a Teflon lined vessel for hydrothermal treatment. Then the prepared nanoparticles were filtered from the solution using a centrifuge and then dried to obtain $BiVO_4$ nanoparticles. Titanium tetra iso-propoxide solution was taken in an ice bath. $BiVO_4$ nanoparticles are added to the above solution and then magnetically stirred for 3-4 hours and filtered and dried to obtain core-shell $BiVO_4$-TiO_2 nanoparticles. Different steps and the growth sequence is shown in Fig. 2.15.

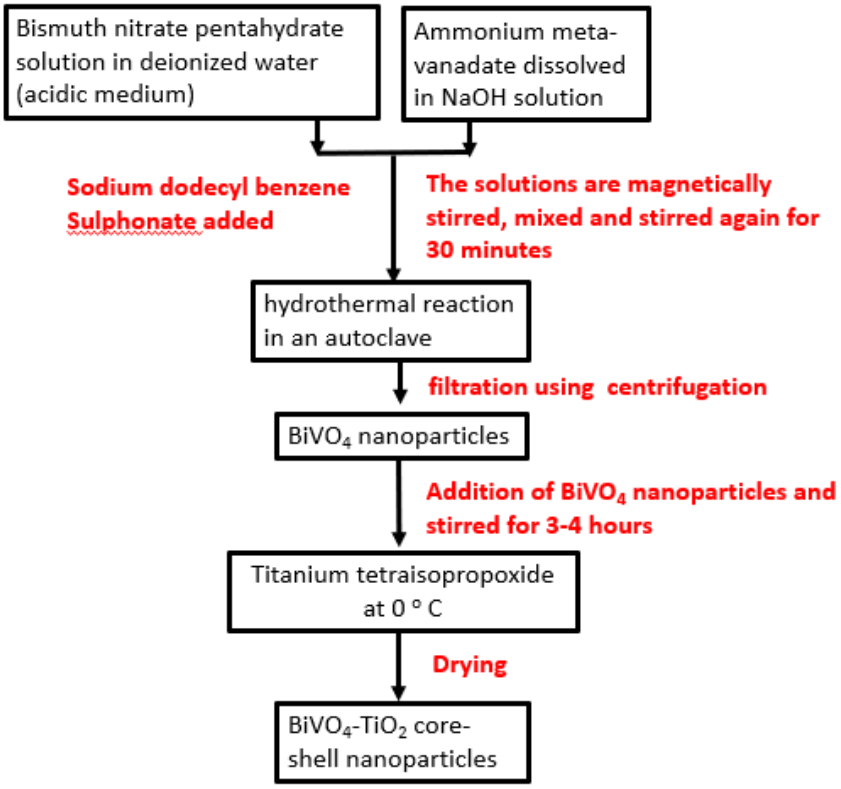

Figure 2.15: Growth sequence used in the present study for the growth of $BiVO_4$-TiO_2 core shell nanoparticles

Chapter 3

Structural, optical, electronic and PEC properties of hydrogenated TiO_2 nanoparticles

3.1 Introduction

In this chapter, the results on the effect of vacuum hydrogen annealing of TiO_2 nanocrystals (H:TiO_2) on the structural, optical and electrical properties and the resulting changes on the improved photocatalytic and photo-electrochemical performance are reported. In addition to the experimental characterization, DFT simulations also showed a considerable enhancement of the visible light absorption along with increasing defect concentration, which is consistent with the experimental results. As shown schematically in Fig. 3.1, the objective of the present study is to investigate the change in optical properties and surface modification in terms the change in the properties of the nanoparticle core and surface capping layer This study presents a new experimental approach to tailor the optical, electrical and photocatalytic properties of TiO_2 nanoparticle in a controlled manner.

3.2 Results and Discussion

3.2.1 Morphological and structural properties

HRTEM investigations have been carried out in order to investigate the changes in microstructure upon hydrogen treatment and the results are shown in Fig 3.1. The pristine TiO_2 nanocrystals are crystalline as indicated by the well-defined lattice fringes. HRTEM images for black H:TiO_2 nanoparticles hydrogen treated for 30 hours exhibit a disordered amorphous shell around the crystalline TiO_2 core resulting in the formation of core-shell type of a nanostructure. This is shown in Fig. 3.1. The average size of individual nanoparticles is approximately 15 nm in diameter. The disordered layer is about 1-2 nm in thickness around the crystalline core after the hydrogen treatment for

30 hrs. From these values, we can estimate that the fraction of disordered material is between 15-25% of the total volume. The presence of amorphous TiO_2 shell around the nanoparticles is expected to have a large effect on the surface catalytic properties and change in the crystalline TiO_2 core on the optical and band structure. Blue shifts and broadening of the Raman peaks in argon treated TiO_2 are related to non-stochiometry and structural defects[151]. Hydrogen implantation of Anatase TiO_2, single crystal surfaces and TiO_2 nanotubes have shown enhanced photocatalytic properties[162]. The presence of Ti^{3+} defects, surface hydroxyl groups, oxygen vacancies, and Ti-H bonds show large change in optical properties resulting in increased optical absorption and in electronic and catalytic properties[163]. Physical, chemical properties and surface adsorption been related to disordered crystalline structure and large changes in the photo-catalytic properties been observed in amorphous TiO_2 nanostructures[164]. These will be discussed later in detail. The optical image of pristine and hydrogen treated samples show the change in the color on hydrogen treatment and the formation of black-like TiO_2 nanoparticles indicating a large change in the optical properties indicating higher visible light absorption.

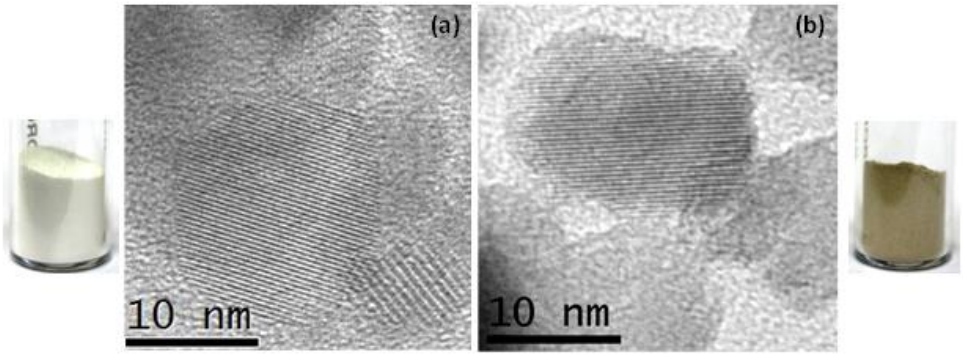

Figure 3.1: HR-TEM images of a) pristine and b) vacuum hydrogen treated TiO_2 nanoparticle sample for 30 hrs. Optical image of the two samples are also shown.

X-ray diffraction (XRD) spectra for the pristine and TiO_2 nanocrystals samples hydrogen annealed for 30 hours at 300^oC were taken and the results are shown in

Fig.3.2. The XRD peaks have been indexed for both of pristine and H:TiO_2 samples and the results show that the peaks correspond to the tetragonal anatase TiO_2 crystallographic phase. Major peaks are observed at 2θ angles of 25.3, 37.84, 48.07, 53.95, and 55.10 ^{o} which correspond to d-values of 3.51, 2.37, 1.89, 1.69, and 1.66Å and (hkl) values of(101), (044), (200), (105) and (211), respectively. These results indicate that tetragonal structure and anatase phase of TiO_2 is retained even after hydrogen annealing at 300^{o}C for 30 hours in vacuum conditions. It is thus clear that any change in the properties of white TiO_2 to black TiO_2 is not due to any major structural changes or phase transformation. The annealing of TiO_2 in hydrogen ambient seems to affect TiO_2 in other possible ways and not major phase transformation. From the results reported in the literature, it is expected that hydrogenation process can lead to the formation of TiH_2 or formation of lattice defects[160]. Slight decrease in the intensity of the XRD diffraction peak especially for (101) peak in H:TiO_2 indicates that the crystallinity of H:TiO_2 upon hydrogen treatment is decreased due to defect generation or some degree of surface disorder.

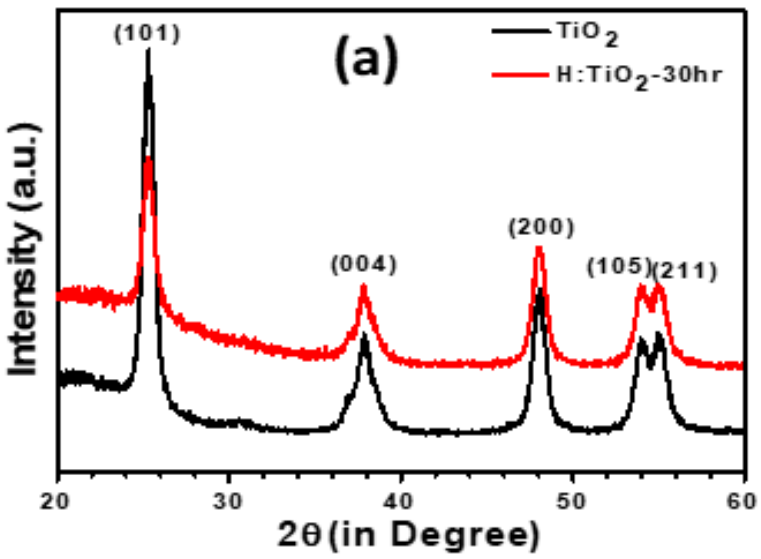

Figure 3.2: XRD spectra of the pristine and vacuum hydrogen treated TiO_2 *nanoparticle sample.*

In comparison to XRD technique, Raman spectroscopy is relatively more sensitive to small changes in stoichiometry. Raman spectroscopy was carried out on pristine and H:TiO_2 and results are shown in Fig. 3.3. Well-resolved TiO_2 Raman peaks were observed at 144 cm^{-1} (B_{1g}), 398 cm^{-1} (B_{1g}), 515 cm^{-1} (E_g), and 640 cm^{-1} (E_g) in the spectra of all samples, indicating that anatase is the predominant phase in both the nanoparticle samples. The decrease in the intensity of the Raman peaks may be due to the formation of defects in the TiO_2 core and the formation of amorphous TiO_2 shell as indicated by HRTEM results. Low intensity of the Raman peak corresponding to Brookite phase in Lanthanum doped TiO_2 nanopowder has been related to highly disordered phase [165]. Only the peak expected at 147 cm^{-1} (E_g) was not visible, which may be suppressed by a much stronger TiO_2 peak at 144 cm^{-1} (B_{1g}) line[166]. No major effects of vacuum hydrogen treatment with time is therefore observed in terms of position of peaks. This indicates that the anatase structure is present even after hydrogen treatment and this result is consistent with the XRD results.

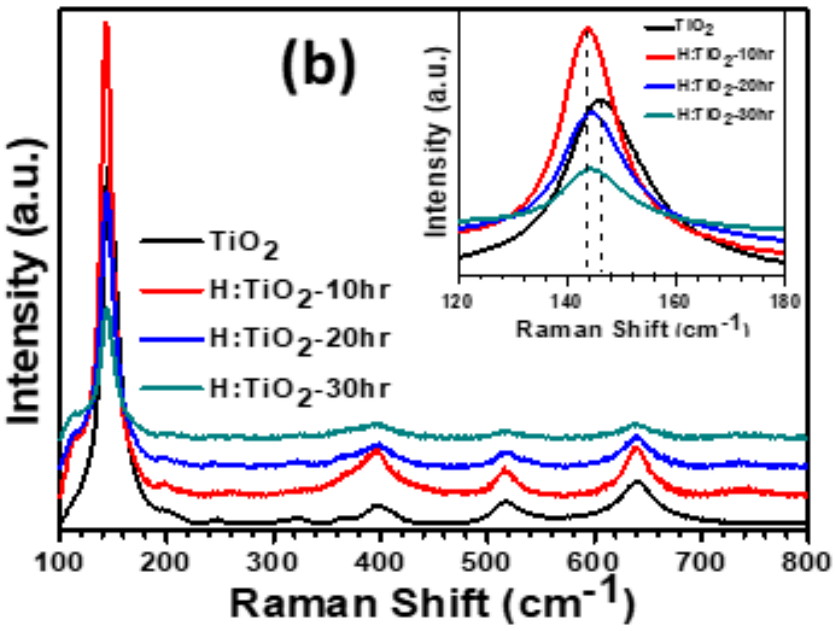

Figure 3.3: Raman spectra of the pristine and vacuum hydrogen treated TiO_2 nanoparticle sample.

3.2.2 Optical Properties

Fig. 3.4 shows the absorbance spectra of pristine and vacuum hydrogen treated TiO_2 nanocrystals. The observed decrease in absorbance at wavelengths longer than 375 nm is due to the intrinsic band gap of crystalline anatase TiO_2. At wavelength lower than this, a strong absorption is observed due to bandgap excitations.H:TiO_2 samples with different durations of treatment show a significant shift of absorption edge towards higher wavelength indicating visible light absorption. For TiO_2 sample treated in hydrogen for 30 hrs, higher absorbance is observed in the wavelength range 375-675 nm. The calculated values of band gap energy of the pristine TiO_2 nanocrystals is approximately 3.30 eV, slightly higher than that of bulk anatase TiO_2. The onset of light absorption for the vacuum hydrogen treated black TiO_2 nanocrystals is lowered to about 2.59 eV. This is consistent with the change in the color of the nanoparticle samples as shown in the optical images in Fig 3.1.

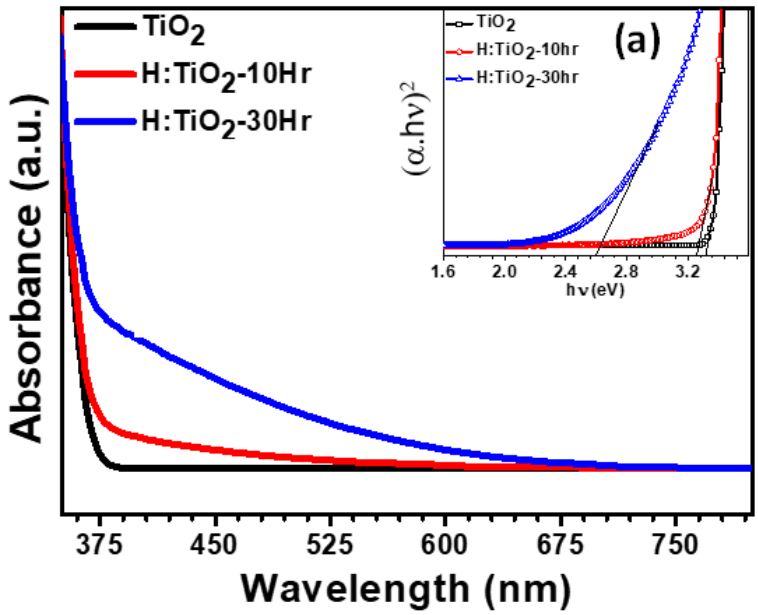

Figure 3.4: Absorbance spectra of pristine and vacuum hydrogen treated TiO_2 nanoparticle sample. Insert shows the Tauc's plot giving the value of absorption edge of the samples.

Fourier transform infrared (FTIR) spectroscopic measurements were carried out to characterize both the samples and the results are shown in Fig.3.5. FTIR spectra for both pristine and vacuum hydrogen treated samples show similar absorption features from 500 cm^{-1} to 4000 cm^{-1} along with the absorption bands near the 1635 cm^{-1} and 3400 cm^{-1} regions. The characteristic feature of the spectrum symmetric stretching vibrations of the Ti–O bonds is observed in the spectral region 400-800 cm^{-1} which is probably due to the TiO_6 octahedra. On vacuum hydrogen treatment, the intensity of OH absorption bands at 3400 cm^{-1} decreases slightly and a wider OH absorption band is observed in comparison to pristine TiO_2 due to defect formation[167].

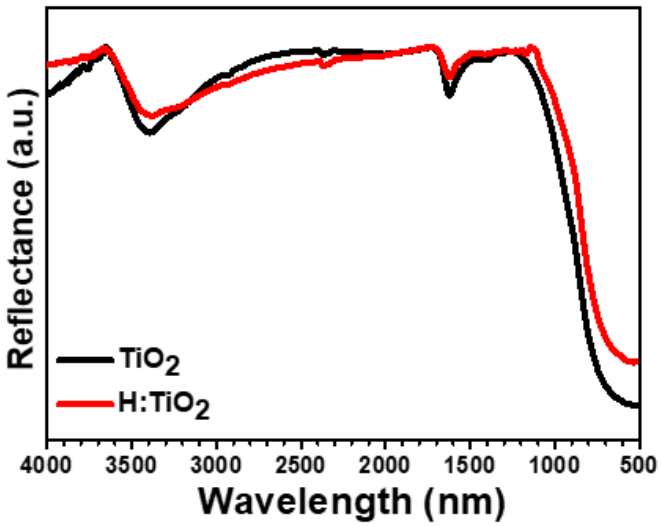

Figure 3.5: FTIR spectra of the pristine and vacuum hydrogen treated TiO_2 nanoparticle sample.

3.2.3 NMR and EPR investigations

EPR and NMR studies were carried out on pristine and hydrogenation TiO_2 nanoparticles samples. Proton Nuclear magnetic resonance (^{1}H-NMR) measurements have been carried out by using Nuclear Magnetic Resonance Spectrometer (JEOL-JNM-ECA Series (Delta V4.3)-400 MHz-FT-NMR). The EPR studies were carried out using a Bruker EPR 100d X-band spectrometer for pristine and H:TiO_2 samples through the EPR cavity. *G* values were calibrated using a di(phenyl)-(2,4,6-trinitrophenyl

iminoazanium (DPPH) sample. The center field value of 3512 G, frequency 9.74 GHz and microwave power of 20 mW was utilized in EPR measurements.

^{1}H NMR measurements have been carried out to study the role of hydrogen incorporation on TiO_2 nanoparticles in vacuum conditions. Fig. 3.6 shows the ^{1}H NMR data of pristine and H:TiO_2 samples with peaks corresponding to the chemical shift at 3.74 and 3.87 ppm, respectively. Pristine TiO_2 shows two narrow peaks at chemical shifts of +0.22 ppm and -0.77 ppm. However, the hydrogen treated H:TiO_2 sample shows a pronounced additional peak at a chemical shift of -1.07 ppm. This new peak at δ = -1.07 ppm in H:TiO_2 is due to the presence of weakly bound hydrogen atoms at bridging sites at the surface formed during the vacuum hydrogen treatment process on the surface[168,169]. It can be concluded that the weakly bounded hydrogen atoms are absorbed by oxygen vacancies on hydrogen treatment[170-173]. These results may explain the formation of black TiO_2. As already explained the presence of defects and surface functional groups have been related with the formation of defect states in the forbidden gap of TiO_2. Absorption of photons of lower energy due to the defect states is considered to be responsible for conversion of white TiO_2 to black TiO_2[162].

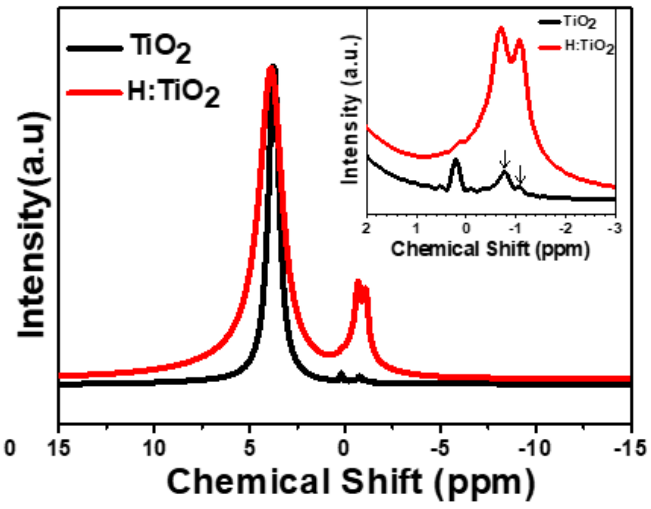

Figure 3.6: ^{1}H NMR spectra of pristine and vacuum hydrogen treated TiO_2 samples recorded at 300 K.

Electron paramagnetic resonance (EPR) spectroscopy is a technique to study the presence of unpaired electrons and therefore, is a useful technique to study the change in the properties on defect formation or changes in the defect configurations. As shown in Fig.3.7, the pristine TiO_2 samples contain only Ti^{4+} ($3d^0$) ions and show signal due to weak unpaired electrons. For the sample treated with hydrogen for 30 hrs, a strong EPR signal was observed with the g value of 2.0822, which is characteristic parameter corresponding to paramagnetic Ti^{3+} centers. The formation of Ti^{3+} centers can be explained due to the generation of oxygen vacancies during the reduction of TiO_2 during hydrogen treatment. It has been proposed in a number of experimental and theoretical[170-172] works that atomic hydrogen gets preferably absorbed at the oxygen vacancies in TiO_2[173]. The strong EPR signal in $H:TiO_2$ is indicative of a large concentration of Ti^{3+} and oxygen vacancies in hydrogen treated sample.

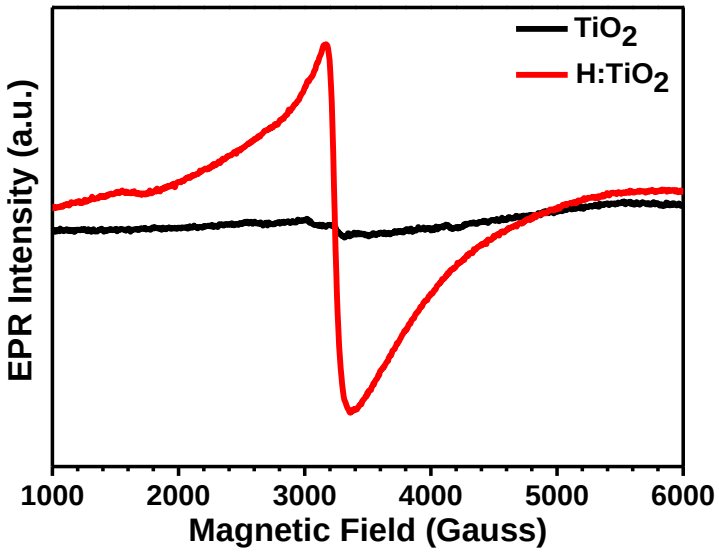

Figure 3.7: EPR spectra of pristine and vacuum hydrogen treated TiO_2 samples recorded at 300 K.

3.2.4 Photocatalytic and photo-electrochemical activity

In addition to the optical properties, the modification in the surface catalytic properties on hydrogenation is also important for photo-electrochemical applications. The

photocatalytic activity of pristine and hydrogen treated samples was studied by measuring the degradation of methylene blue (MB) under visible-light exposure as a function of time and the results are shown in Fig 3.8. It is shown that the pristine TiO_2 sample shows a lower photocatalytic activity in the visible-light and the degradation rate constant k of pristine TiO_2 was found to be 5.1×10^{-6} min^{-1}. This small value can be due to the lower light absorption, especially in the visible part of the spectrum. For the H:TiO_2 samples, the photodegradation activity increases with increasing the hydrogen treatment which may be due to both, the enhanced visible light absorption and increase in surface catalytic properties on hydrogen treatment. The photodegradation rate constant k reaches the maximumvalue of ~9.9×10^{-3} min^{-1} for the 30 hrs hydrogen treated sample. This value is approximately three orders higher than that of pristine TiO_2 under visible-light irradiation and confirms, a large modification in the optical absorption properties on hydrogenation as indicated by optical absorption studies. It also shows modification in the surface catalytic properties due to defect formation as was indicated in EPR and NMR studies.

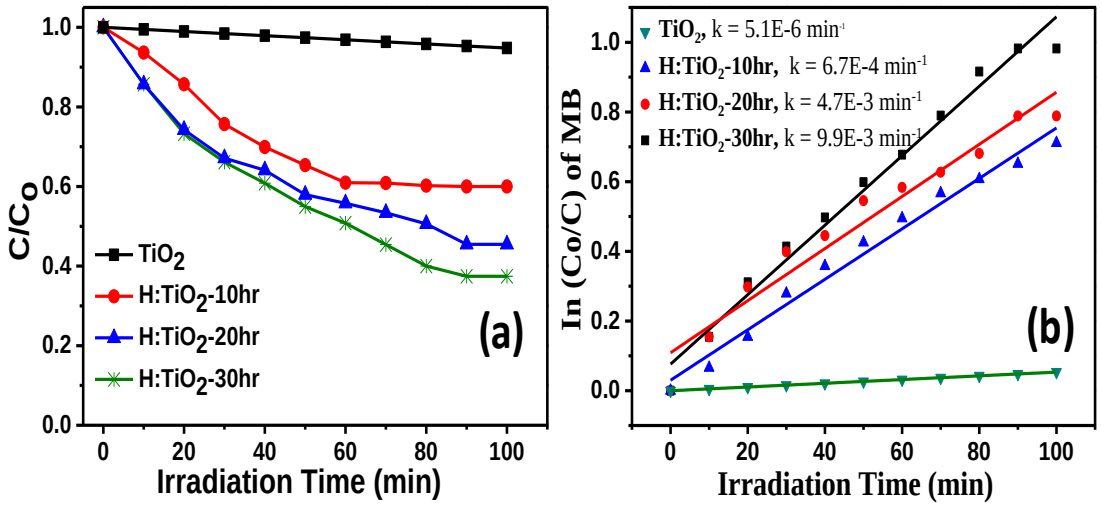

Figure 3.8: a) Solar-light driven photocatalytic decomposition of methylene blue and b) rate constant calculation for pristine and vacuum hydrogen treated TiO_2 samples.

It is important to discuss the effect of change in the various properties of TiO_2 nanoparticle due to hydrogenation process discussed above on the photo-electrochemical activity. TiO_2 and H: TiO_2 powders were prepared and deposited in the form of thin layers on ITO substrates using the spin coating technique. This was essential to form photoelectrodes based on pristine and hydrogenation nanoparticle samples for performing photo-electrochemical measurements. As discussed in experimental section, the measurements were performed under visible light illumination with output intensity 100 mW/cm^2 using a tungsten lamp source. The PEC properties of H:TiO_2 were investigated by measuring the current under dark and illumination conditions in the potential range +0.5 to +1.0 V *vs.* Ag/AgCl with a scan rate of 20 mV/s. Fig.3.9 shows the photocurrent density vs. applied potential (V *vs.* Ag/AgCl) for pristine and vacuum hydrogen treated TiO_2 samples collected in 1M NaOH solution. In case of pristine TiO_2, a very small value of the photocurrent of~35µA/cm^2 (at 1.0 V *vs.* Ag/AgCl) was observed. In comparison to this, H:TiO_2 layer sample shows a relatively large value of photocurrent density ~0.56 mA/cm^2(at 1.0 V *vs.* Ag/AgCl).

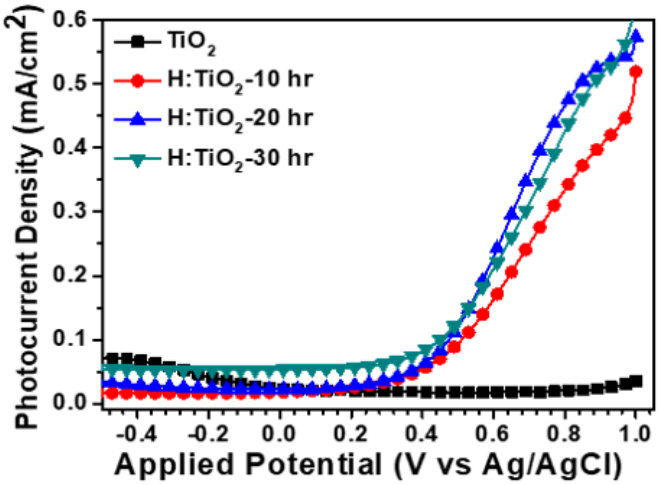

Figure 3.9: Photocurrent density vs. applied potential (V vs. Ag/AgCl) curves showing photo-electrochemical response

3.2.5 Junction and interface properties

To study the electron transport and interface properties of TiO_2 samples corresponding to sample-electrolyte interface, TiO_2 layers were used as working electrodes and C-V measurements were carried outat 1kHz ac signal frequency in 1M NaOH solution under dark conditions. Mott-Schottky ($1/C^2$ versus V) plotsobtained from these results are shown in Fig 3.10. The donor density (N_D) and flat band potential (V_{FB}) corresponding to the semiconductor-electrolyte interface was obtained using the Mott-Schottky relation. Fig.3.10 shows the Mott-Schottky plots for pristine and vacuum hydrogen treated TiO_2 samples. The positive slope of Mott-Schottky curves in both the samples indicate n- type conduction in TiO_2 films. The donor density was estimated from the slopes of the Mott-Schottky curve using the equation. The calculated value of $N_{D,}$ from the slopes of the curve, was found to increase in hydrogenated sample. The vacuum hydrogen treated H:TiO_2 films exhibited significantly higher donor density, 5.5×10^{17} cm^{-3} compared to the pristine TiO_2 (7.2×10^{16} cm^{-3}) sample. This change in the electronic properties at the surface of TiO_2 on hydrogenation is important as no change in crystal structure or any major change in the stoichiometry was observed. The enhanced donor density can be attributed to excess electrons provided by lattice defects such as oxygen vacancies (V_O) or oxygen vacancies that are occupied by atomic hydrogen (H_O). The observed negative shift of flat band potential could be due to the substantially increased electron density, which is expected to shift the Fermi level of TiO_2 towards the conduction band. As was mentioned in chapter 2, the values of donor density and flat band potential obtained from these plots is sensitive to the nature of the interface and the presence of surface or oxide layers can alter these values. But the large change in the properties in pristine and hydrogenated samples does indicate the effect of hydrogenation process on electronic properties and electron transfer process at the interface.

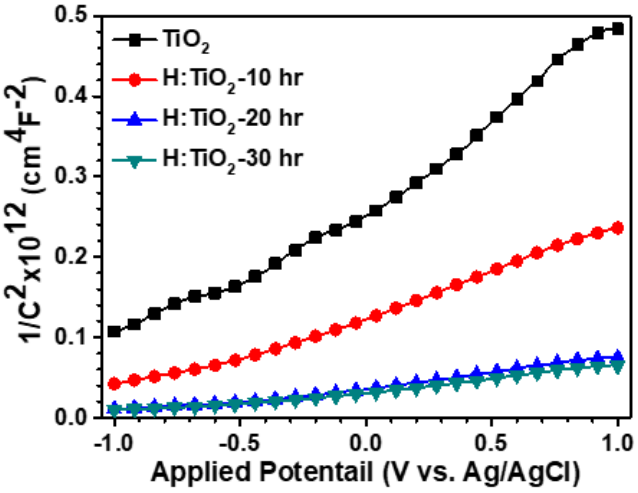

Figure 3.10: Mott-Schottky plots for pristine and vacuum hydrogen treated TiO_2 samples collected in 1M NaOH solution.

It is important to understand the effect of hydrogen treatment on the charge separation and recombination processes at the interface, as these processes are important in determining the PEC response, in addition to optical absorption and surface catalytic properties. For this purpose, electrochemical impedance spectroscopic (EIS) measurements were carried out. EIS Nyquist plots of the pristine and H:TiO_2 samples are shown in Fig.3.11. The semicircle plot can be fitted as per the Randles equivalent circuit model[174] (inset of Fig. 3.11). In this model, the R_S is the resistance related to the resistance of the semiconductor catalyst, ITO substrate, the electrolyte and wire connections in the whole circuit. The elements of $R_{ct,bulk}$ and C_{bulk} are related to the charge transfer at the interface of the photoelectrode/electrolyte. A smaller radius of semicircle represents a better charge transfer ability (i.e., faster surface reaction kinetics)[174]. Radius of semicircle in case of H:TiO_2 sample is quite lower than for pristine and other TiO_2 samples, which indicates that the hydrogen treatment of TiO_2 reduces the semiconductor-electrolyte resistance and enhances the charge transport. The improved charge transport in case of H:TiO_2 samples is expected to direclty improve PEC activity at the oxide-electrolyte interface. The smaller radiusin case of

H:TiO_2 sample is presumably due to an increased electron density as obtained in the Mott-Schottky measurement which improves the electrical conductivity of the electrodes resulting in fast charge transfer occurs on the photoelectrode after hydrogenation.

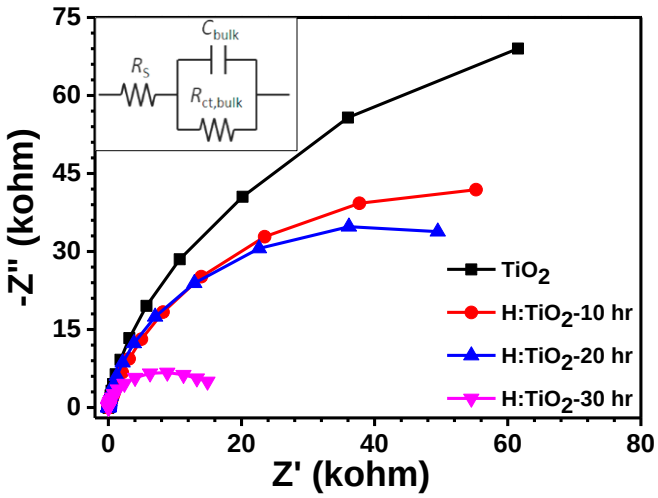

Figure 3.11: EIS Nyquist plots of the pristine and vacuum hydrogen treated TiO_2 samples at an open bias condition under dark.

3.2.6 Density Function Theory Simulations

Density function theory simulation was carried out to study the formation of defects in TiO_2 on hydrogenation and its effect on the band structure and optical and electronic properties. For the *ab initio* calculations the Vienna *ab initio* simulations package (VASP) was used[175]. In VASP the valence electrons are described by using a plane wave basis set and the core electrons are taken into account using the projector-augmented wave formalism. All simulations were carried out within the PBE + *U* framework. A value of 4 eV was used for the Hubbard parameter *U* very close to the choice used in previous studies on n-type defects in TiO_2[176]. For modelling hydrogen treated anatase TiO_2 with different levels of disorder, a 3 × 3 × 1 super cell was used. Structural relaxations were performed until all forces were smaller than 0.02 eV $Å^{-1}$. The unit cell vectors were optimized simultaneously with the ion positions until

pressure lower than 1.0 kbar (0.1 GPa) was reached. In those cases where external pressure was applied, the unit cell vectors were varied until the target pressure was reached with an accuracy of 1.0 kbar. The details related to the calculation of absorption coefficient and imaginary part of the dielectric function are described in detail elsewhere[177].

As a first step, it is important to understand which defects are energetically favorable under different conditions. The energetics of both, localized and delocalized states induced by the various defects, V_O or H_O, as a function of defect concentration and external pressure were evaluated. In the present study, simulations were carried out using PBE+U approach. An anatase supercells of the composition $Ti_{36}O_{72}$ was generated by a 3×3×1 repetition of the tetragonal anatase unit cell. The dimensions of the optimized defect free supercell are 1.17×1.17×0.97 nm^3. Different supercell configurations $Ti_{36}O_{72-x}$ (V_O defects) and $Ti_{36}O_{72-x}H_x$ (H_O defects) at different values of x = 0,1,6,10 was considered corresponding to defect concentrations of 0, 1.4, 8.3 and 13.9% with respect to the number of oxygen atoms. Disorder in the material was modelled by placing the lattice defects on random sites in the super cell. However, the positions of the impurities were chosen such that defects on adjacent sites were avoided since such configurations are energetically disfavored.

The results obtained from the ab-initio calculations indicate the conditions which favor the generation of localized Ti^{3+} centers or delocalized shallow donor states due to V_O and H_O defects. The stabilty of the localized Ti^{3+} states is studied by calculating the localization energy (given by the following equation) as a function of the concentrations of V_O and H_O defects and external pressure. In the equation 3.1, E_{deloc} and E_{loc} are the ground state energies of the defective TiO_2 unit cells with delocalized and localized Ti^{3+} states, respectively.

$$E_{\mathrm{loc}} = \frac{E_{\mathrm{deloc}} - E_{\mathrm{loc}}}{d} \qquad \ldots\ldots\ldots\

In the next step, modification in the electronic structure of TiO_2 as a function of the concentration of V_O and H_O defects is investigated. The presence of localized Ti^{3+} centers can be associated with the formation of occupied mid-gap states in the density of states (DOS). As shown in Fig. 3.12, at low concentrations of oxygen vacancies (1%), two types of mid-gap states at 0.74 eV and 1.11 eV, below the conduction band minimum (CBM) are observed. These are formed by two localized Ti^{3+}centers in the vicinity of the respective oxygen vacancies. At the lowest considered concentration of H_O defects, as the delocalized solution is favored such that no mid gap state is present in the DOS. At higher defect concentrations occupied mid gap states are present for both defect types and the respective mid gap state spectra broaden and shift down towards the valence band maximum, although the broadening of the spectrum is considerably more pronounced for the V_O defects. It may be mentioned that in the present calculations, the electronic band gap of pristine $TiO_2$is 2.55 eV, which is due to know underestimation in DFT calculations.

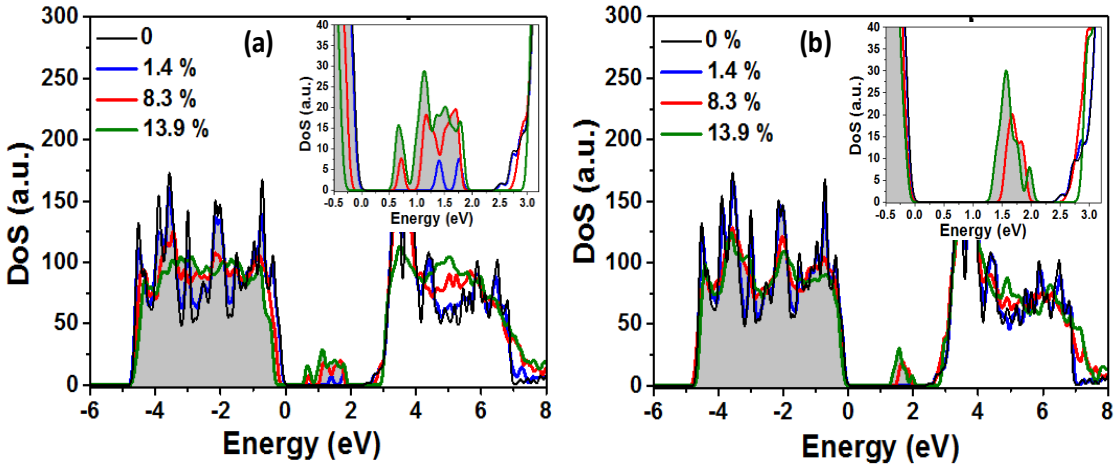

Figure 3.13: Density of states of anatase TiO_2 for different concentrations of oxygen vacancies V_O in a) and substitutional H_O defects in b). The band gap areas are enlarged and shown as insets. Shown are the densities of states for 0, 1, 6 and 10 defects in the 3×3×1 supercell. The highest occupied state of pristine TiO_2 is taken as zero energy. Occupied energy levels are indicated by the grey colour.

The most important results in the context of the present study is: how do the concentration of V_O and H_O defects influence the optical absorption below the absorption edge of pristine TiO_2. Therefore, it is important to determine the optical absorption properties in the presence of defect. In Fig.3.13, optical absorption coefficient for the V_O defects is shown. At the low defect concentration of 1.4%, the absorption of photons with energies below the band gap energy of pristine TiO_2 is observed. With increasing defect concentration, the absorption increases further and up to the investigated defect concentration of 13.9%, an increase in absorption with increase in concentration is observed. This indicates that the magnitude of disorder is important in determining the optical properties. It can therefore be conjectured that the increase in optical absorbance with increase in hydrogenation time is consistent with the above results of increasing absorption with increase in defect concentration. It may be noted that the simulated values are red-shifted with respect to the experimental data due to the underestimation of the electronic band gap. The absorption coefficient spectrum for different H_O defect concentrations are also shown in Fig. 3.14. Not much absorption in the band gap region of pristine TiO_2 is observed at the low defect concentration of 1.4 %, which is in accordance with the absence of a localized midgap state. At higher defect concentrations absorption in the visible part of the spectrum sets in and also an increasing defect concentration leading to higher absorption coefficient is observed. In contrast to this, the experimental data for the absorption coefficient decays much slower with increasing wavelength. This suggests that the vacuum hydrogen treated samples considered in this work mainly contain oxygen vacancies which do not exclude their partial occupancy by substitutional hydrogen.

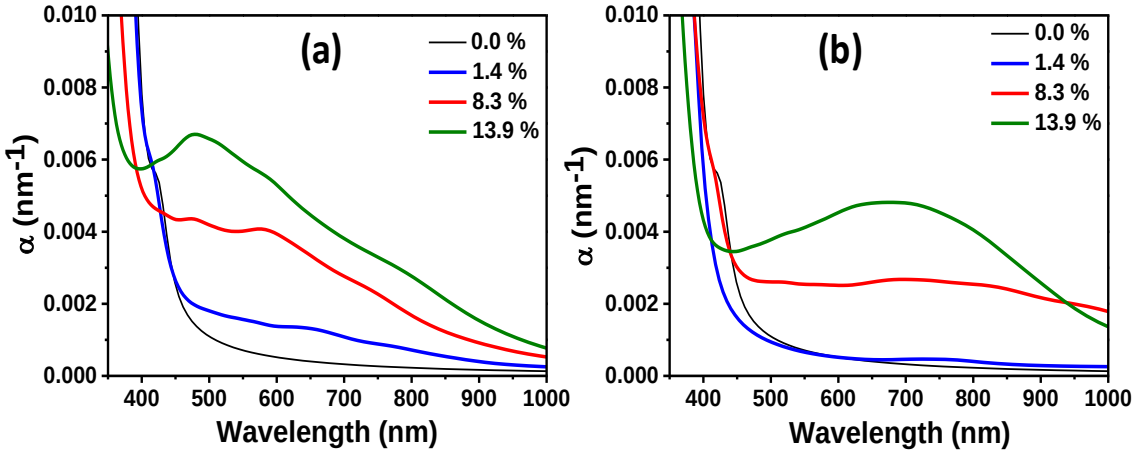

Figure 3.14: Absorption coefficient of TiO_2 with different concentrations of oxygen vacancies in a) pristine TiO_2 and b) H:TiO_2.

It is concluded that oxygen vacancies are occupied by atomic hydrogen leading to the conversion of stoichiometric TiO_2 to the composition $TiO_{2-x}H_x$. This finding was rationalized by the absence of any localized Ti^{3+} centers in the EPR results,which are typically formed near oxygen vacancies. This reasoning is supported by simulations and the observation of a strong EPR signal of localized Ti^{3+} states. As the samples were synthesized under rather mild hydrogen conditions, it can be concluded that the majority of oxygen vacancies are not occupied by atomic hydrogen. Previous experimental studies[172-174] and our simulation results show that a high concentration of oxygen vacancies and Ti^{3+} centers introduces occupied mid-gap states, which substantially narrow the electronic band gap of TiO_2. Photoexcitation of these states correspondingly leads to a narrow optical band gap in agreement with optical measurements.

It is important to understand the crucial role of vacuum hydrogen treatment to form localized electronic mid gap states in the form of Ti^{3+} centers as experimentally observed in this work. In different studies oxygen vacancies (pristine V_O or occupied by atomic hydrogen H_O) have been considered as the main defects associated with the reduction of TiO_2 by hydrogen and the resulting modification of the electronic structure

and optical absorption properties. In many cases[178,179], the blackening of hydrogen treated TiO_2 is related to the formation of localized Ti^{3+} states in the TiO_2 band gap enabling the absorption of photons from the visible light spectrum. However, hydrogen treatment of TiO_2 can also lead to the generation of a high density of occupied delocalized electronic states which act as shallow electron donors and hence lead to a high concentration of mobile charge carriers[173].

The significant improvement in the photocatalytic activity and photocurrent density after vacuum hydrogen annealing of TiO_2 nanocrystals shows that it can generate more electron-hole pairs in visible light and exhibits a stronger ability for electron-hole pair separation than pristine TiO_2. The observation of a small photocurrent in pristine TiO_2 using visible light illumination (λ>380 nm) is due to the high band gap energy as the photons with energies less than the band gap energy (E_g = 3.31 eV) did not contribute to the excitation of valence band electrons to the conduction band to generate the electron-hole pairs. The DRS, EPR and Mott-Schottky measurements and DFT calculation clearly show that the reduction in band gap of H:TiO_2 is likely due to the formation of midgap states induced by localized Ti^{3+} states. Therefore, the significant improvement in photocatalytic activity and photocurrent density can be explained by the surface disordering and defects formation after vacuum hydrogen annealing.

3.3 Conclusions

In summary, it has been shown that vacuum hydrogen treatment of TiO_2 under mild hydrogen condition at lower pressures than atmospheric pressure, at 2.0* 10^{-3} Torr. leads to an enhanced photocatalytic and photo-electrochemical response, which significantly depends on the duration of hydrogen treatment. DRS and EPR analysis of pristine and vacuum hydrogen treated TiO_2 nanocrystals show that the tailoring in properties of H:TiO_2 is due to surface oxygen-vacancies and Ti^{3+} states. Additionally,

these modifications in properties induced a higher charge carrier concentration and a more negative flat band potential as compared to pristine TiO_2. The experimental studies were substantiated by *ab-initio* calculations in order to gain a deeper understanding of the origin of enhanced visible light absorption due to Ti^{3+} centers and the conditions that favor the formation of localized or delocalized excess electrons due to oxygen vacancies. Carriers captured by localized states do not participate in conduction process. Therefore, conditions which create delocalized states are important for improved electronic behaviour in addition to increased optical absorption[19,20]. It was shown that with higher concentrations of V_O and H_O defects the spectrum of the induced mid gap states broaden considerably and moves energetically downward towards the VBM. At the same time the visible light absorption increases and localization of the Ti^{3+} states becomes more favorable. Substitutional H_O defects at low concentrations were identified as candidates to provide delocalized charge carriers in TiO_2. This study provides a detailed overall picture covering experimental and theoretical aspects of the effect of hydrogen treatment on the structural, optical and electronic properties of the TiO_2 matrix and resulting improvements in the photo-electrochemical properties. One of the important finding of the present study is the identification of Ti 3+ defects responsible for change in optical and structural properties on hydrogen treatment under vacuum conditions. The enhancement in surface catalytic and photo-electro-chemical properties on hydrogen treatment under clean vacuum conditions can be utilized for large scale application.

Chapter 4

TiO_2 nanoparticles: MoS_2 nanoflake composite

4.1 Introduction

In this chapter, composite nanostructures comprising of MoS_2 2D nanoflakes and TiO_2 nanoparticles (TiO_2-MoS_2 nanocomposite) with varying concentration (2.5 to 10.0 wt. %) have been investigated in terms of structural, optical, photocatalytic and photo-electrochemical properties in comparison to those of pristine TiO_2 nanoparticles. Large surface area of nanoparticles and large interface between 2D flakes and nanoparticles, along with useful optical properties of MoS_2 and photocatalytic and photo-electrochemical properties of TiO_2 are expected to result in potential advantage in terms of efficient light absorption and carrier separation.

4.2 Results and Discussion

4.2.1 Structural and morphological properties

XRD technique was used to study the phase and crystal structure of the TiO_2 and composite nanoparticles for the purpose of investigating if there is any change in the crystal structure on nanocomposite formation. Fig. 4.1 shows the XRD patterns of pristine TiO_2 nanoparticles and 5.0 wt. % MoS_2 in TiO_2 nanocomposite sample. As shown in Fig. 4.1, pristine TiO_2 nanoparticles comprise of pure Anatase phase of TiO_2. This may be due to the annealing of TiO_2 samples at 400^{o}C in an air atmosphere, which is a suitable temperature for Anatase phase formation as discussed earlier in chapter 1 section 1.6.1. In the XRD spectra of MoS_2-TiO_2 nanocomposite, at MoS_2 concentration (< 5.0 wt. %)[137], a single Anatase phase corresponding to TiO_2 nanoparticles was observed[180]. Crystallite size of pristine TiO_2 and MoS_2-TiO_2 nanocomposite has been calculated by using FWHM (full width and half maximum) of TiO_2 peaks and Debye–

Scherrer equation and was found to be 20 nm for pristine TiO_2 and slightly lower (16.6 nm) in 5wt.% MoS_2-TiO_2 nanocomposite. As Scherrer method[139] give an approximate value of crystallite size, it can be interpreted that there is no change in crystallite size on nanocomposite formation. Due to lower concentration of MoS_2, XRD peaks having quite low intensity are observed in comparison to peaks corresponding to major TiO_2 phase.

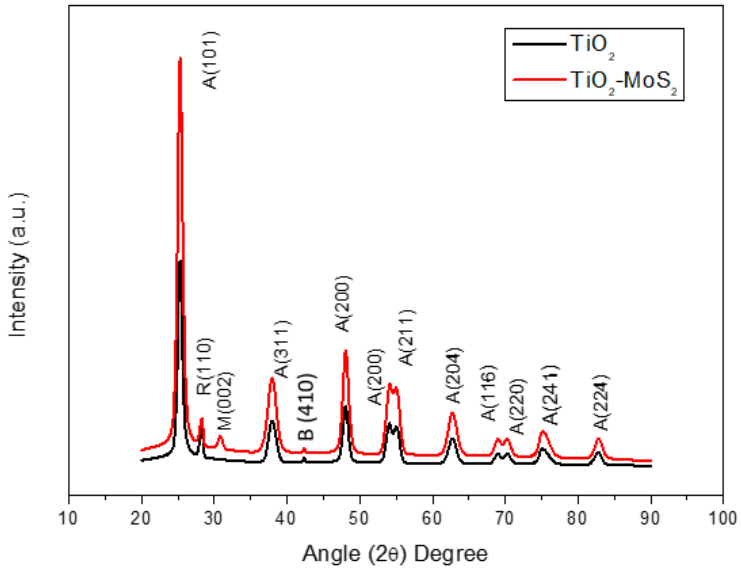

Figure 4.1: XRD spectra of a) TiO_2 and b) 5.0 % MoS_2-TiO_2 nanocomposite sample. XRD peaks indexed as A, R and M peaks correspond to Anatase, Rhombohedral TiO_2 and Rhombohedral MoS_2 phases.

Raman spectroscopy of the samples was carried out to further study the phase and composition on nanocomposite formation. Raman spectroscopy was carried out on pristine TiO_2 nanoparticles and 5.0 wt. % MoS_2-TiO_2 nanocomposite. Raman analysis of pristine TiO_2 nanoparticles shows the formation of Anatase phase (Fig. 4.2). Anatase phase of TiO_2 has six Raman active modes ($A_{1g} + 2B_{1g} + 3E_g$) and out of thesesix modes, five modes are allowed[181]. In the pristine TiO_2 sample, Raman active modes were observed at 143.7 cm^{-1} (E_g), 196.1 cm^{-1} (E_g), 396.0 cm^{-1} (B_{1g}), 515.8 cm^{-1} (B_{1g}) and 638.4 cm^{-1} (E_g)[181], as shown in Fig.4.2. As shown in Fig 4.4, Raman spectra of MoS_2-TiO_2 nanocomposite sample exhibits an additional peak of Rhombohedral phase of

MoS_2 as E_{1g} mode[182] was observed at 381 cm^{-1}. Raman analysis confirms the presence of Rhombohedral phase of MoS_2 in MoS_2-TiO_2 nanocomposite sample.

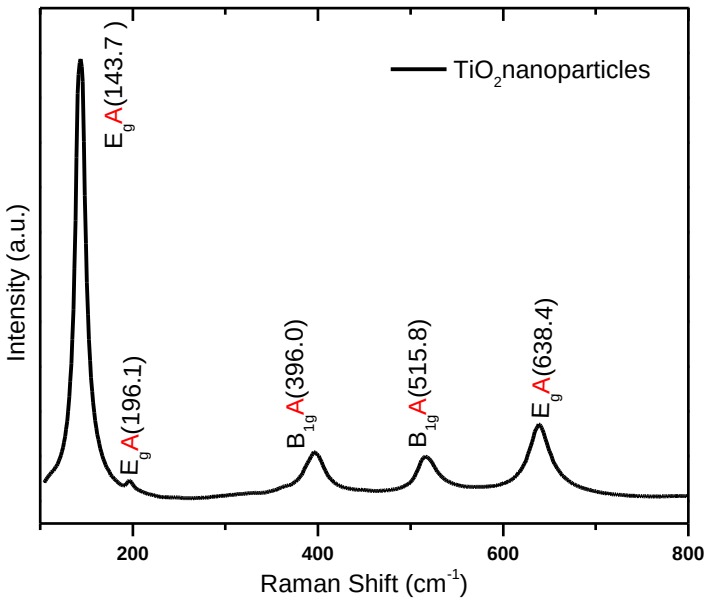

Figure 4.2: Raman Spectra of Pristine TiO_2 nanoparticle sample showing Anatase phase

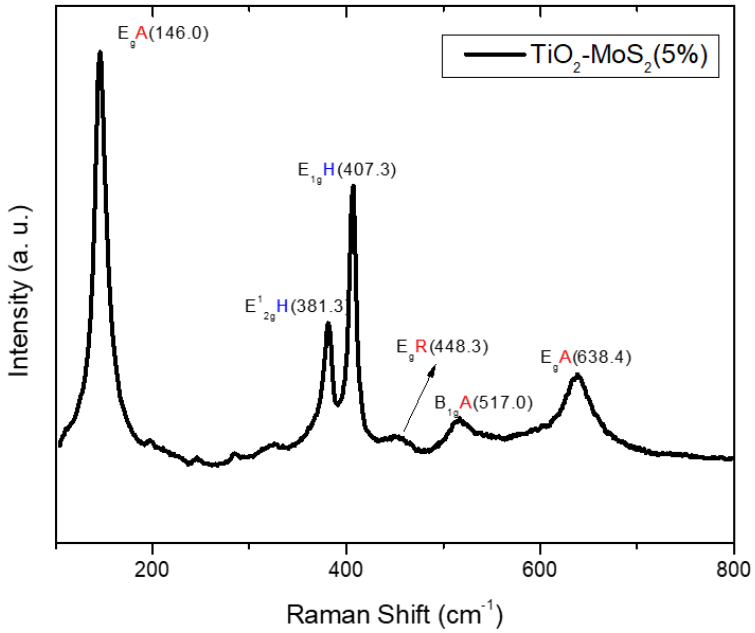

Figure 4.3: Raman spectra of 5.0 % MoS_2-TiO_2 nanocomposite samples

Scanning electron microscopy studies were carried out to study the changes in morphology on nanocomposite formation and the results are shown in Fig. 4.4. It is clearly observed in FESEM image (micrograph a1) that TiO_2 nanoparticles have uniform size and morphology. In case of TiO_2-MoS_2 composites, TiO_2 nanoparticles and MoS_2 nanoflakes are mixed together and there a close morphological proximity within both the phases (image c1).

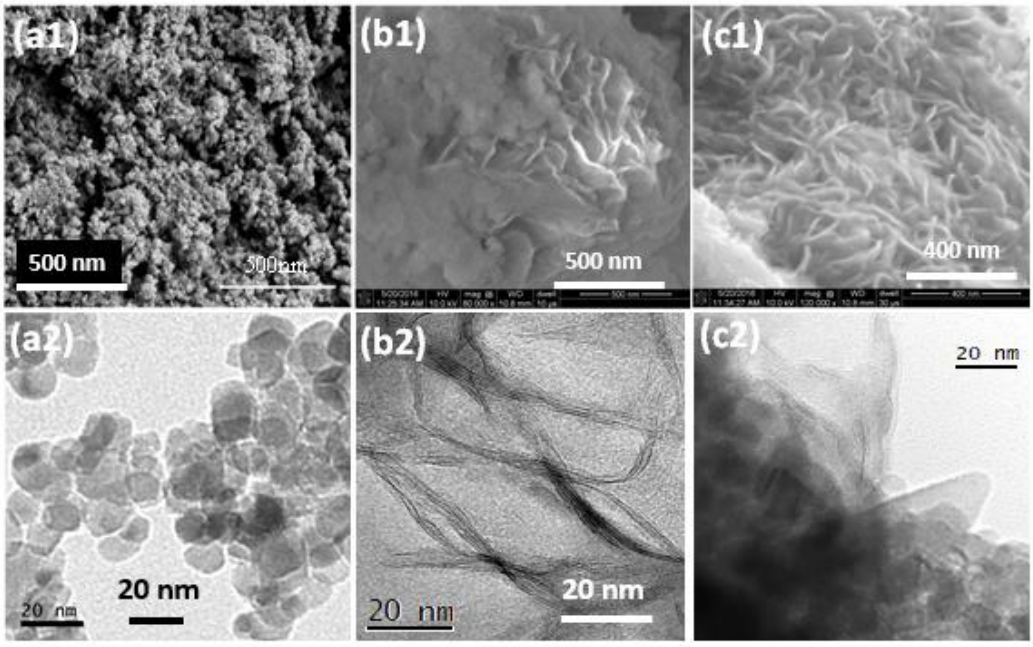

Figure 4.4: SEM microscopic images for structure evolution of (a1) pristine TiO_2 (b1) pure MoS_2 and (c1) 5.0 % MoS_2-TiO_2 nanocomposite sample. TEM images of (a2) pristine TiO_2, (b2) pure MoS_2 and (c2) 5.0 % MoS_2-TiO_2 nanocomposite sample.

The crystallite size in image obtained from FESEM is consistent with that obtained through the XRD spectra. In order to further confirm the composite formation of TiO_2 nanoparticle and MoS_2 nanoflakes, TEM microscopy of the pristine TiO_2, pure MoS_2 and resulting MoS_2-TiO_2nanocomposites are also shown in Fig.4.4. Micrograph b1 shows the SEM image of sample having only MoS_2 flakes. Fig. 4.4 shows the TEM images of pristine TiO_2 nanoparticles (micrograph a2) which indicates the homogeneous morphology in terms of size and shape with an average particle size of

about 10nm. TEM image (micrograph b2) of pure MoS_2 show the nanosheets formation having layered structure. When TiO_2 was incorporated into the MoS_2nanosheets, TiO_2 agglomerates were formed on the surface of the nanosheets. TEM imageof MoS_2-TiO_2 nanocomposite sample (micrograph c2) shows the presence of TiO_2 nanoparticles as well as some nanoflakes like structure of MoS_2. Structural and microscopic investigations show that both MoS_2 and TiO_2 phases are intact in the nanocomposite samples but there is a mixing of the two phases at morphological levels. In other words, both TiO_2 and MoS_2 phases are mixed together which will result in large interfacial area, but both the phases maintain their separate identity in terms of crystal structure and thus properties. Both these observations are useful for the application of nanocomposite samples in PEC applications.

4.2.2 Optical properties

Figure 4.5 shows the absorption spectra of pristine TiO_2 and MoS_2-TiO_2 nanocomposite for 5.0 wt. % and 10 wt. % MoS_2. In case of pristine TiO_2 nanoparticles, only absorption below 380 nm is observed which is attributed to its large band gap of 3.2 eVabsorbs only UV light and exhibits an. As is well known, this results in a very poor absorption of visible light photon and the photo-electrochemical properties of TiO_2 are restricted to only UV light absorption. During the experiment, it was observed that the white coloured TiO_2 nanoparticle sample gets changed to dark-brown colour when the MoS_2 nanoflakes were incorporated along with the TiO_2 nanoparticles in case of nanocomposite sample. These observations indicate that the incorporation of MoS_2 nanoflakes into TiO_2 nanoparticles results in better light absorption in the visible region of the solar spectrum. The absorption intensity at around 450 nm for 10.0 wt. % TiO_2-MoS_2 nanocomposite is obviously enhanced, which is attributed to the visible light absorption characteristics of MoS_2 nanoflakes. The 10.0 wt. % MoS_2 nanoflakes in TiO_2

nanoparticles sample are observed to have absorption bands near 450 nm in the visible region, which are shown in the spectrum of 10.0 wt. % MoS_2 nanoflakes-TiO_2 nanocomposite sample. The above results show that the optical properties of nanocomposite samples can be modified by controlling the concentration of MoS_2 nanoflakes. In addition, the optical absorption edge of MoS_2 nanoflakes can be modified by controlling the thickness or number of layers[183]. Thus, the optical properties of MoS_2 nanoflakes-TiO_2 nanocomposites can be controlled by changing the layer thickness of MoS_2 and the concentration of MoS_2 flakes, which is potentially quite useful for improved photo-electrochemical properties. As these measurements were done by dispersing the nanoparticle samples in liquid medium, the value of absorbance depends upon the amount of sample and its dispersion in the liquid medium. The shift of the absorption edge is independent of the concentration of sample dispersed in liquid medium.

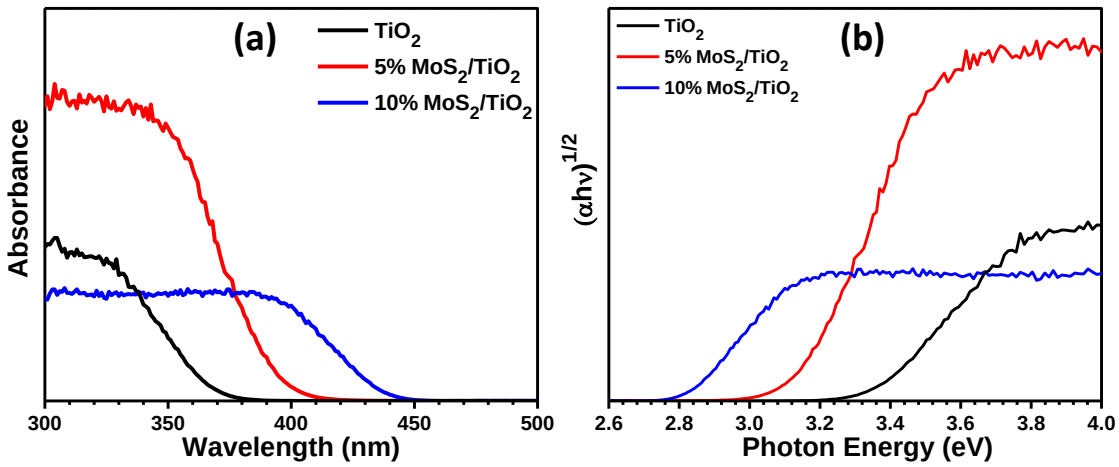

Figure 4.5: Absorption spectra of pristine TiO_2, 5.0 % MoS_2-TiO_2, and 10.0 % MoS_2-TiO_2 nanocomposite sample.

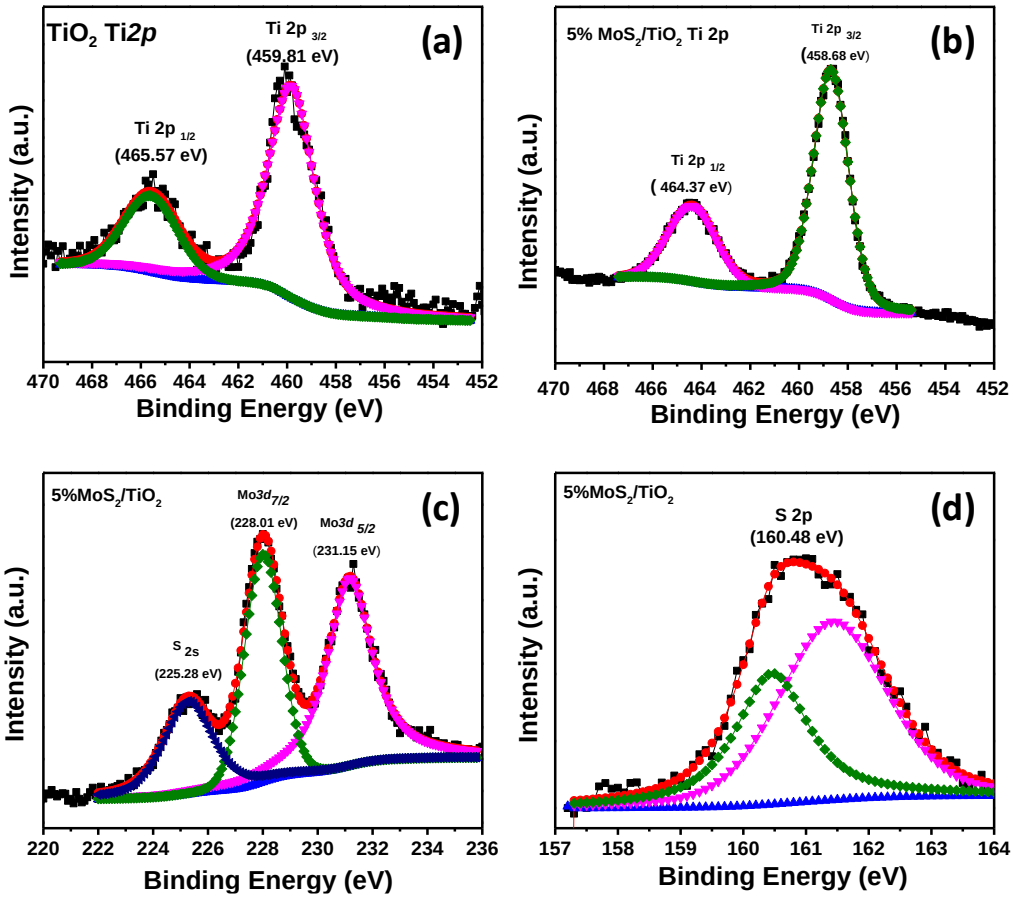

Figure 4.6: XPS spectra of a) Ti 2p in pristine TiO_2 b) Ti 2p in 5.0 % MoS_2-TiO_2, c) O 1s in pristine TiO_2 and d) O 1s in 5.0 % MoS_2-TiO_2 samples.

4.2.3 X-ray photoelectron microscopy studies

XPS measurements on pristine TiO_2 nanoparticles and 5.0 wt. % MoS_2-TiO_2 nanocomposite were carried out and the value of peak positions of various elements were obtained by fitting the Gaussian peaks in the respective XPS spectra. In case of pristine TiO_2 nanoparticles, the position of Ti $2p_{1/2}$ and $Ti2p_{3/2}$ peaks are observed at 465.57 eV and 459.81 eV, respectively. Two peaks of O 1s are observed to be at 529.65 eV and 531.32 eV respectively. The two oxygen peaks are due to oxygen bonded to Ti and oxygen adsorbed on the surface. In the case of 5.0 wt. % MoS_2-TiO_2 nanocomposite sample, Ti $2p_{1/2}$ and Ti $2p_{3/2}$ peaks are observed at 464.37 eV and 458.68 eV, respectively. Whereas, two oxygen peaks are observed to be at 530.06 eV and 530.55

eV respectively. These results show that on addition of MoS_2 nanoflakes on to TiO_2 nanoparticles, Ti2p peaks shifts towards lower energy by 1.20 eV for Ti $2p_{1/2}$ and by 1.13 eV for Ti $2p_{3/2}$.Whereas the value of two oxygen peaks increase and decrease by 0.41 eV and 0.77 eV, respectively. Also, in the case of 5.0 wt. % MoS_2-TiO_2 nanocomposite sample, the position of Mo $3d_{5/2}$ and Mo $3d_{7/2}$ peaks are observed at 231.15 eV and 228.01 eV, respectively (Fig. 4.6) Similarly, the position of S 2p is observed to be at 160.48 eV. The above results indicate an electronic interaction between the two phases resulting in electron transfer and change in the element peak positions.

4.2.4 Photo-catalytic Activity

TiO_2 is known to have good photocatalytic properties. Therefore, it is important to investigate how incorporation of MoS_2 changes these properties. The photocatalytic properties of pristine TiO_2 nanoparticles and MoS_2-TiO_2 nanocomposite samples having different composition (2.5, 5.0, 7.5 and 10.0 wt.%) were determined by studying the degradation of Rhodamine B (RhB) dye in aqueous solution under visible light irradiation. In a typical measurement procedure, 40 mg of photo-catalytic sample was dispersed in 100 mL of 1.0×10^{-5} M RhB aqueous solution. The dye solution with the catalyst was stirred in the dark for 1 hour time until the equilibrium adsorption was attained. No significant decrease in the concentration of the dye was observed after 1 hour for all the experiments. Experiments without simulated solar radiation in the presence of the catalyst, and experiments with simulated solar radiation in the absence of catalyst, showed no degradation of photo-catalytic dye. After centrifugation, a clear supernatant solution was analysed by UV−vis spectrophotometer to determine the concentration of Rh B dye.

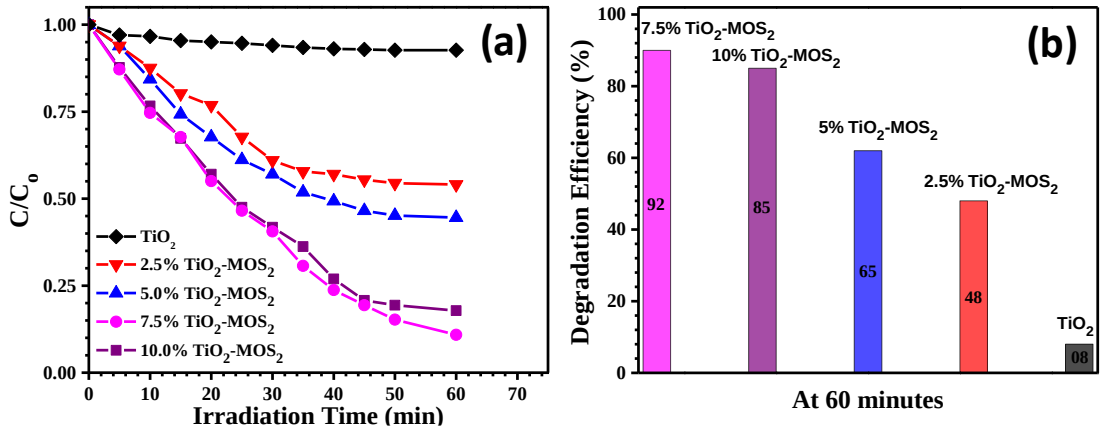

Figure 4.7: a) Photocatalytic performance and b) degradation efficiency of TiO_2, and MoS_2 nanoflakes-TiO_2 nanocomposite sample at various concentration of MoS_2 nanoflakes (by weight) in TiO_2 (2.5, 5.0, 7.5, and 10.0 %) for the degradation of Rh B (rhodamine) dye solution under visible light irradiation.

The degradation of RhB dye was used to evaluate the photo-catalytic properties of pristine TiO_2, MoS_2-TiO_2 having different concentrations, which are shown with respect to irradiation time in Fig. 4.7. The degradation rates increase with increase in the MoS_2 concentration up to a 7.5 wt. % MoS_2 in TiO_2. The degradation efficiency of all the five samples are shown in Fig. 4.7. From the above results, kinetics of photo-degradation of Rh-B dye under visible light was also investigated and is given in Fig. 4.8. Kinetics plot clearly shows a linear relationship between $\ln(C_0/C)$ and reaction time, indicating that the photo-degradation of RhB dye follows the first-order kinetics. The apparent rate constants were determined as 0.0017, 0.0162, and 0.0306min^{-1} for TiO_2, MoS_2-TiO_2 (5.0 %) and MoS_2-TiO_2 (10.0 %), respectively. The order of rate constants is consistent with the conclusions of photo-catalytic degradation curves as shown in Figure 4.8. The result of the above study shows that up to 7.5 % concentration the surface catalytic properties are enhanced. It can be therefore concluded that large surface area of MoS_2 nanoflakes further increases the surface catalytic properties of TiO_2. It is only at a very high concentration (> 7.5% in the present case), MoS_2

nanoflakes seems to screen the TiO_2 nanoparticle surface and thus impede the surface catalytic properties. The above investigation is important from the point of view of the present study. The above results show that at small concentrations, MoS_2 nanoflakes surface and its interface with TiO_2 provide additional sites for photocatalytic reaction, in addition to higher absorption of visible light photons.

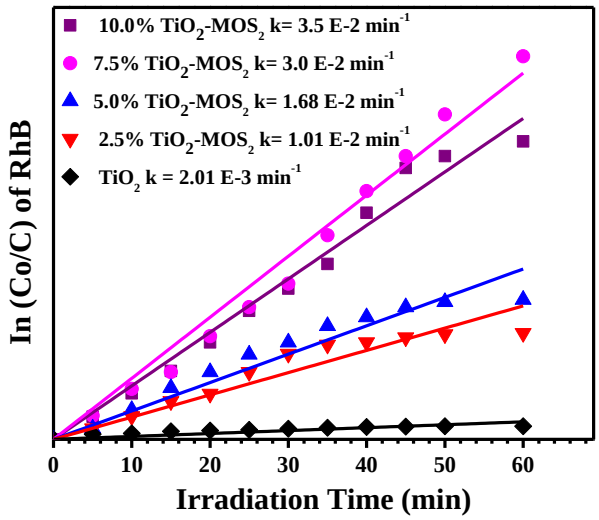

Figure 4.8: Plot of ln(C_0/C) as a function of visible irradiation time for photo-catalysis of Rh B (Rhodamine) dye solution containing: TiO_2, TiO_2-MoS_2 (5.0 %), TiO_2-MoS_2 (7.5 %) and TiO_2-MoS_2 (10.0 %) hetero-structures under visible light irradiation.

4.2.5 Photo-electrochemical properties

The photo-electrochemical performance of the samples were investigated as described earlier in Chapter 2 on experimental studies by forming photoelectrodes from the nanocomposite powder on conducting substrates. The photocurrent response at applied potential in a three-electrode PEC cell with the TiO_2 and TiO_2-MoS_2 nanocomposite photoanodes was investigated. Fig. 4.9 shows the current-voltage characteristics of the pristine TiO_2 and TiO_2-MoS_2 nanocomposite samples having different concentrations of MoS_2 nanoflakes measured under the visible-light conditions. As already mentioned,1M NaOH solution was used as electrolyte. During photo-

electrochemical reaction, the photo-generated holes in the material reaches on the surface of the photoanode and the photo-generated electrons migrates to the Pt counter electrode through external circuit and participate in chemical reactions at the electrode-electrolyte interface resulting in water splitting reactions. The photocurrent densities for pristine TiO_2 and TiO_2-MoS_2 nanocomposite samples were measured with respect to applied potential under dark and visible light conditions. The difference in the current under light and dark conditions represents the photocurrent and the values are shown in Fig. 4.9. The photocurrent density for pristine TiO_2 was obtained at 0.04 mA/cm^2, which is quite low. However, the TiO_2-MoS_2 nanocomposite samples exhibits significantly higher photocurrent density as compared to pristine TiO_2 which are 0.22, 0.91, 2.27 and 1.21 mA/cm^2, (at 1.0 V) for the samples of MoS_2-TiO_2 nanocomposite samples with 2.5, 5.0, 7.5 and 10.0 wt.% MoS_2 in TiO_2, respectively. The considerably low photocurrent density in pristine TiO_2 photo-electrode is due to large band bap of TiO_2 which responds only to UV (Ultra-violet) light. The enhancement in photocurrent density of TiO_2-MoS_2 nanocomposite photo-electrodes can be understood through two aspects of (i) enhanced visible light absorption and (ii) accelerated photo-excited charge separation. As shown in schematic diagram in Fig. 4.10, TiO_2-MoS_2 nanocomposites exhibits efficient light absorption in the visible region. Also, the TiO_2-MoS_2 nanocomposites could trap more incident light within the nanocomposite material as MoS_2 nanoflakes in TiO_2 nanoparticles may cause multiple reflections due to dispersion of two phase in the nanocomposite sample. This can further increase photon absorption and thus PEC response. In addition, the band alignment between MoS_2 and TiO_2 is favourable for the electron transfer from the conduction band (CB) of MoS_2 to the CB of TiO_2 which suppresses the photo-generated carrier recombination in TiO_2 effectively. Moreover, upto 7.5 wt.% TiO_2-MoS_2 nanocomposite sample, the TiO_2

particles seem to connected with the neighbouring MoS_2 nanoflakes and act as bridge routes which benefit the electron transfer along the TiO_2 channel to the conductive substrate. Mixing of two phases as seen in the SEM and TEM micrographs of the nanocomposite samples indicate this type of morphology. At higher concentration, MoS_2 nanoflakes may not be uniformly distributed due to segregation and thus screen the TiO_2 nanoparticle surface from photo-electro-chemical reaction. This may be responsible for decrease in photo-electro-chemical (PEC) activity at higher concentration of MoS_2 nanoflakes, thus making 7.5 wt. % concentration as the optimum concentration of MoS_2 nanoflakes for highest photo-electro-chemical activity.

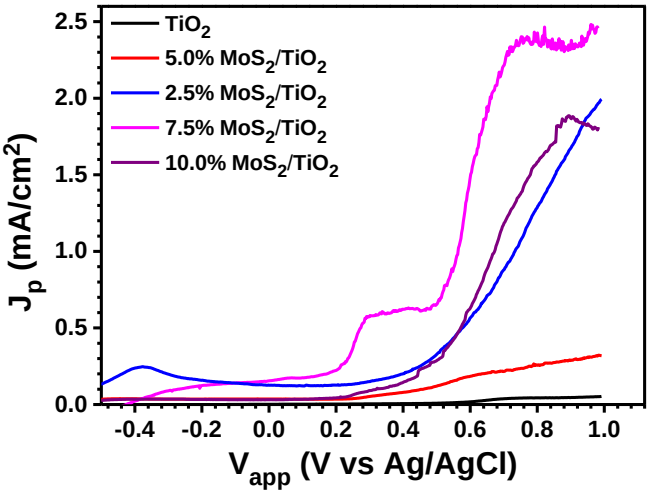

Figure 4.9: Photocurrent density vs. applied potential (V vs. Ag/AgCl) curves for TiO_2 and MoS_2-TiO_2 measured in 1M NaOH solution under visible light illumination.

There are two factors which inhibit the performance of as photocatalyst in water splitting applications. The first limitation is its relatively large optical band gap, about 3.2 eV, which limits its photo response only in UV light; the other being rapid recombination of photogenerated electron-hole pairs, which results in a low quantum efficiency and exhibit low photocatalytic activity under visible light illumination[184]. In the present studies, use of lower band gap of 2D MoS_2 nanoflakes and choosing the optimum concentration of 7.5% results in increased visible light absorption in the

nanoparticle samples. The present study shows that 7.5% MoS_2 is the optimum concentration in terms of increase in the PEC response. In addition to the visible light absorption, the large interface between TiO_2 and MoS_2 increasing the charge separation by forming the junction with is also important for improved performance. This is derived from the recent literature which shows that the layered two-dimensional transition metal dichalcogenides (TMDs), such as molybdenum disulphide (MoS_2) based TiO_2 nanocomposite (TiO_2-MoS_2), satisfy the above-mentioned requirements[185-192]. In TiO_2-MoS_2 nanocomposite, MoS_2 may also play the role of an effective photosensitizer to enhance the photoactivity of TiO_2[193-195]. For a given nanocomposite system, interface band alignment is important for the electron–hole separation, which is desired to be tuned to enhance the charge separation efficiency. It has been observed that type II band alignment is formed between MoS_2 and TiO_2, which is beneficial for the separation of photogenerated electrons and holes[196]. Since MoS_2 2D layers are one atomic layer to few atomically thin layers, interfacial interactions are expected to be pronounced with a strong effect on their charge transport properties[196]. At higher concentration, MoS_2 nanoflakes which are not an integral part of the nanocomposite topography seem to screen the TiO_2-electrolyte interface resulting in lower performance

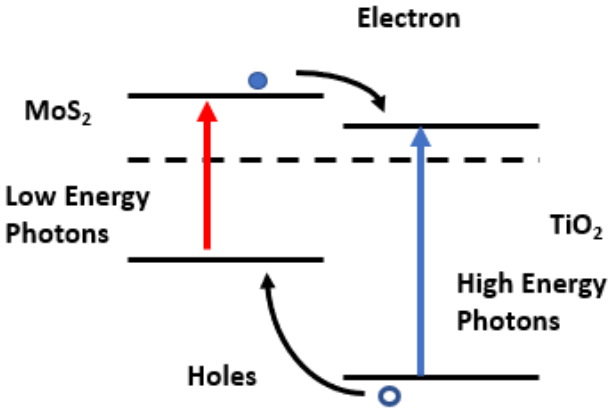

Figure 4.10: Energy band diagram of MoS_2-TiO_2 nanocomposite shows absorption of low energy photons and separation of photogenerated electrons and holes due to favorable band alignment.

4.3 Conclusions

In summary, MoS_2-TiO_2 nanocomposites having various concentration (2.5, 5.0, 7.5, 10.0 wt. %) of MoS_2 nanoflakes have been prepared by two step hydrothermal method. A reduction in absorption edge was observed in MoS_2-TiO_2 nanocomposites. An important result of the present study is that there is an optimum value of MoS_2 concentration at which the PEC response is maximum and further increase in concentration results in degradation in response. The MoS_2-TiO_2 nanocomposite sample with an optimum concentration of 7.5 wt. % possesses highest photo-catalytic and photo-electro-chemical activity which is due to the appropriate amount of MoS_2 which increases visible light absorption and prohibits the recombination of photo-generated charge carriers in TiO_2-MoS_2 nanocomposite samples without screening TiO_2 surface from photo-electro-chemical reaction. The present study also shows that there is electronic interaction at the TiO_2-MoS_2 interface. In addition, highly apparent photocatalytic reaction rate constant was observed in 7.5 wt. % MoS_2-TiO_2 nanocomposite sample which is about 17 times than that observed for pristine TiO_2 nanoparticles.

Chapter 5

$BiVO_4$-TiO_2 core-shell heterostructure

5.1 Introduction

In the present study, pristine $BiVO_4$, TiO_2 and $BiVO_4$-TiO_2 core-shell heterostructure nanoparticles are prepared by hydrothermal methods and studied for structural, morphological, optical, photo-electrochemical (PEC) water splitting and photocatalytic (PC) degradation. Both pristine $BiVO_4$ and TiO_2 exhibit poor PEC and PC performance under visible light illumination. However, an enhanced PEC and PC activity in $BiVO_4$-TiO_2 core-shell heterostructure is observed due to high solar energy absorption and superior charge separation properties in core-shell nanoparticles. The main objective of the present study is to understand the role of low band gap core nanoparticle coated with TiO_2 shell on the PEC properties

5.2 Results and Discussion

5.2.1 Structure and morphology

Pristine TiO_2, $BiVO_4$ and $BiVO_4$-TiO_2 core-shell nanoparticles are characterized for the determination of the crystal phase structure and phase purity by XRD technique and the results are shown in Fig 5.1. XRD peaks for TiO_2 samples are observed at 2θ values of 25.5, 37.9, 48.2 and 55.06 which correspond to (101), (004), (200) and (105) planes, respectively of anatase phase of TiO_2.[197]. In case of $BiVO_4$ nanoparticle sample, peaks are observed at 2θ values of 29 , 31, 35, 40, 42, 46, 47, 49,53,56, and 59^o corresponding to (112), (004), (202), (114), (105), (213), (204), (220), (116), (301) and (107) hkl indices of monoclinic phase of $BiVO_4$ phase [198]. In case of $BiVO_4$-TiO_2 core shell samples, XRD peaks corresponding to both anatase TiO_2 and monoclinic $BiVO_4$ phases are observed. The absence of any other phase and the observation of peaks

corresponding to main phases indicate the absence of other impurity phase or mixed phase. This confirms that both TiO_2 and $BiVO_4$ phases with their crystal structure preserved are present in core-shell nanoparticle sample.

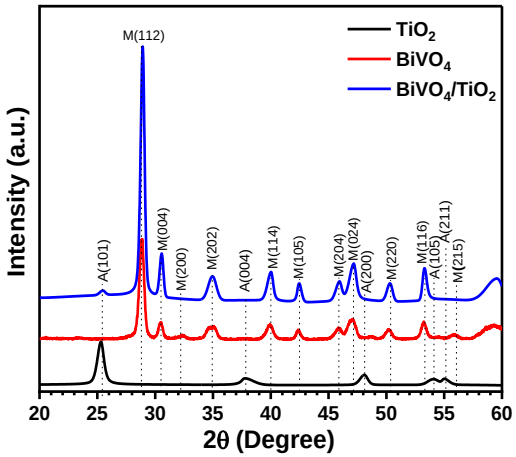

Figure 5.1: X–ray diffractogram of a) $BiVO_4$ nanoparticles and b) TiO_2 nanoparticles c) $BiVO_4$-TiO_2 core-shell nanoparticles. hkl indices of different XRD peaks are shown. B and T represents XRD peaks corresponding to $BiVO_4$ Monoclinic phase and TiO_2 Anatase phase, respectively.

5.2.2 Nanoparticle Morphology

Surface morphology obtained from scanning electron microscopy investigations (SEM) for pristine $BiVO_4$, TiO_2 and $BiVO_4$-TiO_2 core-shell nanoparticles are shown in Fig. 5.3. SEM micrograps for pristine $BiVO_4$ indicate dendritic shaped nanoparticles within the size range of around 80-100 nm. SEM image for TiO_2 nanoparticles show quasi-spherical nanoparticles with size of about 10-15 nm. SEM micrograph of the core shell nanoparticle indicate the coverage of the dendric shaped features with an overlayer.

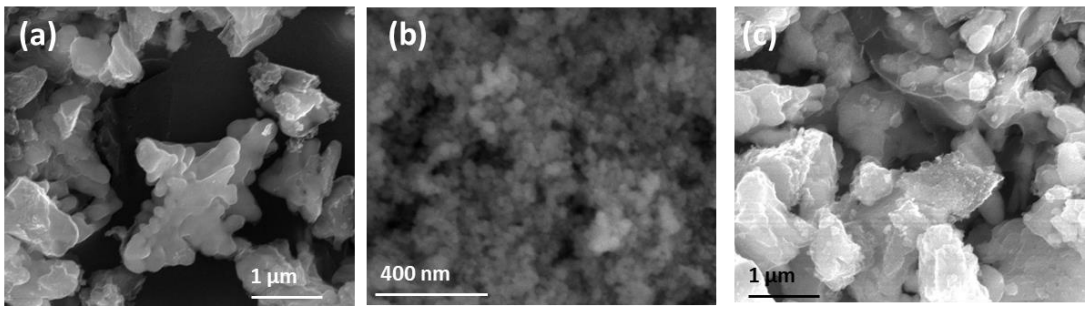

Figure 5.2: SEM micrographs of a) $BiVO_4$ nanoparticles b) TiO_2 nanoparticles and c) $BiVO_4$-TiO_2 core-shell nanoparticle samples.

Transmission electron microscopic (TEM) images of $BiVO_4$, $TiO_2$and $BiVO_4$-TiO_2 core-shell nanoparticlesare shown in Fig. 5.3. TEM images cleary show the formation of nanoparticles with an average particle size of about 80-100 nm for $BiVO_4$ (Micrograph a) and 10-15 nm for TiO_2 (Microrgraph b) samples. TEM analysis of sample $BiVO_4$-TiO_2 core-shell nanoparticles (Micrographs c & d) clearly show anapproximately 10 nm thick overlayer of TiO_2 around $BiVO_4$ core nanoparticles. Further, the core-shell composition is confirmed by energy-dispersive X-ray spectroscopy (Micrograph e & f), which revealed clearly that $BiVO_4$ samples is composed of Bi, V and O only however, in $BiVO_4$-TiO_2 core-shell nanoparticle one additional element Ti is present.

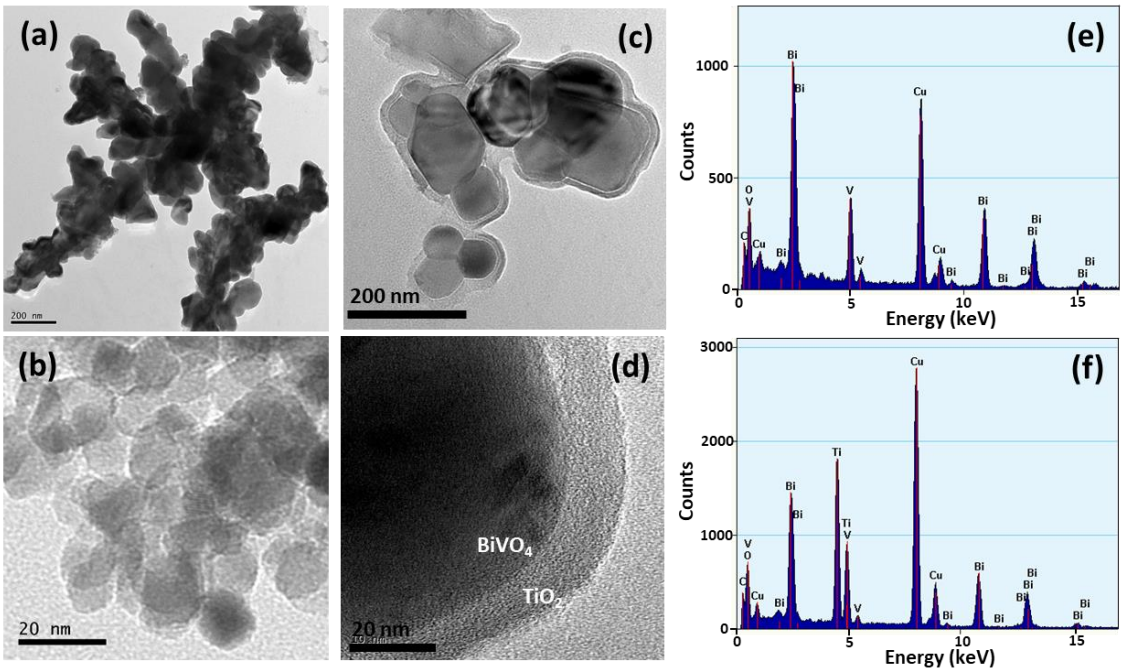

Figure 5.3: TEM images of a) $BiVO_4$ nanoparticles showing dendritic structure b) TiO_2 nanoparticles showing agglomerated structure c) $BiVO_4$-TiO_2 core-shell nanoparticles and d) magnified image of $BiVO_4$-TiO_2 core-shell nanoparticles clearly showing the formation of core-shell structure. TEM-EDS analysis of e) $BiVO_4$ nanoparticles and f) $BiVO_4$-TiO_2 core-shell heterostructures.

5.2.3 Optical properties

Diffuse reflectance spectra (DRS) of pristine $BiVO_4$, TiO_2 and $BiVO_4$-TiO_2 core shell nanoparticles obtained by spectrophotometry technique on bulk samples are shown in Fig.5.4. From these results absorption spectra is obtained and the results are shown in Fig 5.5. Pristine $BiVO_4$ nanoparticle sample exhibit an absorption edge at 530 nm, while pristine TiO_2 nanoparticle sample show the absorption edge at 375 nm. Anatase TiO_2 exhibits a prominent absorption edge in the UV region of solar spectrum, however, the $BiVO_4$ samples exhibits the optical absorption in visible region which stated at around 530 nm with absorption tail extending up to 660 nm.

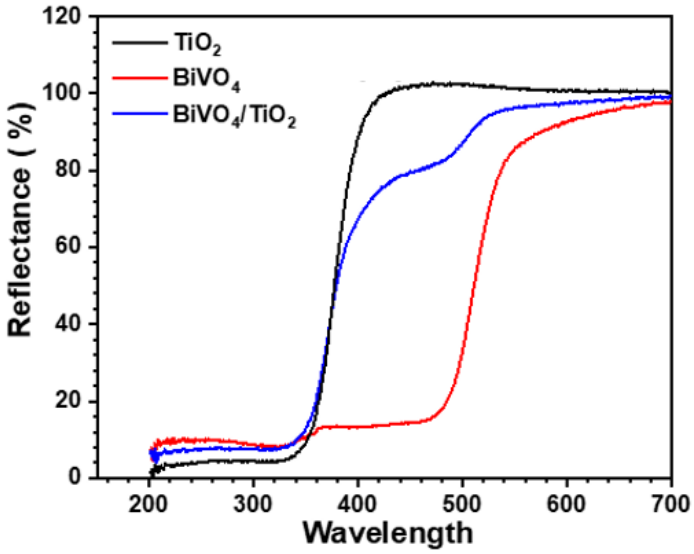

Figure 5.4: DRS spectra of $BiVO_4$, TiO_2 and $BiVO_4$-TiO_2 core-shell nanoparticles. Two absorption features for core-shell nanoparticles are observed.

The estimated band gap from the DRS spectra consistent with the known values of band gap values of 2.4 eV and 3.2 eV for $BiVO_4$ and TiO_2, respectively. The absorption edge values obtained in both the cases are in a good agreement with earlier reported values for the anatase TiO_2 and monoclinic $BiVO_4$. Due to nanoparticle effect, a slight increase in the absorption edge values is expected. DRS spectrum of the $BiVO_4$-TiO_2 core-shell heterostructures validates the generation of a new energy level, as a clear red shift of

the absorption edge is observed compared with that of the TiO_2. The $BiVO_4$-TiO_2 core-shell heterostructures demonstrate a characteristic absorption spectrum, and the fundamental absorption stopping edge at $\lambda \approx 510$ nm lies within the visible light region. Because of the presence of two phases, two absorption edge features are clearly observed. This clearly shows that increased absorption in the visible region due to the visible optical absorption in $BiVO_4$ core. Thus, both UV and visible light can be utilized by $BiVO_4$-TiO_2 core-shell nanoparticle which may potentially lead to improved photocatalytic activity of $BiVO_4$-TiO_2 core-shell nanoparticles because of increase in the photon absorption.

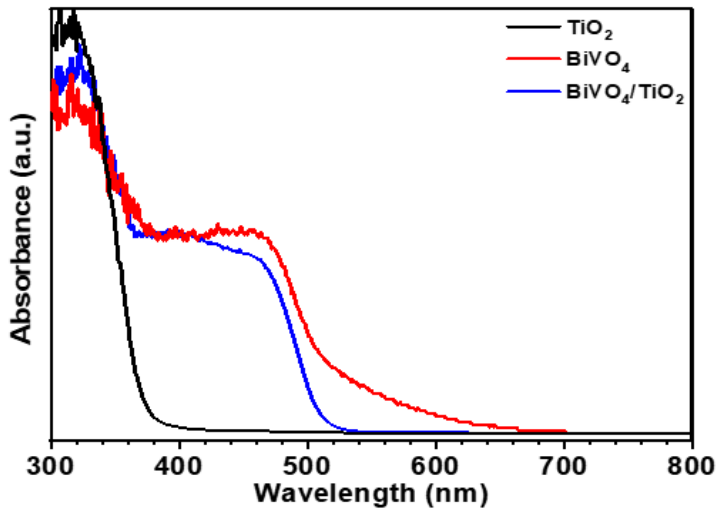

Figure 5.5: Absorbance spectra of $BiVO_4$, TiO_2 and $BiVO_4$-TiO_2 core-shell nanoparticles obtained from DRS measurements.

5.2.4 Photocatalytic Investigations

The photocatalytic activity of all three samples is evaluated by measuring the time-dependent degradation of methylene blue (MB) under visible-light irradiation. From Fig. 5.6, we can see that the pristine $BiVO_4$ and TiO_2 sample shows poor photocatalytic activity in the visible-light. The degradation rate constant k of pristine TiO_2 and $BiVO_4$ are calculated as $\sim 3.4 \times 10^{-3}$ and 2.9×10^{-3} min^{-1}. This small value is attributed to the large band gap energy of TiO_2. For the $BiVO_4$-TiO_2 samples, the photodegradation

activity increases and the photodegradation rate constant k reaches the maximum ~8.4×10^{-3} min^{-1}. This value is approximately three times of magnitude higher than that of pristine TiO_2 under visible-light irradiation (Fig. 5.6). To check the long stability of the defect generated in $BiVO_4$-TiO_2 samples when stored under ambient conditions, we used $BiVO_4$-TiO_2 samples to re-examine the photocatalytic and photo-electrochemical application tests. We found that $BiVO_4$-TiO_2 samples still exhibit the enhanced photocatalytic activity for phenol degradation.

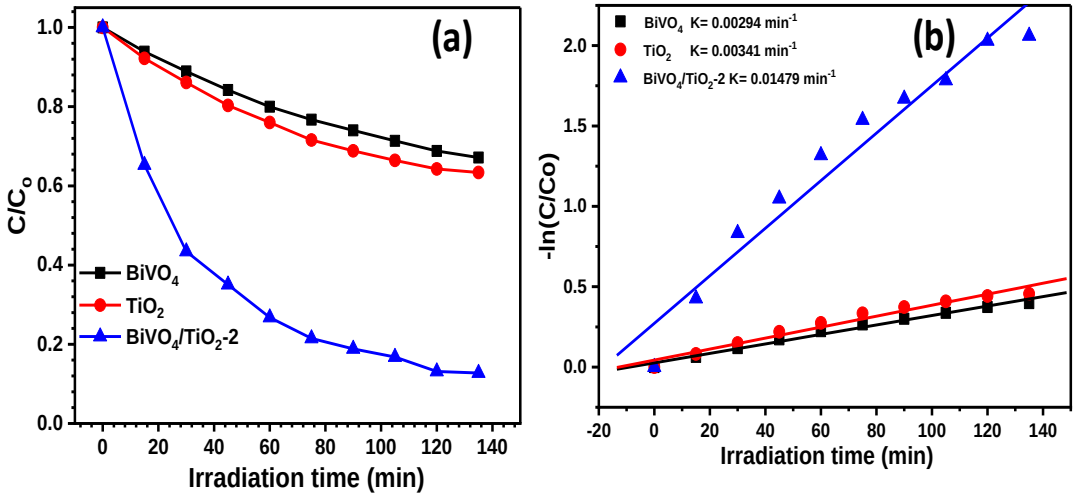

Figure 5.6: a) Solar-light driven photocatalytic decomposition of methylene blue and (b) rate constant calculation for $BiVO_4$, TiO_2 and $BiVO_4$-TiO_2 core-shell nanoparticles.

5.2.5 Photo-electrochemical properties

The main objective of this study is to investigate the effect of core-shell nanoparticle formation on the photo-electrochemical response. For this, the pristine $BiVO_4$, TiO_2 and $BiVO_4$-TiO_2 core-shell nanoparticles were used as working electrode in a photo-electrochemical cell to investigate the solar water splitting activity. The photocurrent density for both the pristine and core-shell nanoparticles is calculated by subtracting the value of dark current from that of light current and then by dividing it by the exposed area (0.5 cm^2) of the samples to the incident light. Results are shown in Fig.5.7. It can

be noted that $BiVO_4$-TiO_2 core shell nanoparticle sample shows (Fig 5.7) the photocurrent density in cathodic side, which correspond to p-type nature of the core-shell nanoparticles. Whereas, pristine TiO_2 and $BiVO_4$ nanoparticles samples show the photoanodic behavior which correspond to n-type behavior for both $BiVO_4$ and TiO_2 nanoparticles. The change from anodic to cathodic behavior in core-shell nanoparticles is an important result and will be discussed in more details later. Maximum photocurrent density of 0.1 mA/cm^2 was obtained for $BiVO_4$-TiO_2 core–shell nanoparticles at -0.8 V/Ag/AgCl as compared to value of 0.006 mA/cm^2 in case of $BiVO_4$ and 0.04 mA/cm^2 for TiO_2. The photocurrent density values obtained for $BiVO_4$-TiO_2 core-shell nanoparticles is approximately 2.5 times higher than of TiO_2 nanoparticle which may be attributed to the enhanced optical absorption and efficient charge separation charge separation at the interface of the $BiVO_4$ and TiO_2, probably due to of built in electric field at the $BiVO_4$ and TiO_2 interface.

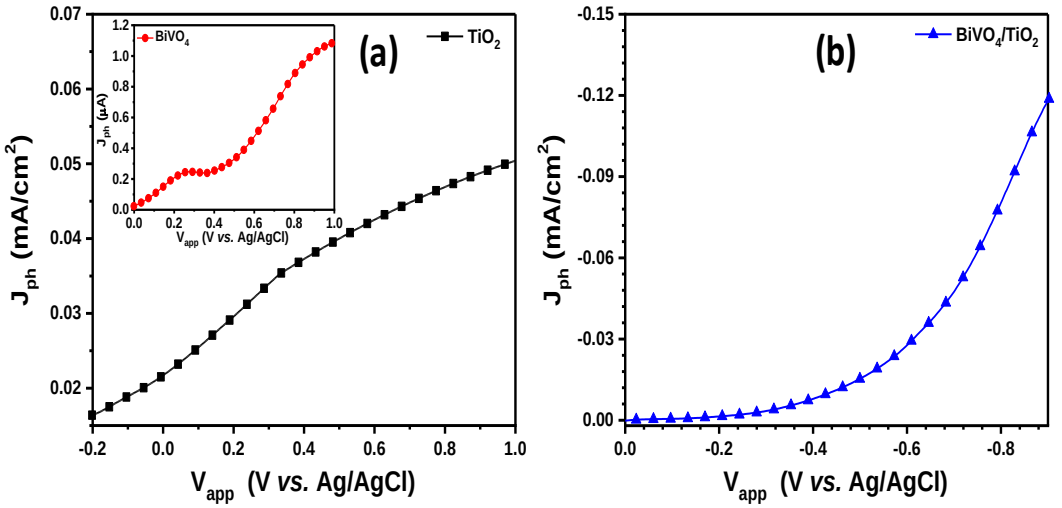

Figure 5.7: Photocurrent vs. applied bias curves for a) TiO_2 nanoparticle samples, $BiVO_4$ nanoparticle (in inset) and b) $BiVO_4$-TiO_2 core-shell nanoparticles. Interestingly, both $TiO_2$and $BiVO_4$ nanoparticles exhibits the anodic behavior of and relativily low photocurrent density, however, the $BiVO_4$/TiO_2 core-shell nanoparticles show cathodic behavior with relatively large value of photocurrent density.

5.2.6 Electrochemical Impedance spectroscopy

The charge transfer process at the electrolyte and semiconducting material surface is investigated using electrochemical impedance spectroscopy (EIS) measurements under light conditions. Fig. 5.8 show the Nyquist plots for pristine $BiVO_4$, TiO_2 and $BiVO_4$-TiO_2 core-shell nanoparticles. As shown in Fig. 5.8, it is evident that the radii of semicircle on the real axis of Nyquist plots of $BiVO_4$-TiO_2 core-shell heterostructured sample is much smaller than those for pristine $BiVO_4$ and TiO_2samples, which indicates that the core-shell heterostructured reduces the semiconductor–electrolyte contact resistance and improves the charge transport. Therefore, the charge transport efficiency in $BiVO_4$-TiO_2 core-shellheterostructured sample increased significantly both on the surface (i.e., surface reaction kinetics) and in the bulk, leading to an improved PEC activity[199].

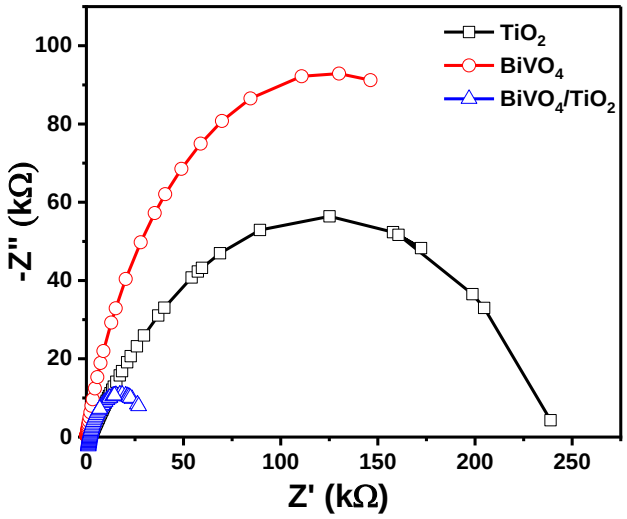

Figure 5.8: EIS spectra of for a) $BiVO_4$, b) TiO_2 and c) $BiVO_4$-TiO_2 core-shell nanoparticles.

5.2.7 Mott Schottky Measurements

To determine the electrical properties of $BiVO_4$, TiO_2 and $BiVO_4$-TiO_2 core-shell nanoparticle interface, Mott–Schottky measurements were carried out at 1 kHz AC signal frequency in 1M NaOH solution under dark conditions to calculate the flat band

potential (V_{FB}) by using the Mott–Schottky equation. Fig. 5.9 shows the Mott–Schottky plots ($1/C^2$ *vs* applied bias) for pristine $BiVO_4$ and TiO_2 and $BiVO_4$-TiO_2 core-shell heterostructure. The flat-band potential values of these samples were obtained from the linear fit of the data of these curves using a $1/C^2$*vs* V relationship[200]. The pristine $BiVO_4$ and TiO_2 show a negative slope of a linear region of a plot indicating its n-type nature with a flat band potential values of -0.38 and -0.30 volts (*vs* Ag/AgCl), respectively. However, $BiVO_4$-TiO_2 sample shows the positive slope of a linear region of a plot indicating its p-type nature with a flat band potential values of 0.58 V (*vs* Ag/AgCl). The positive value of flat band potential value for the $BiVO_4$-TiO_2 core-shell nanoparticle based photoelectrode indicates photocathodic behavior. This change in the electronic nature of $BiVO_4$-TiO_2 nanoparticles in comparison to $BiVO_4$ and TiO_2 nanoparticles is in consistent with photo-electrochemical results. The more positive values of flat band potential indicate better efficient charge transport at electrolyte-semiconductor interface and its higher photo-electrochemical activity.

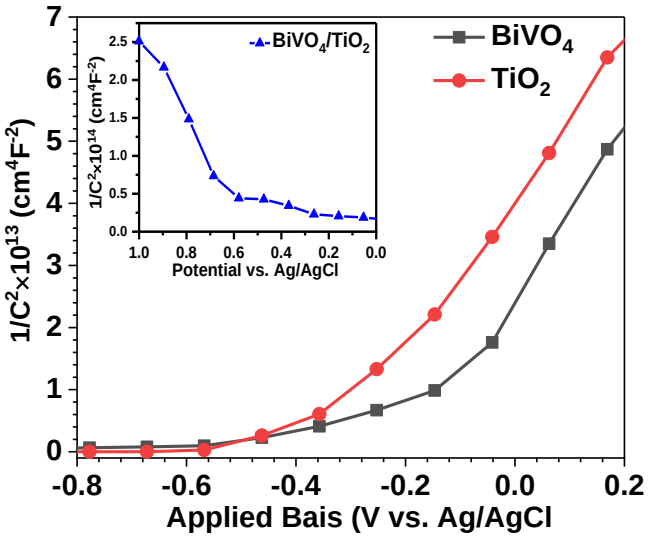

Figure 5.9: $1/C^2$ vs V curves for a) $BiVO_4$ b) TiO_2 and c) $BiVO_4$-TiO_2 core-shell nanoparticles (in inset)

5.2.8 Discussion

The central objective of the present study is to improve the solar energy absorption capacity by making the core-shell heterostructure using two semiconductor materials having different optical properties. Shell of a wide band gap (TiO_2) materials and nanoparticle core of smaller band gap ($BiVO_4$) semiconductor have been used and the properties of core shell nanoparticle has been compared with those of $BiVO_4$ and TiO_2 nanoparticles of similar sizes. $BiVO_4$ nanoparticles samples showed lower photocurrent density due to poor carrier transport properties because of lower hole diffusion length[201]**.** The present strategy of using core-shell heterostructure resulted in photogenerated carriers very close to $BiVO_4$-TiO_2 interface. Surface catalytic properties of the semiconductor surface in contact with liquid electrolyte is also very important. TiO_2 surface is known to have superior surface photocatalytic properties in comparison to other semiconductors, as well as high stability in liquid electrolyte[202]. Therefore, the use of TiO_2 shell in core-shell nanoparticle is expected to result in stability and better surface catalytic properties. Further, for improving the charge transfer in a heterojunction, a favorable band alignment is an important pre-requisite. The favorable potential difference between $BiVO_4$ and TiO_2 for efficient charge transfer has also been reported in thin film heterojunction[203]. The improved properties at $BiVO_4$ and TiO_2 interface explained in terms of favorable Fermi level alignment in the $BiVO_4$/TiO_2 interface with conduction band of $BiVO_4$ higher than that of TiO_2 resulting in a type II band alignment. This will favor photoelectrons created in $BiVO_4$ being efficiently transferred to TiO_2 preventing recombination and efficient PEC reaction at TiO_2/ electrolyte interface. Based on our photo-electrochemical results, it can be confirmed that the separation of photogenerated charge carriers of $BiVO_4$ nanoparticles could be enhanced after making the $BiVO_4$-TiO_2 core-shell heterostructure by

depositing a thin TiO_2 shell. Accordingly, there is an increase in photocatalytic activity for the degradation of methylene blue dye under visible-light irradiation. In previous studies, it has been reported that the increased separation of photogenerated charges in $BiVO_4$-TiO_2 heterostructure, when TiO_2 is in contact with electrolyte as a top layer, are mainly attributed to the uncommon transfers of photo-excited highenergy electrons from bottom $BiVO_4$ layer to top TiO_2 layer. When $BiVO_4$-TiO_2 core-shell is illuminated by one sun radiation to excite the charge carriers, the TiO_2 shell layer absorbs the UV radiation shorter than 375 nm. The remaining light with radiation larger than 375nm and shorter wavelengths than 530 nm reaches to excite the $BiVO_4$ core and generate a large concentration of high-energy electrons (e) in $BiVO_4$ above the conduction band (CB) with positive holes (h^+) left in the valence band (VB). Generally, these high-energy electrons are active for water reduction, because they possess a higher energy level than that standard hydrogen electrode (SHE) of water reduction, while the holes would be captured by water to oxidize. However, it should be noted that the high-energy electrons migrated easily to the bottom of the CB in a remarkably short time, as they relax and then immediately recombine with the holes at the VB, leading to weakened charge separation with a lowered photoactivity. Interestingly, when the $BiVO_4$ is coupled with TiO_2 in core–shell configuration, the visible-light-excited high-energy electrons of $BiVO_4$ would thermodynamically transfer to the CB of TiO_2, which prolongs the lifetimes of the high-energy electrons. In addition, it is well known that the CB energy level of TiO_2 is higher than that of water reduction potential, meaning that the transferred high-energy electrons can be used directly for hydrogen generation.

One of the most important finding in the result of the present study is the change in the nature of PEC response from anodic behavior of TiO_2 and $BiVO_4$ nanoparticle samples to cathodic behavior for $BiVO_4$/TiO_2 core- shell nanoparticles along with enhanced

PEC response. The change in the work function due to nanoparticle size, core-shell nanoparticle configuration and interaction of nanoparticle with water may be responsible for the change in this electronic behavior. The above discussion supports this conjecture. the enhancement mechanism of charge separation in $BiVO_4$-TiO_2 type-2 heterojunction[204].

Work function of a semiconductor surface is one of the most important parameters determining band alignment at the interface important for metal-semiconductor contacts, photovoltaic junction and photo-electro-chemical devices. In the context of the present study, effect of interaction of semiconductor surface with water adsorbed is important. Studies for measuring the surface properties of semiconductors and changes on water adsorption are normally performed at liquid nitrogen or lower temperature in vacuum conditions involving adsorption of few layers of water. It is clear that this can give results different from when a semiconductor is in direct contact with liquid electrolyte as in case of photo-electro-chemical cell. Despite its importance, work function of widely used TiO_2 semiconductor has only been investigated in limited studies[205]. In an interesting study, the effect of surface treatment (oxidation and annealing) has been carried out[206]. The results show overall variation of work function to be 1.74, 2.14 and 1.39 eV for Anatase (001), Anatase (101) and polycrystalline Anatase, respectively. Work function is found to be in the order: oxidized> stoichiometric> annealed>sputtered. As discussed above, work function values can get modified by surface conditions, stoichiometry, doping, surface charge layers or the surface dipole [207]. As work function is difference in the Fermi energy and vacuum level energy, it may also change with any change in these parameters. In the context of present study involving application of TiO_2 and $BiVO_4$ nanoparticles for water splitting, interaction of semiconductor surface with water may also result in some changes.

Distribution of vacancies may also influence interface of TiO_2 and water[206]**.** There is a general agreement that water interaction with TiO_2 will affect work function of a semiconductor surface, but it is not clear which way and how much is the effect on the change in work function values as adsorption affect the work function values of surface[207]. In a study on effect of work function on water adsorption, work function has been measured and shown that it can vary in the range of 4.70-6.44, 4.62-6.76 and 4.51-5.62 eV for (001), (101) and polycrystalline surfaces, respectively[206].

One of the most important result of the present study is the change in the nature of PEC response from anodic response for TiO_2 and $BiVO_4$ nanoparticle samples to cathodic response for $BiVO_4/TiO_2$ core- shell nanoparticles along with enhanced photo-electro-chemical response. The change in the work function due to nanoparticle size, core-shell nanoparticle configuration and interaction of nanoparticle with water may be responsible for the change in this electronic behavior. The above discussion supports this conjecture.

5.3 Conclusions

In summary, pristine $BiVO_4$, TiO_2, and $BiVO_4$-TiO_2 core-shell heterostructure nanoparticle have been fabricated by chemical method. TEM analysis confirm the formation of core-shell nanoparticles.The present study shows that the fabricated core–shell heterostructure can not only provide a high optical absorption in visible region, but also cause the formation of a staggered $BiVO_4$-TiO_2 core -shell nanoparticle heterojunction to promote the charge separation and transfer, leading to a significantly enhanced photo-electrochemical water splitting efficiency and high rate of photocatalytic degradation of organic pollution as compared to pristine $BiVO_4$ and TiO_2 nanoparticles.The change in PEC response from anodic (for TiO_2 and $BiVO_4$ nanoparticles) to cathodic for $BiVO_4$-TiO_2 core-shell nanoparticles is explained on the

sensitive dependence of work function values to surface conditions, nanoparticle effect, core-shell configuration and interaction of core-shell nanoparticle with water.

Chapter 6

Summary and Scope of Further Work

6.1 Summary

The present study has been carried out with the objective of modifying the optical absorption, surface catalytic and charge separation properties of TiO_2 nanoparticles using novel and widely different methodologies and for understanding the relationship between the modified properties and the enhanced photo-electrochemical response. Three different methodologies have been employed to achieve the stated objectives of the present thesis. Post deposition hydrogenation surface treatment in mild vacuum hydrogen environment has been employed for modifying the optical absorption and surface catalytic properties of TiO_2 nanoparticles. Synergetic combination of layer dependent properties of MoS_2 2D nanoflakes and size dependent properties of TiO_2 nanoparticles have been ultized by forming 1D-2D nanocomposites. Use of core-shell nanoparticles with the core comprising of a lower band gap material ($BiVO_4$) and the shell comprising of a chemically stable oxide material having efficient surface catalytic properties (TiO_2) has resulted in an improved PEC response. The important take away from the thesis work are an improved basic understanding of the relationship between materials properties and the device performance. The novel nanostructures having tailorable properties have been fabricated by simple chemical methods that are suitable for low cost and large area applications.

The important results of the present thesis investigation can be summarized as follow:

1. Vacuum hydrogenation treatment has been utilized to modify the optical absorption properties of TiO_2 nanoparticles. The main advantage of carrying out the hydrogenation treatment in a mild vacumm environment (at 10^{-2} Torr

pressure) is the possibility of controlled modification of the properties of TiO_2 nanoparticles by controlling the hydrogenation environment. Detailed and comprehensive characterization of pristine and hydrogenated TiO_2 nanoparticles using diverse and complementary characteriation tools has provided an improved understanding of the modified properties. NMR and EPR measurements have shown that the presence of Ti^{3+} defects and corresponding energy states in the bandgap of TiO_2 results in increased absorption in visible part of the spectrum at energy values lower than the band gap of TiO_2. As the samples were synthesized under rather mild hydrogen conditions, it has been concluded from the DFT simulations that the majority of oxygen vacancies are not occupied by atomic hydrogen, which results in occupied midgap states. This study has also identified the conditions that favor the formation of localized or delocalized states due to vacancies. This is important in suitably selecting the hydrogenation treatment conditions useful for improved PEC response. Formation of amorphous TiO_2 shell and structural defects present in the crystalline nanoparticle core, as revealed by HRTEM, XRD, Raman spectroscopy and other characterization techniques, improved the surface catalytic properties.

2. TiO_2-MoS_2 nanoflake-nanoparticle composite has been used for utilizing the layer and size dependent properties of 1D and 2D nanocomposites, respectively. In addition, a large surface and interface area of the 1D-2D nanocomposite results in an improved charge-separation property at the interface. It has been shown that the two components maintain their structural and compositional integrity and the chemical mixing is minimal as revealed by XRD, HRTEM, Ramam and XPS spectroscopy studies. XPS results show that there is electronic

interaction at the TiO_2-MoS_2 interface which may be responsible for the improved carrier seperation at the TiO_2 and MoS_2 interface. An important result of the present study is that there is an optimum value of MoS_2 concetration (7.5 w%), upto which the increased abosption in lower photon energy and charge separation at the TiO_2-MoS_2 inerface favours the improvement in PEC response. At higher MoS_2 concentration, a possible screening of superior surface catalytic properties of TiO_2 results in lowering the PEC response.

3. In an important investigation of the present study, the structural, optical and electronic properties of $BiVO_4$-TiO_2 core-shell nanoparticle have been compared with TiO_2 and $BiVO_4$ nanoparticle prepared by similar methods and having similar dimensions. The improved PEC response of the core-shell nanoparticle is accompanied by the change in anodic response of TiO_2 and $BiVO_4$ nanoparticle to cathodic response of the core-shell nanoparticles. A possible modification in the work function values due to the presence of a thin TiO_2 shell and the modification in the semiconductor properties at semiconductor- electrolyte interface may be responsible for this large change in the nature of the PEC response.

4. As summarized above, modification in the properties of TiO_2 nanoparticles on hydrogenation, nanocomposite formation with MoS_2 and core-shell nanoparticle with $BiVO_4$ has resulted in the improved PEC response. Especially in case of TiO_2-MoS_2 nanocomposite samples, higher photocurrent density of 2.27 mA/cm^2, (at 1.0 V) is observed for the samples of MoS_2-TiO_2 nanocomposite samples 7.5 wt.% MoS_2 in TiO_2. As these samples are prepared using simple chemical synthesis techniques suitable for low cost and large area applications, these results can be potentially used in large scale applications.

6.2 Scope for further work

1. Hydrogenation treatment of TiO_2 nanoparticle investigated in the present study may be extended to other oxide materials. The nature of the defect depends upon the chemistry of hydrogenation of the oxide material in addition to the hydrogenation conditions (as shown in the present study). This research direction is therefore, potentially useful for further improving the understanding of the role of defect type and its concentration in improving optical and electronic properties and the the resulting catalytic and PEC properties.

2. In the present study, the effect of concentration of MoS_2 2D nanoflakes on the optical and photo-electrochemical properties has been investigated. As was mentioned earlier, it is important to study the effect of thickness or number of atomic layers on the optical and catalytic properties and resulting photo-electrochemical properties.

3. It may also be useful to apply the methodology used in this thesis work using other 2D materials like WS_2, WSe_2 or $MoSe_2$. As the optical properties of these 2D layers are very different from that of MoS_2 (used in the present study), this is expected to result in improvement in the light absorption at different parts of the solar spectrum. This is of potential interest not only for PEC devices but also for solar cell and other optoelectronic devices. It is proposed that multiple 2D layers of different materials having appropriate band gap values and absorption coefficients may be used to improve the visible light absorption in a broader spectral range. 2D layers having diverse advantages like highly conducting nature (graphene) and visible light absorption (MoS_2) and superior catalytic properties may result in a comprehensive improvement in PEC properties.

4. Application of core-shell nanoparticles with other stable oxide materials may also be investigated. It is also important to study the effect of nanoparticle size and shell thickness on the optical and electronic properties and the resulting PEC response.

List of Publicatons

Publications in Journals

1. Hydrogen Treated Anatase TiO_2: A New Experimental Approach and Further Insights from Theory, Manan Mehta,Nisha Kodan, Sandeeep Kumar,Akshey Kaushal, Leonhard Mayrhofer,Michael Walter,Michael Moseler,Avishek Dey,Satheesh Krishnamurthy,SuddhasatwaBasuandAadesh P. Singh, Journal of Materials Chemistry A 4,2670 (2016).
2. Synthesis of MoS_2-TiO_2 nanocomposite for enhanced photocatalytic and photo-electrochemical performance under visible light irradiation, Manan Mehta, Aadesh P. Singh, Sandeeep Kumar, Satheesh Krishnamurthy, Björn Wickman and SuddhasatwaBasu, Vacuum, 155, 675 (2018).
3. Synthesis, structural and photo-electrochemical properties of $BiVO_4$-TiO_2 core-shell nanoparticles, Manan Mehta, Aadesh P. Singh, Satheesh Krishnamurthy, Björn Wickman and SuddhasatwaBasu (Accepted for publication in Journal of Materials Today Chemistry, 2020).

Presentations in conferences:

4. Hydrogen treatment of TiO_2 nanoparticles for photo-electrochemical applications, Manan Mehta, Aadesh P. Singh, Satheesh Krishnamurthy and SuddhasatwaBasu, National Conference on Semiconductor Materials and Devices, 4-6 March 2016, IIT Jodhpur, India.
5. Photo-electrochemical propertiesof TiO_2-MoS_2 nanocomposites, Manan Mehta, Aadesh P. Singh, Satheesh Krishnamurthy and SuddhasatwaBasu, European Materials Research Society Meeting (EMRS), 22-26 May 2017, Strasbourg, France.

6. Structural, optical and photo-electrochemical propertiesof TiO_2-MoS_2 nanocomposites, Manan Mehta, Aadesh P. Singh, Satheesh Krishnamurthy and SuddhasatwaBasu, 2nd International Conference on Advanced Energy Materials (AEM), University of Surrey, England, 11-13 September 2017.

7. Photo-electrochemical properites of TiO_2 and TiO_2-$BiVO_4$ core shell nanoparticle for water splitting applications, Manan Mehta, Aadesh P. Singh, Satheesh Krishnamurthy and SuddhasatwaBasu, International Conference on Nanoscience and Technology 2018 (ICONSAT 2018), Indian Institute of Science, Bengaluru, Karnataka (organized by Centre for Nano and Soft Matter Sciences).

8. Core-shell nanoparticles and 2D-3D nanocomposites for photo-electrochemical applications for water splitting, Manan Mehta, Aadesh P. Singh, Satheesh Krishnamurthy and SuddhasatwaBasu, GLAD conference, Delhi, India, 30-31 March 2018**(Best Poster Award).**

9. Nanostructured Materials for photo-electrochemical electrodes for water splitting applications for hydrogen production, Manan Mehta, Aadesh P. Singh, Satheesh Krishnamurthy and SuddhasatwaBasu, Symposium on Advanced Materials Technologies, 20-21 Feberuary 2017, Dehradun, India.

References

1. Midilli A., Rzayev P., Olgun H. and Ayhan T., Solar hydrogen production from hazelnut shells, International Journal of Hydrogen Energy, 25, 723 (2000).

2. International Energy Agency, Renewables in Global Energy Supply, An IEA Fact Sheet, (2002) (https://webstore.iea.org/renewables-in-global-energy-supply).

3. International Energy Agency, World Energy Outlook, International Energy Agency, 75739 Paris Cedex 15, France (2019). (https://www.iea.org/reports/world-energy-outlook-2019).

4. Rzayeva M. P., Salamov O. M. and Kerimov M. K., Modelling to get hydrogen and oxygen by solar water electrolysis, International Journal of Hydrogen Energy, 26, 195 (2001).

5. MIT Energy initiative, The future of solar energy. (2019) http://energy.mit.edu/research/future-solar-energy/.

6. Singh V., Fundamental and use of hydrogen as a fuel, ISST Journal of Mechanical Engineering, 6, 63 (2015).

7. Balat M., Potential importance of hydrogen as a future solution to environmental and transportation problems. International Journal of Hydrogen Energy, 33, 4013 (2008).

8. Wang Z., Roberts R. R., Naterer G. F., and Gabriel K., Comparison of thermochemical, electrolytic, photoelectrolytic and photochemical solar-to-hydrogen production technologies. International Journal of Hydrogen Energy, 37, 16287 (2012).

9. Park K., Kim Y. J., Yoon T., David S., and Song Y. M, A methodological review on material growth and synthesis of solar-driven water splitting photoelectrochemical cells, RSC Advances, 9, 30112 (2019).

10. Fujishima A. and Honda K., Electrochemical Photolysis of Water at a Semiconductor Electrode, Nature, 37, 238 (1972).

11. Gerischer H., Cardon F., Gomes W.P., and Dekeyser W., The principles of Photoelectrochemical energy conversion., In: Photovoltaic and photoelectrochemical solar energy conversion, (Eds.) NATO ASI Summer School, Ghent, Belgium, Plenum, New York, B 69, 199 (1981).

12. Nozik A.J., Photoelectrochemistry: Applications to Solar Energy Conversion, Annual Review of Physical Chemistry, 29, 189 (1978).

13. Heller A., Hydrogen-Evolving Solar Cells, Science, 233, 1141 (1984).

14. Getoff N., Photoelectrochemical and photocatalytic methods of hydrogen production: a short review, International Journal of Hydrogen Energy, 15, 407 (1990).

15. Pleskov Y.V, Solar energy conversion: A photoelectrochemical approach, Springer, Berlin, 176 (1990).

16. Gao L., Cui Y., Vervuurt R.H.J., Dm D.V.,, Rene P. J., Veldhoven V., Hofmann J.P. , Ageeth A., Bol J. E. , Haverkort M., Peter H. L. , Notten E. , Bakkers P. A. M., and Hensen E. J. M., High efficiency InP-based photocathode for hydrogen production by Interface energetics design and photon management, Advanced Functional Materials, 26 (5) 679 (2016).

17. Prévot M. E., and Sivula K., Photoelectrochemical tandem cells for solar water splitting, Journal of Physical Chemistry C, 117, 17879 (2013).

18. Archer M. D., Photovoltaics and photoelectrochemistry: similarities and di¬fferences, Physica E 14, 61 (2002).

19. Sze S.M., Semiconductor devices, Physics and technology, Wiley & Sons, New Jersey (2002).

20. Kittel C., Introduction to solid state physics, 8th Edition, Wiley, New Jersey, 2004.

21. Sze S. M., and Kwok K. N., Physics of Semiconductor Devices, Wiley, New Jersey, (2007)

22. Kahn A., Fermi level, work function and vacuum level, Materials Horizon., 3, 7 (2016).

23. Louise H., and Nicholas E. D., Fundamental losses in solar cells. Progress in Photovoltaics: Research and Applications, 19, 286 (2011).

24. Micha, D.N., and Silvares R.T., The Influence of solar spectrum and concentration factor on the material choice and the efficiency of multijunction solar cells. Scientific Reports, 9, 20055 (2019).

25. Bak T., Nowotny J., M Rekas and Sorrell C. C., Photo-electrochemical hydrogen generation from water using solar energy. Materials-related aspects, Hydrogen Energy, 27, 991 (2002).

26. Gai Y. Q, Li J. B, Li S. S, Xia J. B, and Wei S. H., Design of narrow-gap TiO_2, A passivated codoping approach for enhanced photoelectrochemical activity, Physical Review Letters 102, 036402 (2009).

27. Walter M.G, Warren E.L, McKone J.R, Boettcher S.W, Mi Q.X, Santori E.A, and Lewis N.S, Solar Water Splitting Cells, Chemical Review, 110, 6446 (2010).

28. Jiang C., Savio J. A., Wang M A., Zang T., and Tang J., Photoelectrochemical devices for solar water splitting – materials and challenges, Chemical Society Review, 46, 4645 (2017).

29. Sivula K., van de Krol R., Semiconducting materials for photoelectrochemical energy conversion, Nat Review Materials, 1, 15010 (2016).

30. Jafari T., Moharreri E., Amin A. S., Miao R., Song W., and Steven L. S., Photocatalytic water splitting - The untamed dream; A review of recent advances, Molecules, 21, 900 (2016).

31. Benelmekki M., An introduction to nanoparticles and nanotechnology, Morgan & Claypool Publishers (2015).

32. Chaudhuri G., and Paria S., Core/shell nanoparticles: classes, properties, synthesis mechanisms, characterization, and applications, Chemical Review, 112, 2373 (2012).

33. Gawande M. B., Goswami A., Asefa T., Guo H., Biradar, A. V., Peng D.L, Zboril A., and Verma R. S., Core-shell nanoparticles: synthesis and applications in catalysis and electrocatalysis, Chemical Society Review, 44, 7540 (2005).

34. Cooper D.R., Suffern D., Carlini L., Clarke S. J., Parbhoo R., Bradforth S. E., and Nade J. L., Photoenhancement of lifetimes in CdSe/ZnS and CdTe quantum dot-dopamine conjugates, Physical Chemistry and Chemical Physics, 11, 4298 (2009).

35. Li Y., Sun Z. H., Zhu S.M., Liao Y. L., Chen Z. X., and Zhang D., Synergistically enhanced photocatalytic reduction of CO_2 on N–Fe codoped $BiVO_4$ under visible light irradiation, Carbon, 94, 599 (2015).

36. Linsebigler A.L., Lu G., and Yates J.T., Photocatalysis on TiO_2 surfaces: principals, mechanisms and selected results, Chemical Review, 95, 735 (1995).

37. Sandell A., Sanyal B., Walle L., Richter J., Plogmaker S., Karlsson P., Borg A., and Uvdal P., Probing and modifying the empty –state threshold of anatase TiO_2: Experiments and ab initio theory, Physical Review B, 78, 075113 (2008).

38. Li M., Hebenstreit W., Gross L., Diebold U., Henderson M.A., Jennison D.R., Schultz P.A., and Sears M.P., Oxygen-induced restructuring of the TiO_2(110) surface: A comprehensive study, Surface Science, 437, 173 (1999).

39. Wu C.C., Wu C.I., Sturm J.C., and Kahn A., Surface modification of indium tin oxide by plasma treatment: An effective method to improve the efficiency, brightness and reliability of organic light emitting devices, Applied Phyics. Letters, 70, 1348 (1997).

40. Klissurski D., Hadjiivanov K., Kantcheva M., and Gyurova L., Study of peroxide-modified titanium dioxide (anatase), Journal Chemical Society Faraday Transanctions, 86, 385 (1990).

41. Iwamoto M., Yoda Y., Yamazoe N., and Seiyama T., Study of metal oxide catalysts by temperature programmed desorption, oxygen adsorption on various metal oxides, Journal of Physical Chemistry, 82, 2564 (1978).

42. Hanaor, D.A.H., and Sorrell, C.C. Review of the anatase to rutile phase transformation. Journal of Material Science, 46, 855 (2011).

43. Zhang H., and Banfield J. F., Understanding polymorphic phase transformation behavior during growth of nanocrystalline aggregates: insights from TiO2, The Journal of Physical Chemistry B, 104, 3481 (2000).

44. Asahi, R., Morikawa T., Ohwaki T., Aoki K., and Taga Y., Visible-light photocatalysis in nitrogen-doped titanium oxides, Science, 293, 269 (2001).

45. Byrne C., Fagan R., Hinder S., McCormack D.E., and Pillai S. C., New approach of modifying the anatase to rutile transition temperature in TiO_2 photocatalysts, RSC Advances, 6, 95232 (2016).

46. Moulder J.F., Stickle W.F., Sobol P.E., and Bomben K.D., Handbook of X-ray Photoelectron Spectroscopy, Physical Electronics, Inc: Eden Prairie, MN, USA (1995).

47. Yesodharan E., and Gratzel M., Photodecomposition of liquid water with TiO_2 supported noble metal clusters, Chemical Acta, 66, 2145 (1983).

48. Sandell A., Sanyal B., Walle L., Richter J., Plogmaker S., Karlsson P., Borg A., and Uvdal P., Probing and modifying the empty –state threshold of anatase TiO_2: Experiments and ab initio theory. Physical Review B, 78, 075113 (2008).

49. Kodaira S., Sakisaka Y., Maruyama T., Haruyama Y., Aiura Y., and Kato H., Angle-resolved photoemission study of an in-gap state in TiO_2, Solid State Communications, 89, 9 (1994).

50. Siddiqui H., Modification of physical and chemical properties of titanium dioxide (TiO_2) by ion implantation for dye sensitized solar cells (2019). (https://www.intechopen.com/online-first/modification-of-physical-and-chemical-properties-of-titanium-dioxide-tio2-by-ion-implantation-for-dy)

51. Miao X., Pan K., Liao Y., Zhou W., Pan Q., and Tian G., Controlled synthesis of mesoporous anatase TiO_2 microspheres as a scattering layer to enhance the photoelectrical conversion efficiency, Journal of Material Chemistry A, 9853 (2013).

52. Pan K., Dong Y., Zhou W., Wang G., Pan Q., Yuan Y., TiO_2-B nanobelt/anatase TiO_2 nanoparticle heterophase nanostructure fabricated by layer-by-layer assembly for high-efficiency dye-sensitized solar cells, Electrochemistry Acta, 88,263 (2013).

53. Zhang G., Pan K., Zhou W., Qu Y., Pan Q., Jiang B., Anatase TiO_2 pillar-nanoparticle composite fabricated by layer-by-layer assembly for high-efficiency dye-sensitized solar cells, Dalton Transactions, 41,12683, (2012).

54. Zhang Q., Guo X., Huang X., Huang S., Li D., and Luo Y., Highly efficient CdS/CdSe-sensitized solar cells controlled by the structural properties of compact porous TiO_2 photoelectrodes, Physical Chemistry and Chemical Physics, 13, 4659, (2011).

55. Hochbaum A. I., and Yang P., Semiconductor nanowires for energy conversion, Chemistry Review, 110, 527 (2010).

56. Xia Y, Yang P, Sun Y, Wu Y, Mayers B, Gates B, et al. One-dimensional nanostructures: synthesis, characterization and applications, Advanced Materials, 15, 353 (2003).

57. Miao Z., Xu D., Ouyang J., Guo G., Zhao X., Tang Y., Electrochemically induced sol-gel preparation of single-crystalline TiO_2 nanowires. Nano Letters, 2, 717 (2002).

58. Lei Y., Zhang L. D., Meng G W., Li G H., Zhang X Y., and Liang C H., Preparation and photoluminescence of highly ordered TiO_2 nanowire arrays, Appllied Physics Letters, 148, 398 (2001).

59. Zhang X., Yao B., Zhao L., Liang C. F., Zhang L., Mao Y., Electrochemical fabrication of single-crystalline anatase TiO_2 nanowire arrays, J Electrochem Soc, 148, 398 (2001).

60. Wolcott A., Smith W. A., Kuykendall T. R., Zhao Y., Zhang J Z., Photoelectrochemical water splitting using dense and aligned TiO_2 nanorod arrays, Small, 5, 104 (2009).

61. Roy P., Berger S., Schmuki P., TiO_2 nanotubes: synthesis and applications, Angew Chem, 50, 2904 (2011).

62. Liu L., Ji Z., Zou W., Gu X., Deng Y., and Gao F., In situ loading transition metal oxide clusters on TiO_2 nanosheets as co-catalysts for exceptional high area and nano-Schottky junctions, Journal of Colloidal Interface Science, 388, 144 (2012).

63. Wang D., Zhou W., Hu P., Guan Y., Chen L., Li J., High ethanol sensitivity of palladium/TiO_2 nanobelt surface heterostructures dominatied by enlarged surface area and nano-Schottky junctions, Journal of Colloidal Interface Science, 388, 144 (2012).

64. Pan K., Dong Y., Zhou W., Pan Q, Xie Y., and Xie T., Facile fabrication of hierarchical TiO_2 nanobelt/ZnO nanorod heterogenous nanostructure: an efficient photoanode for water splitting, ACS Appllied Materials Interfaces, 5, 8314 (2013).

65. Hu P., Du G., Zhou W., Cui J., Lin J., and Liu H., Enhancement of ethanol vapour sensing of TiO_2 nanobelts by surface engineering, ACS Applied Material Interfaces, 2, 3263, (2010).

66. Lu Y., Wang G., Zhang H., Zhang Y., Kang S., and Zhao H, Photoelectrochemical manifestation of intrinsic photoelectron transport properties of vertically aligned {001} faceted single crystal TiO_2 nanosheet films, RSC Advances, 5, 55438 (2015).

67. Chen X., Liu L., Yu P. Y., and Mao S. S., Increasing solar absorption for photocatalysis with black hydrogenated titanium dioxide nanocrystals, Science, 331, 746 (2011).

68. Kudo A., and Miseki Y., Heterogeneous photocatalyst materials for water splitting, Chemical Society Review, 38, 253 (2009).

69. Aschauer U., Selloni A., Hydrogen interaction with the anatase TiO_2 (101) surface, Physical Chemisty and Chemical Physics, 14, 16595 (2012).

70. Hamdy M. S., Amrollahi R., Mul G., Surface Ti^{3+} containing (blue) titania: a unique photocatalyst with high activity and selectivity in visible light-stimulated selective oxidation, ACS Catalysis, 2, 2641 (2012).

71. He H., Yang K., Wang N., Luo F., and Chen H., Hydrogenated TiO_2 film for enhancing photovoltaic properties of solar cells and self-sensitized effect, Journal of Applied Physics,114, 213505 (2013).

72. Jiang X., Zhang Y., Jiang J., Rong Y., Wang Y., and Wu Y., et al. Characterization of oxygen vacancy associates within hydrogenated TiO_2: a positron annihilation study, J Phys Chem C,116,22619 (2012).

73. Lu H., Zhao B., Pan R., Yao J., Qiu J., Luo L., Safe and facile hydrogenation of commercial Degussa P25 at room temperature with enhanced photocatalytic activity, RSC Advances, 4, 1128 (2014).

74. Naldoni A., Allieta M., Santangelo S., Marell M., Fabbri F., and Cappelli S., Effect of nature and location of defects on bandgap narrowing in black TiO_2 nanoparticles J American Chemical Society,134,7600 (2012).

75. Plodinec M., Gajovic A., Jaksa G., Zagar K., Ceh M., High-temperature hydrogenation of pure and silver-decorated titanate nanotubes to increase their solar absorbance for photocatalytic applications, Journal of Alloy and Compounds, 591, 147 (2014).

76. Raghunath P., Huang W. F., and Lin M. C., Quantum chemical elucidation of the mechanism for hydrogenation of TiO_2 anatase crystals, Journal of Chemical Physics,138, 154705 (2013).

77. Samiee M., Luo J., Enhancing the visible-light photocatalytic activity of TiO_2 by heat treatments in reducing environments, Material Letters, 98, 205 (2013).

78. Xia T., Chen X., Revealing the structural properties of hydrogenated black TiO_2 nanocrystals, Journal of Materials Chemistry A, 1, 2983 (2013).

79. Pesci F. M., Wang G., Klug D. R., Li Y., Cowan A.J., Effiecient suppression of electron-hole recombination in oxygen –deficeint hydrogen treated TiO_2 nanowires for photoelectrochemical water splitting, Journal of Physical Chemistry C, 117, 25837 (2013).

80. Kang Q., Cao J., Zhang Y., Liu L., Xu H., and Ye J., Reduced TiO_2 nanotube arrarys for photoelectrochemical water splitting, Journal of Matericals Chemistry A, 1, 5766 (2013).

81. Xu C., Song Y., Lu L., Cheng C., Liu D., and Fang X., Electrochemically hydrogenated TiO_2 nanotubes with improved photoelectrochemical water splitting performance, Nanoscale Research Letters, 8, 1 (2013).

82. Wang G, Wang H, Ling Y, Tang Y, Yang X., and Fitzmorris R. C., Hydrogen-treated TiO_2 nanowire arrays for photoelectrochemical water splitting, Nano Letters, 11, 3026 (2011).

83. Li S., Qiu J., Ling M., Peng F., Wood B., Zhang S., Photoelectrochemical characterization of hydrogenatede TiO_2 nanotubes as photoanodes for sessing applications, ACS Appllied Materials Interfaces, 5, 11129 (2013).

84. Wang G., Ling Y., Wang H., Yang X., Wang C., and Zhang J. Z., Hydrogen-treated WO_3 nanoflakes show enhanced photostability, Energy and Environmental Sciences, 5,6180 (2012).

85. Lu X., Wang G., Xie S., Shi J., Li W., and Tong Y., Efficient photocatalytic hydrogen evolution over hydrogenated ZnO nanorod arrays, Chemical Communications, 48, 7717 (2012).

86. Sun T., and Lu M., Band-structure modulation of srtio3 by hydrogenation for enhanced photoactivity. Appllied Physics A, 108, 171 (2012).

87. Hong W. K., Park J. B., Yoon J., Kim B. J., Sohn J., Lee Y. B., Hydrogen induced morphotropic phase transformation of single–crystalline vanadium dioxide nanobeams, Nano Letters,13, 1822 (2013).

88. Qiu J., Lai C., Gray E., Li S., Qiu S., and Strounina E., Blue hydrogenated lithium titanate as high-rate anode material for lithium-ion batteries, J Matericals Chemistry A, 2, 6353 (2014).

89. Choi H, Santra P. K., Kamat P. V., Synchronized energy and electron transfer processes in covalently linked Cdse-squaraine dye-TiO_2 light harvesting assembly, ACS Nano, 6, 5718 (2012).

90. Huang K. C., Chang Y. H., Chen C. Y., Liu C. Y., Lin L.Y., Lin L. Y., Vittal R., Improved exchange reaction in an ionic liquid electrolyte of a quasi –solid state dye –sensitized solar cell by using 15-crown 5-functionalized MWCNT, Journal of Matericals Chemistry,21, 18467 (2011).

91. Hoang S., Guo S., Hahn N T., Bard A J., Mullins C. B., Visible light driven photoelectrochemical water oxidation on nitrogen –modified TiO_2 nanowires, Nano Lett 12, 26 (2012).

92. Hwang Y. J., Hahn C., Liu B., and Yang P., Photoelectrochemical properties of TiO_2 nanowire arrays: a study of the dependence on length and atomic layer deposition coating, ACS Nano, 6, 5060 (2012).

93. Sudhagar P., Devadoss A., Nakata K., Terashima C., Fujishima A., Enhanced photoelectrocatalytic water splitting at hierarchical Gd^{3+}: TiO_2 nanostructures through amplifying light reception and surface states passivation, Journal of Electrochemical Society, 162, 108 (2014).

94. Tsui L. K., Saito M., Homma T., Zangari G., Trap-state passivation of titania nanotube by electrochemical doping for enhanced photoelectrochemical performance, Journal of Materials Chemistr A, 3, 360 (2015).

95. Wang G., Wang H., Ling Y., Tang Y., Yang X., Fitzmorris R. C., Hydrogen-treated TiO_2 nanowire arrays for photoelectrochemical water splitting, Nano Letters, 11, 3026 (2011).

96. Hwang Y. J., Hahn C., Liu B., and Yang P., Photoelectrochemical properties of TiO2 nanowire arrays: a study of the dependence on length and atomic layer deposition coating. ACS Nano, 6, 5060 (2012).

97. Wheeler D. A., Wang G., Fitzmorries B. C., Adams S. A., Li Y., and Zhang, J. Z., Ultrafast charge carrier dynamics and photoelectrochemical properties of hydrogen treated TiO_2 nanowire arrays, MRS Proceedings. Cambridge University Press, (2012).

98. Kang Q., Cao J., Zhang Y., Liu L., Xu H., and Ye J., Reduced TiO_2 nanotube arrays for photoelectrochemical water splitting, Journal of Materials Chemistry A, 1, 5766 (2013).

99. Xu C., Song Y., Lu L., Cheng, C., Liu D., and Fang X., Electrochemically hydrogenated TiO_2 nanotubes with improved photoelectrochemical water splitting performance. Nanoscale Research Letters, 8, 1 (2013).

100. Li S., Qiu J., Ling M., Peng F., Wood B., and Zhang S., Photoelectrochemical characterization of hydrogenated TiO2 nanotubes as photoanodes for sensing applications. ACS Appllied Materials Interfaces, 5, 11129 (2013).

101. Ansari S. A., Khan M. M., Ansari M. O., and Cho M. H., Nitrogen-doped titanium dioxide (N-doped TiO_2) for visible light photocatalysis, New Journal of Chemistry, 40, 3000 (2016).

102. Kim H., Da M. S., Kim W., and Choi W., N-doped TiO_2 nanotubes coated with a thin tooxny layer for photoelectrochemical water splitting: dual bulk and surface modification of photoanodes, Energy and Environmental Science,8,247(2015).

103. Zhang X, and Chen Z, Enhanced photoelectrochemical performance of the hierarchical micro/nano-structured TiO_2 mesoporous spheres with oxygen vacancies via hydrogenation, RSC Advances, 5, 9482 (2015).

104. Zhang S., Zhang S., Perg B., Wang H., Yu H., and Wang H., High performance hydrogenated TiO_2 nanorod arrays as a photoelectrochemical sensor for organic compounds under visible light, Electrochemical Communications, 40, 24 (2014).

105. Kin F. M., Lee C., Hone J., Shan J, and Heinz T. F., Atomically Thin MoS_2: A New direct-gap semiconductor, Physics Review Letters, 105, 136805 (2010).

106. Jessica R. P., Shanhui F., Broadband absorption enhancement in solar cells with an atomically thin active layer, ACS Photonics, 3, 571, (2016).

107. Loghman K, Combination of mesoporous titanium dioxide with MoS_2 nanosheets for high photocatalytic activity, Polish Jornal of Chemical Technology, 2, 56, (2019).

108. Narayanan P. R., and Narayana Murty S. V. S., Advanced materials and manufacturing processes for strategic engineering and applied science, Materials Science Forum, 830, 533 (2015).

109. Yuan Y. J., Tu J., Ye Z., Chen D., Hu B., Huang Y., Chen T., Cao D., Yu Z., and Zou Z., MoS_2 -graphene/ $ZnIn_2S_4$ hierarchical microarchitectures with an electron transport bridge between light-harvesting semiconductor and cocatalyst: A highly efficient photocatalyst for solar hydrogen generation, Applied Catalysis B: Environmental, 13, 188, (2016).

110. Xiaohui R., Xiang Q., Yongzhen S., Si X., Guanghua X., Zhen Z., Zongyu H., and Jianxin Z., 2D co-catalytic MoS_2 nanosheets embedded with ID TiO_2 nanoparticles for enhancing photocatalytic activity, Jounrl of Physics D: Appllied Physics. 49, 315304 (2016).

111. Yu D., Chen S., Yi L., Xiao Y., Hu J., Wu S., Zhao D., Ge T., Chang, G,, Li J, Lenaerts S., Janiak C., Yang X., and Su B., Hierarchical MoS_2 @ TiO_2Heterojuctions for Enhanced Photocatalytic Performance 13, 1609, (2018).

112. Wang Q, Yu P, Bai L, Bao R, Wang N, Cheng C, LiuZ, Yang M, YangW and Guo Z, Self-assembled nano-leaf/vein bionic structure of TiO_2/MoS composites for photoelectric sensors, Nanoscale, 9, 18194 (2017).

113. Zhang C., Wu Z., Liu J. J., Pial L. Y., One-step synthesis of water-soluble and highly fluorescent MoS2 quantum dots for detection of hydrogen peroxide and glucose, Sensors and Actuators B: Chemical, 252, 183 (2017).

114. Cravanzola S., Sarro M., Cesano F., Calza P., and Scarano D., MoS2 nanoparticles decorating titanate-nanotube surfaces: combined microscopy, spectroscopy, and catalytic studies, Langmuir, 19, 5469 (2015).

115. Zhang W., Xiao X., Zheng L., and Wan, C., Fabrication of TiO2/ MoS2 composite photocatalyst and its photocatalytic mechanism for degradation of methyl orangeunder visible light, Canadian Journal of Chemical Engineering, 93, 1594 (2015).

116. Xiang Q., Yu J., and Jaroniec M., Synergetic effect of MoS2 and graphene as cocatalysts for enhanced photocatalytic H2 production activity of TiO2 nanoparticles, Journal of Americal Chemical Society, 134, 6575 (2012).

117. Luo H., Mueller A.H., McCleskey T. M., Burrell A.K., Bauer E., Jia Q. X., Structural and Photoelectrochemical Properties of BiVO4 thin films, Physical Chemistry C , 112, 6099 (2008).

118. Zhou M., Bao J., Xu Y., Zhang J., Xie J., Guan M., Wang C., Wen L., Lei Y., and Xie Y., Photoelectrodes Based upon Mo:BiVO4 Inverse Opals for Photoelectrochemical Water Splitting,ACS Nano, 8, 7088, (2014).

119. Gu S., Wu X., Zhou H., Wang F., Liu J., and Li W., In situ preparation of novel heterojunction BiOBr/BiVO4 photocatalysts with enhanced visible light photocatalytic activity, RSC advances, 5, 92769 (2015).

120. Sayama K., Nomura A., Arai T., Sugita T., Abe R., Yanagida M., Oi T., Iwasaki Y., Abe Y., and Sugihara H., Photoelectrochemical Decomposition of Water into H2 and O2 on Porous BiVO4 Thin-Film Electrodes under Visible Light and Significant Effect of Ag Ion Treatment, Physical Chemistry B , 110, 11352 (2006).

121. Lim A. R., Choh S. H., and Jang M. S., Prominent ferroelastic domain walls in BiVO4 crystal, Journal of Physics: Condensed Matter 7, 7309 (1995).

122. Navarro R. M., Álvarez Galván M.C., del Valle F., Villoria J. A, Mano D. L., and Fierro J. L.G., Water splitting on semiconductor catalysts under visible-light irradiation, Chem. Sus. Chem. 2, 47(2009).

123. Guiji L., Chunmei D., Jingying S., Donge W., Zhijun W., Nan W. , Fengqiang X. ,Can L., Visible light driven overall water splitting using

cocatalyst/BiVO4 photoanode with minimized bias, Physical Chemistry Chemical Physics,15, 4589 (2013).

124. Li D., Wang W., Jiang D., Zheng Y., and Li X., Surfactant-free hydrothermal fabrication of monoclinic BiVO4 photocatalyst with oxygen vacancies by copper doping, RSC Advances, 5, 14374 (2015).

125. Hu J., Zhao X., Chen W., Su H., Zhong O., and Chen O., Theoretical Insight into the Mechanism of Photoelectrochemical Oxygen Evolution Reaction on $BiVO_4$ Anode with Oxygen Vacancy, Journal of Physicl Chemistry C, 121, 18702 (2017).

126. Fu Y. S., Sun X., and Wang X., $BiVO_4$–graphene catalyst and its high photocatalytic performance under visible light irradiation, Materials Chemistry and Physics, 131, 325 (2011).

127. Xie M., Feng Y., Fu X., Luan P., Jing L., Fu X., Luan P., and Jing L., Phosphate-bridged TiO2-BiVO4 nanocomposites with exceptional visible activities for photocatalytic water splitting, Journal of Alloys and Compounds, 631 ,120 (2015).

128. Tong R., Wang X., Zhou, Liu Q., Zhang Z., Wang H., and Lund P. D., Cobalt-Phosphate modified TiO_2/ $BiVO_4$ nanoarrays photoanode for effiecient water splitting, International Journal of Hydrogen Engergy, 42, 5496(2017).

129. Cheng B., Yang J., Cho H., and Wu J., Fabrication of an Efficient $BiVO_4$-TiO_2Heterojuction Photoanode for photelectrochemical Water Oxidation, ACS Appl Mater interfaces, 8, 20032 (2016).

130. Zhang X., Zhang B., Cao K., Brillet J., Chen J., Wang M., and Shen Y., Novel $BiVO_4$/TiO_2 nanocomposites for highly enhanced photocatalytic activity, J. Mater. Chem. A, 3, 21630 (2015).

131. Jung H., Chae S. Y., Shin C., Min B. K., Joo O. S, and Hwang Y. J, Effect of the Si/TiO_2/$BiVO_4$ heterojunction on the on-set potential of photocurrents for solar water oxidation, ACS Appl. Mater. Interfaces,7, 5788(2015).

132. Mackay K. M, Hydrogen Compounds of the Metallic Elements, E. and F. N. Spon London, UK, 71 (1966). https://www.worldcat.org/title/hydrogen-compounds-of-the-metallic-elements/oclc/681825598

133. Liu P.P., Liu X., Huo X. H., Tang Y., Xu J., and Ju H., TiO_2–$BiVO_4$ Heterostructure to enhance photoelectrochemical efficiency for sensitive Aptasensing, ACS Applied Materials Interfaces 2017, 9, 32, 27185 (2017).

134. Resasco J., Zhang H., Kornienko N., Becknell N., Lee H., Guo J., Briseno A. L., and Yang P., TiO_2/$BiVO_4$ nanowire heterostructure photoanodes based on Type II band alignment, ACS Central Science, 2, 80 (2016).

135. Cullity B.D., Elements of X-ray diffraction, Addison-Wesley Publishing Company Inc, Reading, Massachusetts, (1956).

136. Waseda Y., Matsubara E., and Shinoda K., X-Ray Diffraction Crystallography, Introduction, Examples and Solved Problems, Springer-Verlag Berlin Heidelberg, (2011).

137. Igwebike-Ossi C. D., X-Ray Techniques, https://www.intechopen.com/books/failure-analysis-and-prevention/x-ray-techniques

138. Malvern Panalytical: https://www.malvernpanalytical.com/en/products/product-range/xpert3-

139. P. Scherrer, Göttinger Nachrichten Gesell., Vol. 2, 1918, p 98

140. Patterson, A. (1939). "The Scherrer Formula for X-Ray Particle Size Determination". Phys. Rev. 56 (10): 978–982.

141. Moulder J. F., Stickle W. F., Sobol P. E., and Bomben K. D., Handbook of X-ray Photoelectron Spectroscopy., Edited by Jill Chastain, Published by Perkin-Elmer Corporation, Physical Electronics Division, Eden Prairie, United States of America.

142. Zaidi E., XPS, AES and laser Raman spectroscopy: A fingerprint for a materials surface characterisation. Jurnal Sains Nuklear Malaysia, 23, 26 (2011).

143. Heide P. V., X-Ray Photoelectron Spectroscopy: An Introduction to Principles and Practices, John Wiley & Sons, Inc., New Jersey. (2011),

144. Casa XPS (2005). http://www.casaxps.com/help_manual/XPSInformation/XPSInstr.ht

145. Schrader B., Infrared and Raman Spectroscopy: Methods and Applications, VCH VerlagsgesellschaftmbH (1995).

146. Jones, R.R., Hooper, D.C., and Zhang, L., Raman Techniques: Fundamentals and Frontiers. Nanoscale Research Letters, 14, 231 (2019).

147. Pei-San H., Kuo Y. C., Chen H.G., Chiang H. H.K., and Lee O.K.S., Detection of osteogenic differentiation by differential mineralized matrix production in mesenchymal stromal cells by Raman spectroscopy, (2013). https://doi.org/10.1371/journal.pone.0065438

148. Baer D. R., and Thevuthasan S., Characterization of thin Films and coatings, in Handbook of Deposition Technologies for Films and Coatings, Peter M. Martin, Elsevier Inc. (2010)

149. Raja P. M. V., and Barron A. R., Physical Methods in Chemistry and Nano Science, OpenStax CNX (2019)

150. Kuo J., Electron Microscopy, Methods and Protocols, 2019, Springer Nature Switzerland AG (2019).

151. Reimer L., Scanning Electron Microscopy-Physics of Image Formation and Microanalysis, Springer-Verlag Berlin, Heidelberg, (1998).

152. Shindo D., and Oikawa T., Energy Dispersive X-ray Spectroscopy. In: Analytical Electron Microscopy for Materials Science. Springer, Tokyo (2012).

153. Shuster, J., Southam, G., and Reith, F. Applications of Scanning Electron Microscopy in Geomicrobiology. In J. Kenney, H. Veeramani, & D. Alessi (Eds.), Analytical Geomicrobiology: A Handbook of Instrumental Techniques, Cambridge University Press, Cambridge (2019).

154. Marturi N., Vision and visual serving for nanomanipulation and nanocharacterization in scanning electron microscope, Micro and nanotechnologies/ Microelectronics. Universit´e deFranche-Comt´e (2013).

155. Williams D. B. and Carter C. B., Transmission Electron Microscopy: A Textbook for Materials Science, Springer, (2009).

156. Schroder D. K., Semiconductor materials and device characterization, 2006, John Wiley & Sons, Inc (2006).

157. Barsoukov E., and Macdonald J. R., Impedance Spectroscopy: Theory, Experiment, and Applications, Wiley (2005)

158. Cardon F., and Gomes W. P, On the determination of the flat-band potential of a semiconductor in contact with a metal or an electrolyte from the Mott-Schottky plot, Journal of Physics D: Applied Physics, 11, L63 (1978).

159. Yong X. G., Ahalapitiya H. J., Yu Z., Chen X., and Li M., Hydrothermal Synthesis of Nanomaterials, Hindawi Journal of Nanomaterials, 2020, 8917013 (2020)

160. Raghunath P., Huang W. F., and Lin M. C., Quantum chemical elucidation of themechanism for hydrogenation of TiO_2 anatase crystals, Journal of Chemical Physics, 138, 154705. (2013).

161. Prokes S.M., Gole J.L., Chen X., Burda C., and Carlos W. E., Defect-related optical behavior in surface modified TiO2 nanostructures. Advanced Functional Materials, 15, 161 (2005)

162. Ullattil S. G.,, Narendranath S. B., Pillai S. C., and PeriyaP., Black TiO_2 nanomaterials: A review of recent advances, Chemical Engineering Journal, 343, 708 (2018).

163. Jiang X., Zhang Y., Jiang J., Rong Y., Wang Y., Wu Y., and Pan C., Characterization of oxygen vacancy associates within hydrogenated TiO_2: A positron annihilation, Journal of Physical Chemistry C, 116, 22619 (2012).

164. Sun S., Song P., Cuia J., and Liang S., Amorphous TiO_2 nanostructures: synthesis, fundamental properties and photocatalytic applications, Catalysis Science and Techonolgy, 9, 4198 (2019).

165. Scepanovi M., Sskrabic A., Bereca V., Golubovic A., Mitrovi Z.D., Popovic. K.Z.P., Characterization of La-Doped TiO2 Nanopowders by Raman Spectroscopy. 115, 4, Acta Physica Polonica (2009)

166. Ocana M., Garcia-Ramos J. V., and Serna C. J., Infrared response of vitreous titanium dioxide films with anatase short-range order, Journal of American Ceramic Society, 75, 2010 (1992).

167. Chen X., Liu L., Liu Z., Marcus M.A., Wang W.C., Oyler, N.A., Grass M.E., Mao B., Glans P., Yu P.Y., Guo J., and Mao S.S., Properties of disorder-engineered black titanium dioxide nanoparticles through hydrogenation, Scientific Reports, 3, 1518 (2013).

168. Crocker M., Herold R. H. M., Wilson A.E., Mackay M., Emeis C.A., Hoogendoorn A. M., J. 1H NMR spectroscopy of titania. Chemical shift assignments for hydroxy groups in crystalline and amorphous forms of TiO_2, Chemical Society Faraday Transactions, 92, 2791(1996).

169. Jonsen P., 1H NMR study of reduced Ru/TiO_2 and TiO_2, Colloids and Surfaces, A, 36, 127 (1989).

170. Nahm H. H., and Park C. H., First-Principles LDA+U Study of Hydrogen Impurities in Anatase TiO_2, J. Korean Physics Society, 56, 485 (2010).

171. Filippone F., Mattioli G., Alippi P., and Amore B. A., Properties of hydrogen and hydrogen–vacancy complexes in the rutile phase of titanium dioxide, Physical Review B, 80, 245203 (2009).

172. Aschauer U., and Selloni A., Hydrogen interaction with the anatase TiO_2 (101) surface, Physical Chemistry and Chemical Physics,14, 16595 (2012).

173. Wang Z., Yang C., Lin T., Yin H., Chen P., Wan D., Xu F, Huang F., Lin J., Xie X., and Jiang M., A new approach to prepare highly active and stable black

titania for visible light-assisted hydrogen production, Advanced Functional Materials, 23, 5444 (2013).

174. Klahr B., Gimenez S., Santiago F., Hamann T, Bisquert J., Water Oxidation at Hematite Photoelectrodes: The Role of Surface States, Journal of American Chemical Society, 134, 4294(2012).

175. Morgan B. J., and Watson G.W., A DFT+U description of oxygen vacancies at the TiO_2 rutile (110) surface Surface Science, 601, 5034–5041 (2007).

176. Kresse G., and Furthmuller J., Efficient iterative schemes for ab initio total-energy calculations using a plane-wave basis set, Physical Review B: Condensed Matter Physics, 54, 11169 (1996)

177. Mehta M., Kodan N., Kumar S., Kaushal A., Mayrhofer l., Walter M., Moseler M., Dey A., Krishnamurthy S., Basu S., and Singh A.P., Hydrogen treated anatase TiO2: a new experimental approach and further insights from theory, Jounal of Physical Chemistry A. 2, 2670 (2016).

178. Liu X., Xu H., Grabstanowicz L. R., Gao S., Lou Z., Wang W., Huang B., Dai Y., and Xu T., Ti3+ self-doped TiO_{2-x} anatase nanoparticles via oxidation of TiH_2 in H_2O_2, Catalysis Today, 225, 80 (2014).

179. Naldoni A., Allieta M., Santangelo S., Marelli M., and Fabbri F., Effect of nature and location of defects on bandgap narrowing in black TiO_2 nanoparticles, Journal of American Chemical Society, 134, 7600 (2012).

180. (a) TiO_2 anatase (JCPDS card no. 21-1272), (b) TiO_2 rutile (JCPDS card no. 21-1276), and (c) TiO_2 brookite (JCPDS card no. 29-1360).

181. Ohsaka T., and Fujiki Y, Raman Spectra in hollandite type compounds, Solid State Communications, 44, 1325, (1982).

182. Mazza T., Barborini E., Piseri P., Milani P., Cattaneo D., Bassi A. L., Bottani C. E., and Ducati C., Raman spectroscopy characterization of TiO_2 rutile nanocrystals, Physical Review B ,75, 045416 (2007).

183. Lia X., and Zhu H., Two-dimensional MoS2: Properties, preparation, and applications, Journal of Materiomics, 1, 33 (2015).

184. Virsek M., Jesih A., Milosevic I., Damnjanovic M., Remskar M., Raman Scattering of the MoS_2 and WS_2 single nanotubes, Journal of Surface Science,601, 2868 (2007).

185. Ho W, Yu J C, Lin J, Yu J, Li P, Preparation and photocatalytic behaviour of MoS_2 and WS_2 nanocluster sensitized TiO_2, Langmuir 20, 5865 (2004).

186. Pesci F. M., Wang G., David R. K., Yat L., Cowan A. J., Efficient suppression of electron-hole Recombination in oxygen- deficient hydrogen treated TiO_2 nanowires for photo-electro-chemical water splitting, The Journal of Physical Chemistry C: Nanomaterials and Interfaces, 117, 25837 (2013).

187. Lee C., Li Q., Kalb W., Liu X. Z., Berger H., Carpick R. W., and Hone J., Frictional characteristics of atomically thin sheets, Science, 328, 76, (2010).

188. Novoselov K. S., Jiang D., Schedin F., Booth T. J., Khotkevich V. V., Morozov S. V., and Geim A. K., Two dimensional atomic crystals, PNAS, 102, 10451 (2005).

189. Wang Q. H., Kalantar-Zadeh K., Kis A., Coleman J. N., Strano M. S., Electronics and optoelectronics of two-dimensional transition metal di-chalcogenides, Nature Nanotechnology,7, 699 (2012).

190. Cao L., Wang R., Wang D., Xu L., Li X, Enhanced visible light photocatalytic activity for the hybrid MoS_2/ anatase TiO_2(001) nanocomposite: a first-principles study, Chemistry Physics Letters, 612, 285, (2014).

191. Liu C., Wang L., Tang Y., Luo S., Liu Y., Zheng S., Zeng Y., and Xu Y., Vertical single or few-layer MoS_2 nanosheets rooting into TiO_2 nanofibers for highly efficient photocatalytic hydrogen evolution, Applied Catalysis B-Environmental,164, 1 (2015).

192. Shen M., Yan Z., Yang L., Du P., Zhang J., and Xiang B., MoS_2 nanosheet /TiO_2 nanowire hybrid nanostructures for enhanced visible-light photocatalytic activities, Chemical Communcations, 50, 15447 (2014).

193. Jia F., Liu C., Yang B., Xian Z., Hao Y, Jiaming N., and Shaoxian S., Thermal modification of molybdenum disulphide surface for tremendous improvement of Hg^{2+} adsorption from aqueous solution, ACS Sustainable Chemistry and Engineering, 6 ,579 (2018).

194. Kanda S., Akita T., Fujishima M., Tada H., Facile synthesis and catalytic activity of MoS_2/TiO_2 by a photo-deposition-based technique and its oxidized derivative MoO_3/TiO_2 with a unique photo-chromism, J. Colloidal and Interfaces Science, 354, 607 (2011).

195. Hu K., Hu X., Xu Y., and Sun J., Synthesis of nano- MoS_2/ TiO_2 composite and its catalytic degradation effect on methyl orange, Journal of Material Science, 45 ,2640 (2010).

196. Tacchini I., Terrado E., Ansón A., and Martínez M. T., Preparation of a TiO_2–MoS_2 nanoparticle-based composite by solvo-thermal method with enhanced photo-activity for the degradation of organic molecules in water under UV light, Micro Nano Lett, 6, 932 (2011).

197. Sakurai K. and MizusawaM., X-ray diffraction imaging of anatase and rutile, Analytical Chemistry, 82, 3519 (2010).

198. Venkatesan R., Velumani S., Ordon K., Makowska-Janusik M., Corbel G., and Kassiba A., Structural and morphological data of RF-Sputtered $BiVO_4$ thin films, Matericals Chemistry and Physics, 205, 325 (2018).

199. Klahr B., Gimenez S., Fabregat-Santiago F., Hamann T., and Bisquert J., Water Oxidation at hematite photoelectrodes: The role of surface states, Journal of American Chemical Society, 134, 4294 (2012).

200. Dao T. D., Dang C. T. T., Han G., Hoang C. V., Yi W., Narayanamurti V, and Nagao T, Chemically synthesized nanowire TiO_2/ZnO core-shell p-n junction

array for high sensitivity ultraviolet photodetector, Applied Physics Letters, 103, 193119 (2013).

201. Rettie A. J. E., Lee H. C., Marshall L. G., Lin J. F., Capan C., Lindemuth J., McCloy J. S., Zhou J., Bard A. J., and Mullins C. B., Combined charge carrier transport and photoelectrochemical characterization of $BiVO_4$ single crystals: intrinsic behavior of a complex metal oxide, American Journal of Chemical Society, 135, 11389 (2013).

202. Wold A., Photocatalytic properties of titanium dioxide (TiO_2), Chemistry of Materials, 5, 280 (1993).

203. Wang J., Fan X. M., Wu D. Z., Dai J., Liu H., Liu H. R., and Zhou Z. W., Fabrication of CuO/T-ZnO nanocomposites using photo-deposition and their photocatalytic property, Applied Surface Science, 258, 1797 (2011).

204. Henrich V. E., Dresselhaus G., Zeiger H. J., Observation of two-Dimensional phases associated with defect states on the surface of TiO_2, Physical Review Letters, 36, 1335 (1976).

205. Kashiwaya S, J., Morasch, V., Streibel T., Toupance W., and Jaegermann A., The work function of TiO_2, Surfaces, 1, 73 (2018).

206. Vittadini A., Selloni A., Rotzinger F. P., and Grätzel M., Structure and energetics of water adsorbed at TiO_2 anatase 101and 001 surfaces, Physical Review Letters, 81, 2954 (1998).